

Optical and mechanical effects of Elastomeric distributed Bragg reflectors

Gen Kamita

*A dissertation submitted for the degree of Doctor of Philosophy
April 2013*

Supervisor
Prof. Dr. Ullrich Steiner



University of Cambridge
Department of Physics
Thin Films and Interfaces
Hughes Hall

Declaration

This dissertation is the result of my own work and includes nothing which is the outcome of work done in collaboration except where specifically indicated in the text. I declare that no part of this work has been submitted for a degree or any other qualification at this or any other university. This dissertation does not exceed the word limit of 60,000 words set by the Physics and Chemistry Degree Committee.

Cambridge, September 2013

Gen Kamita

Summary

The stop-band tuning of elastomeric distributed Bragg reflectors (DBRs) by deformation, and the underlying mechanical phenomena were studied. The main findings can be summarized as the follows.

1. Repeatable full-colour tuning of the DBR is possible by inflating the DBR into an axisymmetric balloon.
2. The heterogeneous distribution of strain originating from the inflated shape has an impact on the optical and mechanical response of the DBR.
3. Thin elastomer films are under strong influence of surface tension which influences their stress and strain during the fabrication process.

The thesis will be organized as follows. After an introduction to the thesis in Chapter 1, Chapter 2 will discuss the theoretical background. The materials and methods used in the experiments will be covered in Chapters 3. The optics and the mechanics of elastomeric DBRs will be discussed in Chapter 4 and 5. Throughout these chapters, the elastomeric DBRs were studied in axisymmetrically inflated states. The inhomogeneous strain distribution arising from the geometry of the inflated state and the mechanical property of the material, gave rise to a novel colour mixing effect. Chapter 6 discusses the strain induced by the fabrication method of the elastomeric DBR. Soft materials are highly susceptible to buckling and related instabilities; therefore studying the stress and strain in a systematic fashion would open the door for improving the quality, scalability and reproducibility of the fabrication of elastomeric DBRs and related optical devices.

Contents

Declaration	i
Summary	ii
1 Introduction	1
1.1 An overview of mirrors: How rubbers can be used as materials for the manufacture of mirrors	1
1.2 Polymeric optical multilayers assembled from thin films	5
1.2.1 Rolled metallodielectric multilayers	5
1.2.2 Bio-inspired elastic optical multilayer fibres	6
1.3 Bio-inspired chimera coloured multilayer balloon tunable by inflation .	7
2 Theory	10
2.1 Optics	10
2.1.1 Thin film interference	10
2.1.2 Multilayer interference: Rouard's technique	12
2.2 Mechanical properties of rubber	13
2.2.1 Thermodynamic analysis of rubber elasticity	13
2.2.2 Kinetic theory of rubber elasticity (Neo-Hookean model)	16
2.2.3 Nominal stress and true stress of Neo-Hookean rubber	18
2.2.4 The Mooney-Rivlin theory	21
2.3 Forces acting on curved surfaces under pressure differences	25
2.3.1 Hoop stress and pressure radius characteristics of rubber balloons	25
2.3.2 Surface tension and rubber elasticity	28
2.3.3 Young-Laplace equation	30
2.3.4 From Young-Laplace equation to the hoop stress of balloons . .	32
3 Materials and methods	36
3.1 Materials	36
3.1.1 PDMS	36
3.1.2 PSPI	37
3.1.3 LCE (side chain nematic liquid crystal elastomer)	38
3.1.4 Refractive index dispersion	39
3.2 Approximate calculation of film thickness for automatic film thickness measurements	40
3.2.1 Primitive approach for film thickness estimation by fringe counting	40
3.2.2 FFT analysis of interference spectra	41
3.2.3 Limitations of FFT analysis and how to compensate for it	43
3.2.4 Implementation	45
3.3 Assembly of thin films on water	45
3.3.1 Floating technique	45
3.3.2 Pinning technique	46
3.3.3 Catching technique	46

3.3.4	Folding technique	47
3.3.5	Deformation of DBRs and PDMS films by pressure difference . .	48
3.4	Mechanical tests	48
3.4.1	Tensile test	49
3.4.2	Bulge test	50
4	Multilayer mirrored bubbles with spatially-chirped and elastically-tuneable optical bandgaps	52
4.1	Introduction	52
4.2	Materials and methods	53
4.3	Results	53
4.3.1	Full color DBR tuning	53
4.3.2	Polarization rotation	54
4.3.3	Spatial chirp	56
4.4	Conclusion	58
5	Effect of geometry and mechanical properties on the optical effects of axisymmetrically inflated Elastomeric DBRs	59
5.1	Introduction	59
5.2	Materials and methods	60
5.2.1	Experimental methods	60
5.2.2	Equibiaxial test (bulge test)	61
5.3	Theory of Inflation of axisymmetric balloons	63
5.3.1	Zhu’s method	63
5.3.2	Numerical modelling of axisymmetric inflation of Neo-Hookean membranes	65
5.4	Numerical analysis of axisymmetrically inflated films	66
5.4.1	Modelling of PDMS balloons	66
5.4.2	Modelling of DBR balloons	69
5.4.3	Effect of creep on the optical properties of the inflated DBR . .	70
5.5	Conclusion	72
6	Equilibrium state of thin elastomer films on water	74
6.1	Wrinkling/creasing phenomena in soft materials	74
6.2	Free energy of thin elastomer films on water	76
6.2.1	Helmholtz free energy of Neo-Hookean solid under uniaxial deformation	76
6.2.2	Surface free energy of soft thin films on water	77
6.3	Equilibrium state of thin Neo-Hookean films on water	79
6.3.1	Theoretical calculation	79
6.3.2	Experimental method	79
6.3.3	Analysis of the experimental results	79
6.4	Conclusion and future prospect	82
6.5	Additional remarks	83
	Conclusion and future work	85

Contents

Related Publications	88
Acknowledgement	89
Bibliography	90

1 Introduction

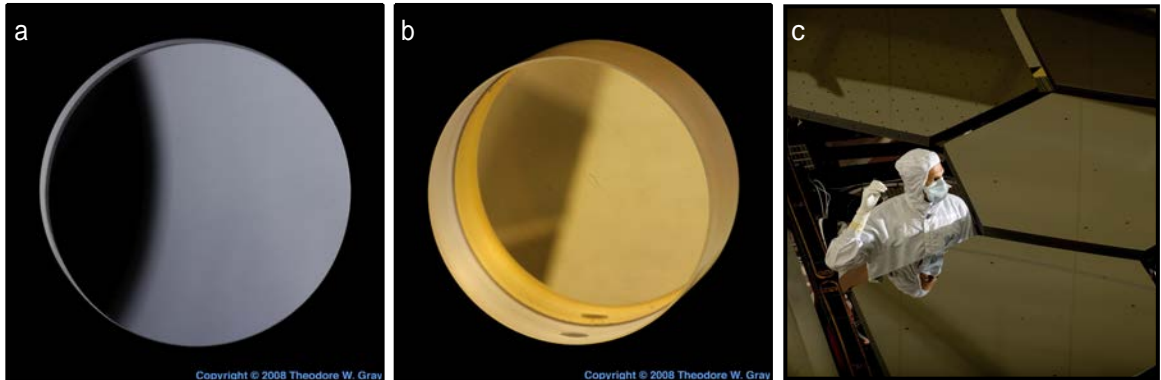


Figure 1.1: Photographs of various mirrors. (a,b) Silver^[1] and gold mirrors.^[2] Reprinted with permission from Theodore Gray. (c) The mirror of the James Webb space telescope. The material of the mirror is Beryllium. Public domain photograph.

1.1 An overview of mirrors: How rubbers can be used as materials for the manufacture of mirrors

How is it possible to make mirrors using rubbers only? This may be the first thought of a reader who sees the title of this thesis. In order to answer this question, we first consider the following three questions.

Q1: What are mirrors made of?

"Silver" may be what many people give as their answer, and indeed, silver-glass mirrors have been among the most popular mirrors, after they were invented by Justus von Liebig in 1835.^[3] However, the choice of material for creating mirrors is not necessarily restricted to the soft, lustrous, white metal with the atomic number 47. In fact, other metals can be also used to manufacture highly reflected mirrors as shown in Figure 1.1. Gold and aluminium are good materials for mirrors especially when the mirror is intended to be used for Infrared^[4] or UV light.^[5] Beryllium is also a suitable material for special requirements. It is used for the mirrors of the James Webb Space Telescope. The reason why beryllium is chosen is because it has an extremely small variation in its coefficient of thermal expansion at temperatures between 30 and 80 K,^[6,7] which makes the mirror stable in the extremely low temperature in space.

Q2: Are metals the only material used for creating mirrors?

The answer to this question is no. The oldest mirror found in history is made from obsidian, a volcanic glass which consists of SiO_2 (70% or more of its weight) and other minerals. The obsidian mirror in Figure 1.2(a), which was excavated from graves in

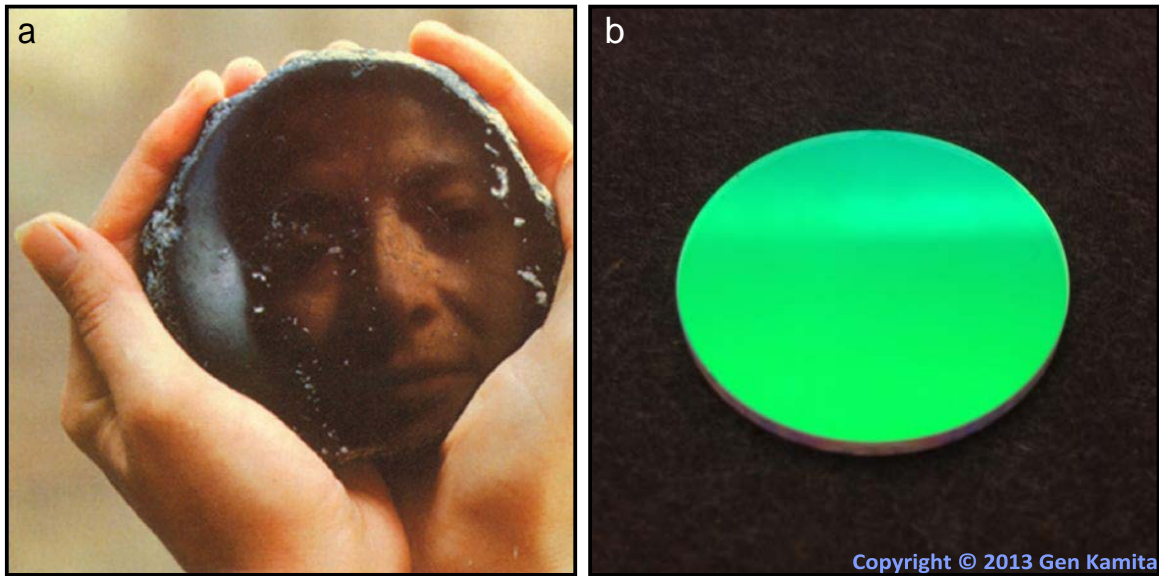


Figure 1.2: (a) An ancient obsidian mirror. Reprinted from Enoch.^[8] (b) Photograph of a conventional DBR taken by the author.

Anatolia, is believed to be made at around 6000 BC, and they were created by grinding and polishing the surface.^[8] Although not as reflective compared to modern metal mirrors, obsidian can be polished to become extremely smooth,^[9] making an ideal surface for specular reflection to take place.

Non-metallic mirrors are still widely used, but of course modern mirrors are no longer made by polishing rocks. Instead, extremely reflective mirrors can be made by creating a multilayer structure consisting of thin layers of alternating low and high refractive index materials. While metallic mirrors reflect light at the surface only, the many-layered mirrors reflect light at every interface, making the rays bounce around in its structure. The multilayer mirrors are also called dielectric mirrors or Distributed Bragg Reflectors (DBRs).

One distinctive property of these mirrors is the wavelength and angle dependency of their reflectance. As these dielectric mirrors operate on the principles of interference, their reflectance is found to be dependent on the wavelength of light, layer thickness and the angle of incident light. This means that DBRs are in general colour selective mirrors as can be seen in Figure 1.2(b), where the DBR is preferentially reflecting green light while allowing other colours to transmit through it as shown in Figure 1.3.

Since DBRs can be made from transparent materials, and because its reflectance improves by the increase in the number of layers and/or refractive index contrast between the constituent materials, DBRs can be made to reflect 99.99%^[10] of the incident light at a wavelength specified by the layer structure. The theoretical description of such properties was first given by Lord Rayleigh in 1887. A new view of the dielectric mirrors was provided by Yablonovitch and John who re-classified them as one dimensional

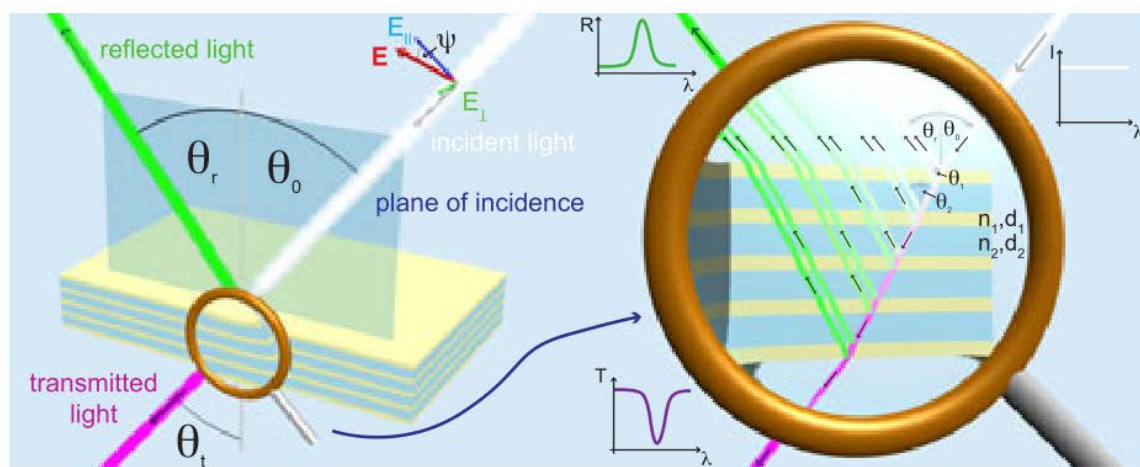


Figure 1.3: Illustration of reflection and transmission of light by a DBR. Reprinted from Kolle.^[12]

photonic crystals.^[11] The knowledge drawn from solid state physics allows us to analyse photonic bandgaps, which provides deep insights in the behaviour of light in nanoscale periodic structures, such as localization of light in defects and waveguides.

Q3: Do the materials used for creating dielectric mirrors have to be hard materials?

The answer to this question is, again, no. In principle, dielectric mirrors can be made from any transparent materials as long as there is a sufficient refractive index contrast between the two constituent materials that comprise the layers, and therefore soft materials such as polymers can be used. Polymers are in general much more responsive to stimuli compared to inorganic materials, and using such materials for creating dielectric mirrors will allow them to exhibit their unique properties in conjunction with the optical properties defined by their periodic structure. Interaction between polymers and their solvents is a classical topic in polymer physics, which was pioneered by Flory and Huggins.^[13] When the capability of volume change of polymer networks in solution is introduced to dielectric mirrors, it will allow the stop-band, or in other words the reflectance peak, to be shifted dramatically.^[14]

Another remarkable property of polymer is its capability to become cross-linked to form elastomers or, more commonly termed, rubbers. Unlike other solid materials, the elasticity of rubbers originates from their entropy and not from their internal energy. This means that as long as the chains are not stretched to their full extent, an imposed deformation will only affect the conformation of its polymer chains, without deforming the covalent bonds of the molecules. The tension of stretched rubbers arise from the thermal motion of the chains and induces only little stress in the polymer chains at the microscopic scale. This is why it is possible to deform rubbers to a great extent without breaking them. These properties are unique to rubber and rubber-like materials. Once the deformable nature of rubber is introduced to a dielectric mirror, it will allow the

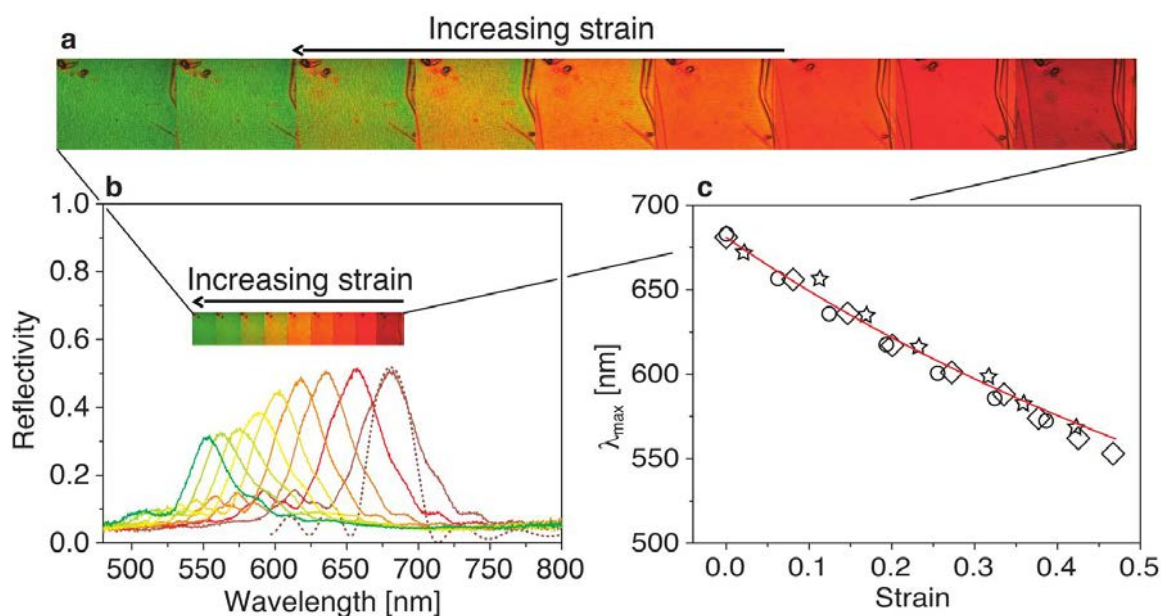


Figure 1.4: Colour tuning of DBR made from rubbers. (a) The DBR shifts its colour as a function of strain. (b) Reflection spectra of the DBR during stretch tuning. (c) Peak wavelength of the reflectance of the DBR as a function of strain. Reprinted from Kolle.^[15]

stop-band to be tuned by deformation.^[15]

After considering the three questions, the answer to the initial question should become clear. The subject of this thesis is elastomeric DBRs, which are dielectric mirrors made from elastomers. Elastomeric DBRs are assembled from thin elastomer films by manipulating them on water surface, and their optical properties are studied in conjunction to their structures and mechanical properties. The marriage of rubbers and dielectric mirrors brings the extraordinary deformability of elastomers to optical applications. Because it is made of rubber, the stop-band can be tuned instantaneously and repeatedly by stretching as shown in Figure 1.4. The many possible applications of rubber-made dielectric mirrors include tunable mirrors, optical filters, light emitting devices, security printing and structural colour displays, just to name a few.

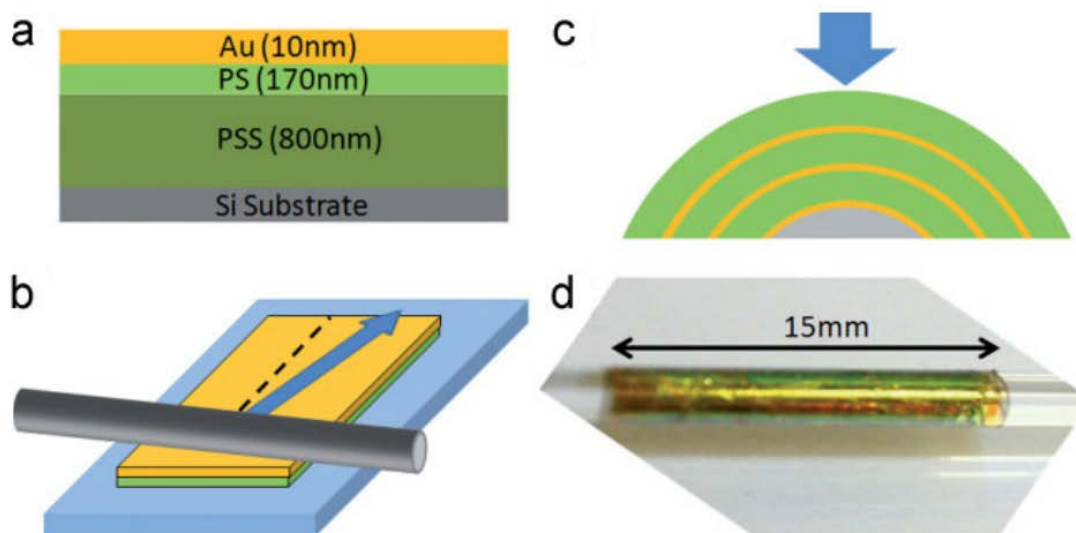


Figure 1.5: (a) Layer structure of films on a initial substrate before the rolling process. (b) Illustration of the rolling process. (c) Cross-section of the sample after rolling. (d) Photograph of a sample after the rolling process. Reprinted from Gibbons.^[17]

1.2 Polymeric optical multilayers assembled from thin films

In the previous section, an overview on mirrors in general was given. A more specific outlook to the field of polymeric optical multilayers assembled from thin films are given in this section. Along with the pioneering work of Kolle *et al.*^[15] on flat stretch-tunable DBRs, which was briefly introduced in the previous section, several studies were performed on polymeric optical multilayers assembled by stacking bilayer films on rods by rolling.^[16–19] The essence of these studies are introduced in the following subsections.

1.2.1 Rolled metallodielectric multilayers

Metallodielectric multilayers are metamaterials which consists of one-dimensional layer stack of dielectrics and metals as shown in Figure 1.5. Gibbons *et al.* used the floated roll technique,^[17] which is an assembly process sharing some key aspects of the fabrication process of this work.

Instead of folding the film as it was done in the initial work of Kolle *et al.*,^[15] Gibbons assembled cylindrical multilayers from polystyrene films coated with a gold film. The polystyrene-gold film was floated on a water surface and rolled on a quartz rod, allowing the bilayer to repeatedly overlay on itself. Sub-wavelength imaging is one of the

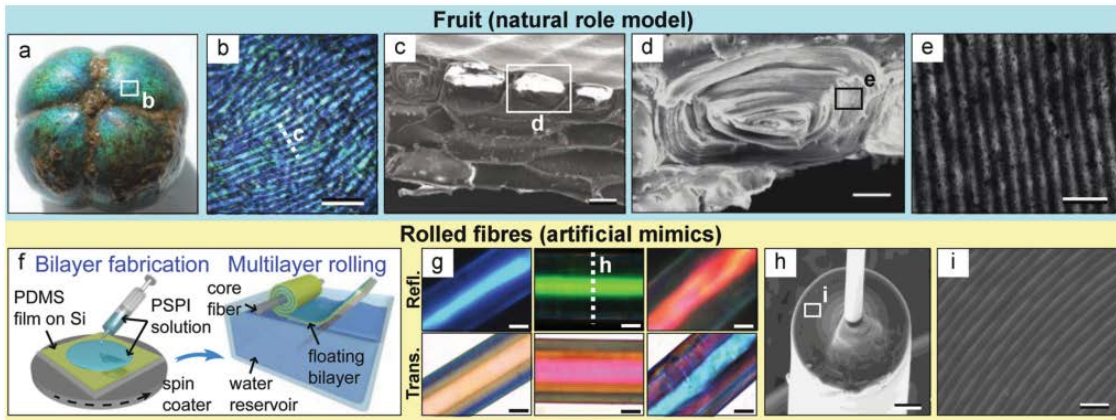


Figure 1.6: (a) A photograph of a *Margaritaria nobilis* without its capsule. (b) Optical micrograph of the surface of the fruit. Elongated cells shows blue colour due to Bragg reflection caused by their multilayer structure. (c) The cross-section through the outer layers of the fruit's endocarp is observed by SEM. (d) A close up SEM image reveals the flattened concentric cylindrical structure of the layer stack in a single tissue cell. (e) TEM image of the multilayer structure. (f) Illustration of the fabrication process of artificial photonic fibres. (g) Micrographs of three photonic fibres in reflection (top row) and transmission (bottom row) (h) SEM image of the cross-section of the photonic fibre. (i) SEM image resolving the individual layers of the photonic fibre. Reprinted from Kolle.^[19]

expected application. Related work includes studies on Corrugated metallodielectric superlattices^[16] and Optical minibands in metallodielectric superlattices.^[18]

1.2.2 Bio-inspired elastic optical multilayer fibres

Kolle *et al.* created elastic optical multilayer fibres which mimic the coloration of a tropical fruit *Margaritaria nobilis* (see Figure 1.6). As Gibbons *et al.* did in their work, a bilayer film of two elastomers were assembled by rolling and a concentric-layered photonic structure was formed. What they used for the rolling assembly was, however, thin glass fibre cores which had only 10 to 20 μm in diameter. This is two orders of magnitude smaller than the quartz rod which was used in the work of Gibbons *et al.*, allowing the number of periods of layer stack to be increased up to 150 periods. The elasticity of the fibre allowed stop-band tuning of 200 nm by elongation. The microscopic conformation of the multilayer stack possessed reduced directional chromaticity which is usually seen in planar DBR, giving rise to its distinctive coloration.

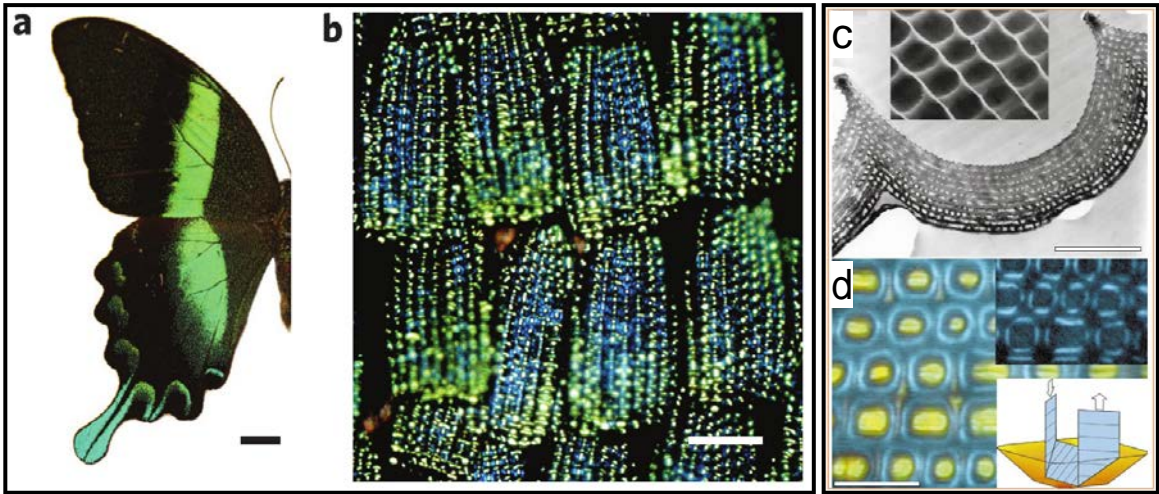


Figure 1.7: (a) Wing of *Papilio blumei*. (b) Micrograph of the wing scale of *Papilio blumei*. (c) Cross-sectional TEM image of the wing scale of *Papilio palinurus*. (d) A micrograph of the wing scale of *Papilio palinurus*. Reprinted from (a, b) Kolle^[20] and (c, d) Vukusik.^[21]

1.3 Bio-inspired chimera coloured multilayer balloon tunable by inflation

As shown in the examples in the previous subsection on the bio-inspired multilayer fibres, photonic crystals found in nature have served as inspirations for novel optical devices in many studies.^[19,20,22–24] Similar to these works, optical devices created from Elastomeric DBRs with a coloration that resembles certain insects are demonstrated in this work. Unlike other works, our device does not exactly resemble that exhibited in one specific animal. Instead, the optical characteristics of the device adopts its essence of coloration from two insects, namely *Papilio blumei*, which is a butterfly well known for its striking green wings, and *Chlorophila obscuripennis*, which is a beetle with bluish green body colour.

Both insects exhibit their colour from multilayer interference and have a similar structure on their surface of their bodies, which are arrays of multilayered concavities. The detailed mechanism of the colouration and the underlying structures are, however, not exactly the same. The green colour of the wings of *Papilio blumei* shown in Figure 1.7(a) is produced by mixing of blue and yellow colours which appears at the edge and centre of the concavity where retro-reflection and specular reflection takes place. Such region-specific colours, which requires optical microscopy to be resolved, are a result of a combined effect of angular-dependent Bragg reflection and variation of angles of the concavity with respect to the incoming ray. Other *Papilio* butterflies such as *Papilio palinurus* are known to exhibit similar colour by the same mechanism as shown in Figure 1.7(d).

The arrangement of the colour of *Chlorophila obscuripennis* shown in Figure 1.8(b)

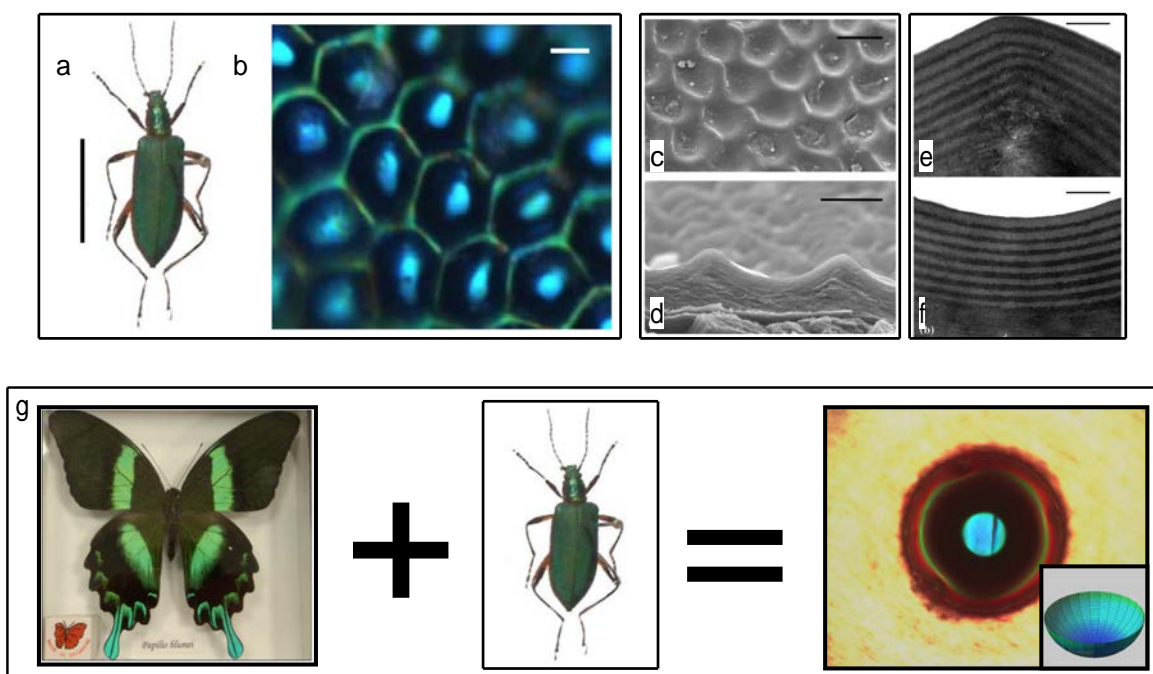


Figure 1.8: (a) Photograph of *Chlorophila obscuripennis*. (b) Micrograph of the outermost elytral surface of *Chlorophila obscuripennis*. (c, d) SEM image of the outermost elytral surface. (c) From top. (d) From side. (e, f) TEM cross-sectional images of the multilayer. (e) Centre. (f) Edge. (g) A representation of the key concept of this thesis. Elastomeric DBRs displays a colouration effect inherited from *Papilio blumei* and *Chlorophila obscuripennis* during axisymmetric inflation. Scales bars are 1 cm for (a) and 5 μm for (b). Reprinted from (a-g)Liu^[25] and (g)Diao.^[26]

may appear very similar to *Papilio blumei*, since there is a similar region-dependent colouration. However, a careful inspection of the colour patterns reveals a clear difference between the colour arrangements of the two insects. While the colour in the centre of the concavity of *Papilio* butterflies have red-shifted colour compared to the edge, the centre is blue-shifted with respect to the edge in the case of *Chlorophila obscuripennis*. Unlike the *Papilio* butterflies, the layer thicknesses of the concavity multilayer structure of *Chlorophila obscuripennis* varies according to the position as shown in Figure 1.8(e) and (f). The layers at the edge are thicker compared to the centre and it is this thickness difference which is the dominant effect on the colour arrangement, making the colour shift opposite from the centre to the edge.

Another important difference between the colouration of the two insects is the polarisation sensitivity. The concavities of the wing scales of *Papilio blumei* are deep enough to allow retro-reflection of light by multiple reflection, resulting in a polarisation sensitive colour as shown in Figure 1.7(d). The concavities of *Chlorophila obscuripennis* are too shallow and is unlikely that they can produce a *Papilio blumei*-like polarisation sensitive colour.

Elastomeric DBRs exhibit unique colour arrangements that inherit the properties of

both insects during axisymmetric inflation. The colour at the centre of the hemispherically-inflated DBR tends to have blue-shifted colour compared to the edge, which resembles *Chlorophila obscuripennis*. However, since the Elastomeric DBRs can be inflated to produce concavities deep enough to cause retro-reflection, they can exhibit a polarisation sensitive colour which resembles *Papilio blumei*. In other words, the deformed DBR is essentially a chimera of *Papilio blumei* and *Chlorophila obscuripennis* in terms of its optical response. Furthermore, the colour can be tuned by the degree of inflation because it is made from rubber. The main focus of this thesis is to reveal the tuneable optical properties of such devices, in relation to their underlying structural and mechanical properties.

2 Theory

In this chapter, theories that are necessary for studying elastomeric DBRs will be described. The subjects included are optics, rubber elasticity and surface chemistry.

The theory of reflection, refraction and interference are essential for understanding the optical characteristics of the elastometric DBR, and will be used in Chapter 4 and 5. The theories of rubber elasticity and surface chemistry give deep insight for the deformation process and sample fabrication and they will serve as a foundation for the discussion in Chapter 5 and Chapter 6.

2.1 Optics

This section was abbreviated from Heavens.^[27] The theory of thin film interference and multilayer interference is derived.

2.1.1 Thin film interference

The refractive indices of the superstrate, film and substrate are given by n_0, n_1 and n_2 respectively and the thickness of the film is given by d . The incidence angle is given by θ_0 and the angle of refraction can be calculated by Snell's law,

$$n_0 \sin \theta_0 = n_1 \sin \theta_1. \quad (2.1)$$

The electric field of the reflected light E can be obtained in the form of an infinite series by taking into account the multiple reflections within the film.

$$E = E_1 + E_2 + E_3 + E_4 + \dots \quad (2.2)$$

The intensity of the electric field of each reflection can be calculated using Fresnel's reflection and transmission coefficients. For light travelling from the superstrate into the thin film, the reflection and transmission coefficients r_{01} and t_{01} are given by the following equations:

$$r_{01\parallel} = \frac{n_1 \cos \theta_0 - n_0 \cos \theta_1}{n_1 \cos \theta_0 + n_0 \cos \theta_1} \quad (2.3)$$

$$r_{01\perp} = \frac{n_0 \cos \theta_0 - n_1 \cos \theta_1}{n_0 \cos \theta_0 + n_1 \cos \theta_1} \quad (2.4)$$

$$t_{01\parallel} = \frac{2n_0 \cos \theta_0}{n_1 \cos \theta_0 + n_0 \cos \theta_1} \quad (2.5)$$

$$t_{01\perp} = \frac{2n_0 \cos \theta_0}{n_0 \cos \theta_0 + n_1 \cos \theta_1} \quad (2.6)$$

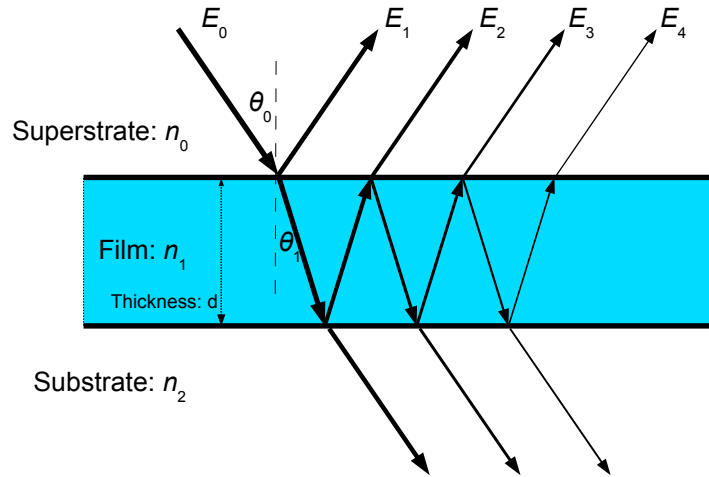


Figure 2.1: Multiple reflections within a film.

Light travelling through a thin film will incur multiple reflections within the film. The overall reflectivity is determined by taking into account the intensity and phase difference of individual reflections.

The subscripts indicate the interface which the reflection/transmission is occurring at and the polarisation of light. For example, $r_{01\parallel}$ is the reflectance of the interface between the superstrate and the film for p-polarised light, e.g. light polarised parallel to the incidence plane, and $r_{12\perp}$ is that of the interface between the film and the substrate for s-polarised light, e.g. light polarised perpendicular to the incidence plane (see Figure 2.1). With the Fresnel coefficients that determine the amplitude of the reflected and transmitted light beams and by taking into account the phase shift Δ that a light beam picks up when travelling through the thin film, Equation 2.2 can be rewritten as

$$E = E_0 (r_{01} + t_{01}t_{10}r_{12}e^{i\Delta} + t_{01}t_{10}r_{12}^2r_{10}^2e^{2i\Delta} + t_{01}t_{10}r_{12}^3r_{10}^3e^{3i\Delta} + \dots) \quad (2.7)$$

$$= E_0 (r_{01} + t_{01}t_{10}r_{12}e^{i\Delta} (1 + r_{12}r_{10}e^{i\Delta} + r_{12}^2r_{10}^2e^{2i\Delta} + \dots)) \quad (2.8)$$

$1 + r_{12}r_{10}e^{i\Delta} + r_{12}^2r_{10}^2e^{2i\Delta} + \dots$ can be written as a geometric series and the equation can be simplified as follows:

$$(1 + r_{12}r_{10}e^{i\Delta} + r_{12}^2r_{10}^2e^{2i\Delta} + \dots) = \sum_{n=0}^{\infty} r_{12}^n r_{10}^n e^{ni\Delta} = \frac{1}{1 - r_{12}r_{10}e^{i\Delta}} \quad (2.9)$$

$$E = E_0 \left(r_{01} + t_{01}t_{10}r_{12}e^{i\Delta} \frac{1}{1 - r_{12}r_{10}e^{i\Delta}} \right) \quad (2.10)$$

$$= E_0 \frac{r_{01} - r_{01}r_{12}r_{10}e^{i\Delta} + (1 - r_{01}^2)r_{12}e^{i\Delta}}{1 - r_{12}r_{10}e^{i\Delta}} \quad (2.11)$$

$$= E_0 \frac{r_{01} + r_{12}e^{i\Delta}}{1 + r_{12}r_{01}e^{i\Delta}} \quad (2.12)$$

$$(2.13)$$

The relation $r_{01} = -r_{10}$ and $t_{01}t_{10} - \sqrt{1 - r_{01}^2}\sqrt{1 - r_{10}^2} = 1 - r_{01}^2$ was used here. Δ , the phase shift for each round trip of the light through the film, is given by

$$\Delta = \frac{4\pi n_2 d \cos \theta_2}{\lambda} \quad (2.14)$$

The relative amplitude of the reflected light A_r is determined as the ratio of the electric field of the incident light and that of the reflected light and the reflectivity is given by the square of the absolute value of A_r .

$$A_r = \frac{E}{E_0} = \frac{r_{01} + r_{12}e^{i\Delta}}{1 + r_{12}r_{01}e^{i\Delta}} \quad (2.15)$$

$$R \equiv |A_r|^2 = A_r A_r^* = \frac{r_{01}^2 + 2r_{01}r_{12} \cos \Delta + r_{12}^2}{1 + 2r_{01}r_{12} \cos \Delta + r_{01}^2 r_{12}^2} \quad (2.16)$$

2.1.2 Multilayer interference: Rouard's technique

The reflectivity of a multilayer can be calculated by extending the results obtained for thin film interference. Starting from the bottommost layer, the effective Fresnel coefficient ρ of each layer can be sequentially calculated to the topmost layer to obtain the overall reflectivity R of the multilayer. We consider a multilayer, again consisting of non-absorbing media, with k distinct, alternating layers. The refractive index and layer thickness are given by n_i and d_i for the i th layer ($i = 0$ and $i = k + 1$ are those of the superstrate and the substrate). The Fresnel coefficients and the phase shift Δ are calculated accordingly. First, we start from calculating the effective amplitude reflectivity of the bottom most layer ρ_k by using Equation 2.15.

$$\rho_k = \frac{r_{k-1,k} + r_{k,k+1}e^{i\Delta_k}}{1 + r_{k,k+1}r_{k-1,k}e^{i\Delta_k}} \quad (2.17)$$

The effective amplitude reflectivity of the $(k - 1)$ th layer can then be calculated by replacing the Fresnel coefficient $r_{k-1,k}$ and $r_{k,k+1}$ with $r_{k-2,k-1}$ and ρ_k .

$$\rho_{k-1} = \frac{r_{k-2,k-1} + \rho_k e^{i\Delta_{k-1}}}{1 + \rho_k r_{k-2,k-1} e^{i\Delta_{k-1}}} \quad (2.18)$$

In a more general expression, ρ_i is given by

$$\rho_i = \frac{r_{i-1,i} + \rho_{i+1}e^{i\Delta_i}}{1 + \rho_{i+1}r_{i-1,i}e^{i\Delta_i}} \quad (2.19)$$

ρ for each layer is calculated by the same process and repeated successively until the final coefficient of the system is given by ρ_1 .

2.2 Mechanical properties of rubber

This section was abbreviated from Treloar.^[28] The theory of mechanical property of rubber is reviewed.

2.2.1 Thermodynamic analysis of rubber elasticity

It is often mentioned that "Gases are the closest relatives of rubber"^[29] and the mathematical formulation of rubber elasticity is strongly related to that of ideal gasses. As it is for gasses, considering the thermodynamics of rubber will give a deep insight to its unique properties. Assuming constant temperature, the following equation which describes the force on a specimen under tension, can be derived from the first and second law of thermodynamics and the equation of the Helmholtz free energy.

$$f = \left(\frac{\partial W}{\partial l} \right)_T = \left(\frac{\partial A}{\partial l} \right)_T = \left(\frac{\partial U}{\partial l} \right)_T - T \left(\frac{\partial S}{\partial l} \right)_T \quad (2.20)$$

Here, f is the force acting on the rubber, W is the work done to the rubber, A is the Helmholtz free energy, T is the absolute temperature, U is the internal energy, l is the length and S is the entropy of the specimen. We can understand from Equation 2.20 that the work done to a solid object by tension at isothermal conditions, can be stored in the form of entropy and internal energy. The following relation

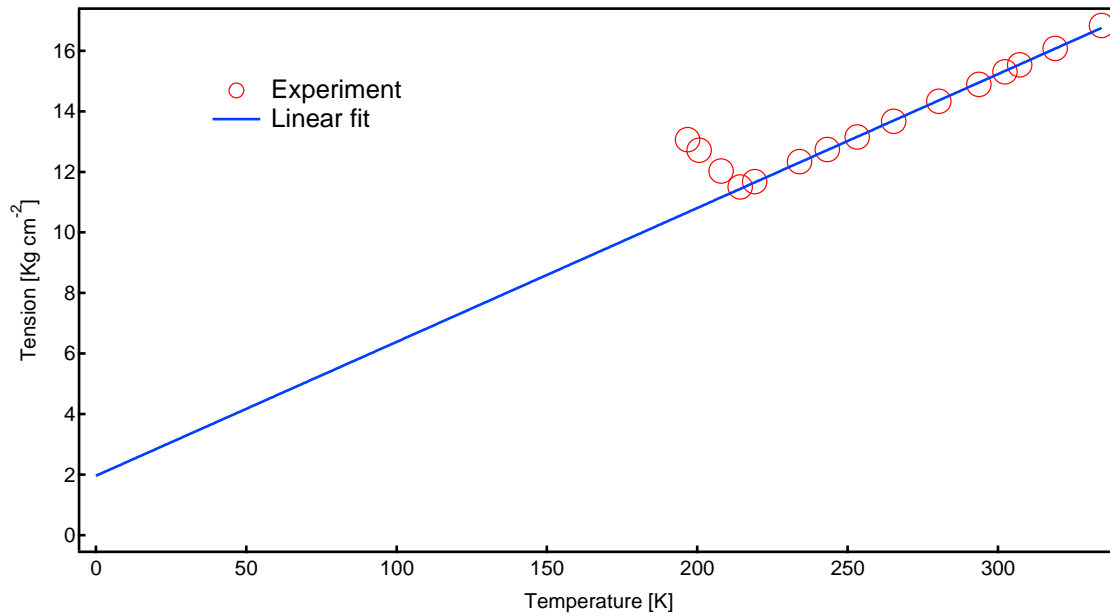


Figure 2.2: Tension on a rubber specimen plotted as a function of temperature. The sample was kept at 350% extension during the measurements. The linear fit was performed using the data above 214 K, which is the glass transition temperature. Data taken from Meyer *et al.*^[30]

$$\left(\frac{\partial S}{\partial l}\right)_T = -\left(\frac{\partial f}{\partial T}\right)_l \quad (2.21)$$

can be used to rewrite Equation 2.20.

$$f = \left(\frac{\partial U}{\partial l}\right)_T - T \left(\frac{\partial f}{\partial T}\right)_l \quad (2.22)$$

Equation 2.21 and 2.22 provide direct means of determining the internal energy and entropy, therefore they are fundamentally important in the physics of rubber elasticity.

In order to evaluate the two terms, the force on a specimen which is stretched to a constant length is recorded with varying temperature. Meyer and Ferri performed an experiment where they recorded the tension of a rubber specimen under constant length with varying temperature.^[30] In their work, the tension was plotted as a function of absolute temperature as shown in Figure 2.2. A straight line was obtained above a critical temperature of 214 K in Figure 2.2. This critical temperature is the glass transition temperature of rubber. The line nearly crosses the origin by extrapolation. As can be understood from Equation 2.22, the vertical intercept of the extrapolated line gives the differential of the internal energy of the rubber. The internal energy term $\frac{\partial U}{\partial l}T$ is significantly smaller than the entropy term $-T\left(\frac{\partial f}{\partial T}\right)_l$ at room temperature (about 300 K). This means that the elastic force of rubber mostly arises from entropy above the glass transition temperature. For simplicity $U = 0$ is assumed and the work done

to the rubber,

$$W = A = U - TS, \tag{2.23}$$

becomes

$$W = -TS. \tag{2.24}$$

Equation 2.24 is the foundation of the classical theory of rubber elasticity. The strain-energy function and stress-strain function will be derived based on this equation.

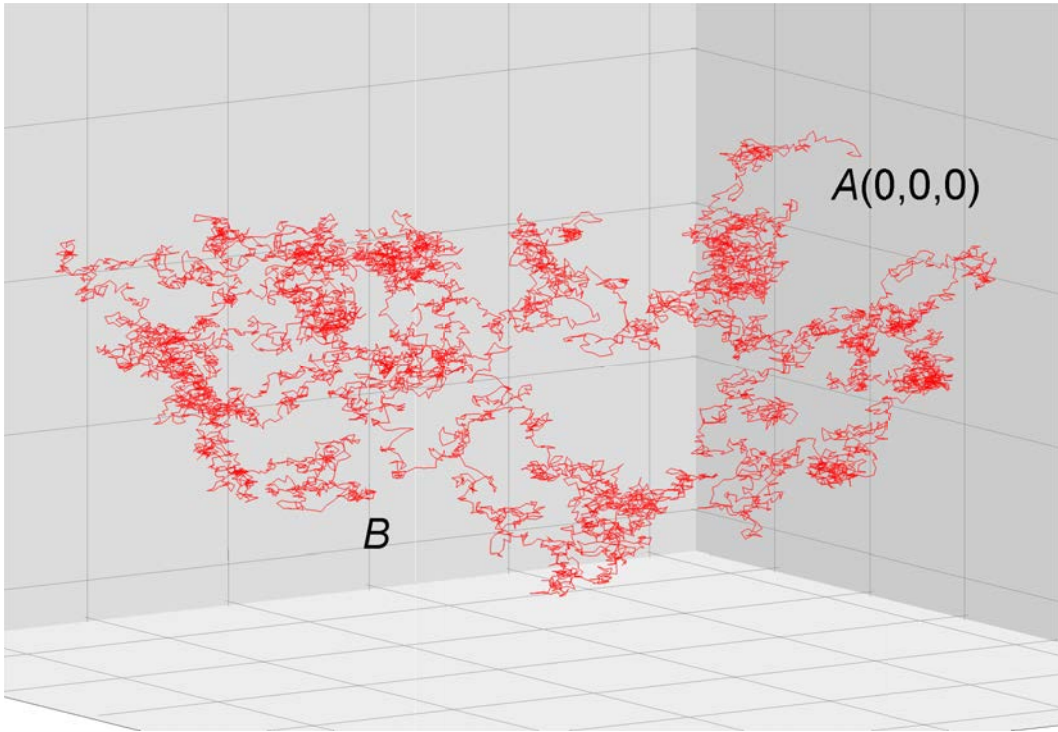


Figure 2.3: Illustration of a computer generated ideal chain with 10000 segments created by the author.

2.2.2 Kinetic theory of rubber elasticity (Neo-Hookean model)

In the previous section, it was shown that the Helmholtz free energy and the stress-strain relationship of rubber can be attributed to its entropy. We consider a randomly-jointed chain with one end, A, is fixed at the origin of a Cartesian coordinate system as shown in Figure 2.3. The other end, B, is allowed to move in a random fashion. The entropy of a randomly-jointed chain can be calculated from Boltzmann's equation as

$$s = k \{ \ln p(x, y, z) d\tau \}. \quad (2.25)$$

where k is the Boltzmann constant, $p(x, y, z)$ is a function that gives the probability density according to the position of B specified in Cartesian coordinates^[28] and s is the entropy of a single polymer chain. Multiplying this by a volume element $d\tau$ gives the probability of B to be found in the vicinity of point (x, y, z) . The formulation of this function is

$$p(x, y, z) = (b^3/\pi^{3/2}) \exp \{ -b^2(x^2 + y^2 + z^2) \}. \quad (2.26)$$

where

$$b^2 = 3/2nl^2 \quad (2.27)$$

where n is the number of bonds in the chain and l is the bond length. By substituting $x^2 + y^2 + z^2 = r^2$ we get

$$p(x, y, z) = (b^3/\pi^{3/2}) \exp(-b^2r^2). \quad (2.28)$$

Therefore, Equation 2.25 becomes

$$s = k \{ \ln(\text{constant}) - b^2r^2 + \ln d\tau \}, \quad (2.29)$$

where k is the Boltzmann constant. Equation 2.29 can be further simplified as

$$s = c - kb^2r^2. \quad (2.30)$$

The Helmholtz free energy is given by

$$A = -Ts = -T(c - kb^2r^2), \quad (2.31)$$

therefore the work required to stretch the chain from distance r to $r + dr$ is

$$\frac{\partial W}{\partial r} = \frac{\partial A}{\partial r} = -T \frac{ds}{dr} = 2kTb^2r. \quad (2.32)$$

We have arrived at a simple expression which relates the entropy of the chain to the tension required to stretch it. By further consideration, it is possible to obtain a function that relates the principal stretch ratios to the energy of the rubber by assuming affine deformation. The derivation of the strain-energy function is based on the previous discussion of a single chain. It requires the change in the end-to-end distance of the chain to be expressed in terms of principal stretch ratios. By considering the entropies of all the chains included in a unit volume of rubber, the strain-energy function of rubber is given as:

$$W = \frac{1}{2}nkT(\lambda_1^2 + \lambda_2^2 + \lambda_3^2 - 3) \quad (2.33)$$

where W is the Helmholtz energy per unit volume which typically takes the unit Jm^{-3} , n is the number of chains per unit volume of rubber and λ_1 , λ_2 and λ_3 are the principal stretch ratios. Note that W must be multiplied by the volume in order to acquire the Helmholtz free energy. nkT is equivalent to the shear modulus μ , therefore

$$nkT = \mu. \quad (2.34)$$

The stretch ratios can be defined in terms of the strain ϵ_i as

$$\lambda_i = 1 + \epsilon_i, \quad (2.35)$$

or by the length of the specimen before l_{i0} and after l_i deformation in the principal directions.

$$\lambda_i = l_i/l_{i0} \quad (2.36)$$

One of the most important concepts with regards to the stretch ratio of rubber is the incompressibility. Because the volume of rubber is nearly conserved during deformation,

$$\lambda_1\lambda_2\lambda_3 = 1. \quad (2.37)$$

2.2.3 Nominal stress and true stress of Neo-Hookean rubber

Equations which relate the deformations such as uniaxial extension and biaxial extension can be derived from Equation 2.33 by partial differentiation. First, λ_2 and when possible λ_3 are eliminated using Equation 2.37. When the rubber is uniaxially stretched in the direction of λ_1 , $\lambda_2 = \lambda_3 = \lambda_1^{-0.5}$ is satisfied as shown in Figure 2.4. There is no other force acting on the specimen to perform any work. W can be expressed in terms of λ_1 only as

$$W = \frac{1}{2}\mu(\lambda_1^2 + 2/\lambda_1 - 3). \quad (2.38)$$

The nominal stress, which is the force divided by the unit *unstrained* area (equivalent to the engineering stress), becomes

$$s_1 = \frac{\partial W}{\partial \lambda_1} = \mu(\lambda_1 - 1/\lambda_1^2). \quad (2.39)$$

Similarly, W of the general biaxial extension is

$$W = \frac{1}{2}\mu(\lambda_1^2 + \lambda_2^2 + 1/\lambda_1\lambda_2 - 3). \quad (2.40)$$

In this situation there are two principal planes the force is acting on, but the nominal stress can be calculated from $\frac{\partial W}{\partial \lambda_1}$ as before,

$$s_1 = \frac{\partial W}{\partial \lambda_1} = \mu(\lambda_1 - 1/\lambda_1^3\lambda_2^2). \quad (2.41)$$

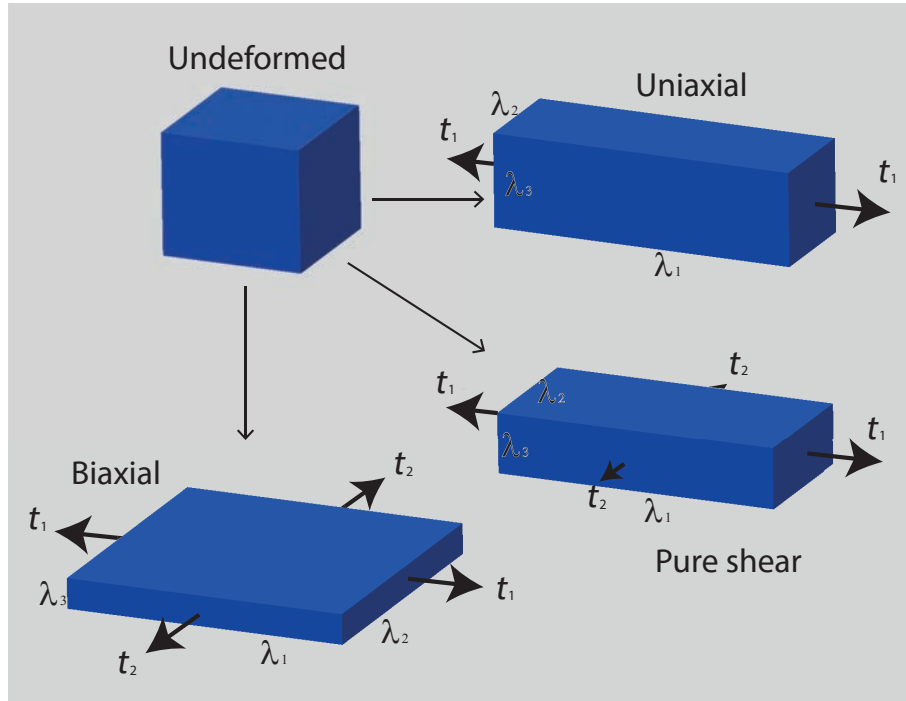


Figure 2.4: Illustration of various types of deformation. The black arrows indicate the tensions applied to the rubber cube.

There are two special cases in biaxial extension. One is equibiaxial extension where

$$\lambda_1 = \lambda_2. \quad (2.42)$$

Substituting this into Equation 2.41 gives

$$s_1 = \frac{\partial W}{\partial \lambda_1} = \mu(\lambda_1 - 1/\lambda_1^5). \quad (2.43)$$

Another case is pure shear where $\lambda_2 = 1$. The nominal stress of pure shear is

$$s_1 = \frac{\partial W}{\partial \lambda_1} = \mu(\lambda_1 - 1/\lambda_1^3). \quad (2.44)$$

The corresponding true stress t_1 , which is the force divided by the unit *strained* area, can be obtained by taking into account the change in the cross-sectional area before (A_0) and during (A) the deformation,

$$t_1 = s_1 A / A_0 = s_1 \lambda_2 \lambda_3 = s_1 \lambda_1, \quad (2.45)$$

therefore the true stress of uniaxial extension is

$$t_1 = \mu(\lambda_1^2 - 1/\lambda_1). \quad (2.46)$$

Likewise, the true stress of general biaxial extension is

$$t_1 = \mu(\lambda_1^2 - 1/\lambda_1^2\lambda_2^2), \quad (2.47)$$

of equibiaxial extension is

$$t_1 = \mu(\lambda_1^2 - 1/\lambda_1^4), \quad (2.48)$$

and of pure shear is

$$t_1 = \mu(\lambda_1^2 - 1/\lambda_1^2). \quad (2.49)$$

Since rubbers are isotropic, the derivation of s_2 and s_3 are equivalent to s_1 , while t_2 and t_3 are equivalent to t_1 . Materials that follow the above constitutive equations are often referred to as “Neo-Hookean materials”. The following chapters will use this terminology when referring to the constitutive equations.

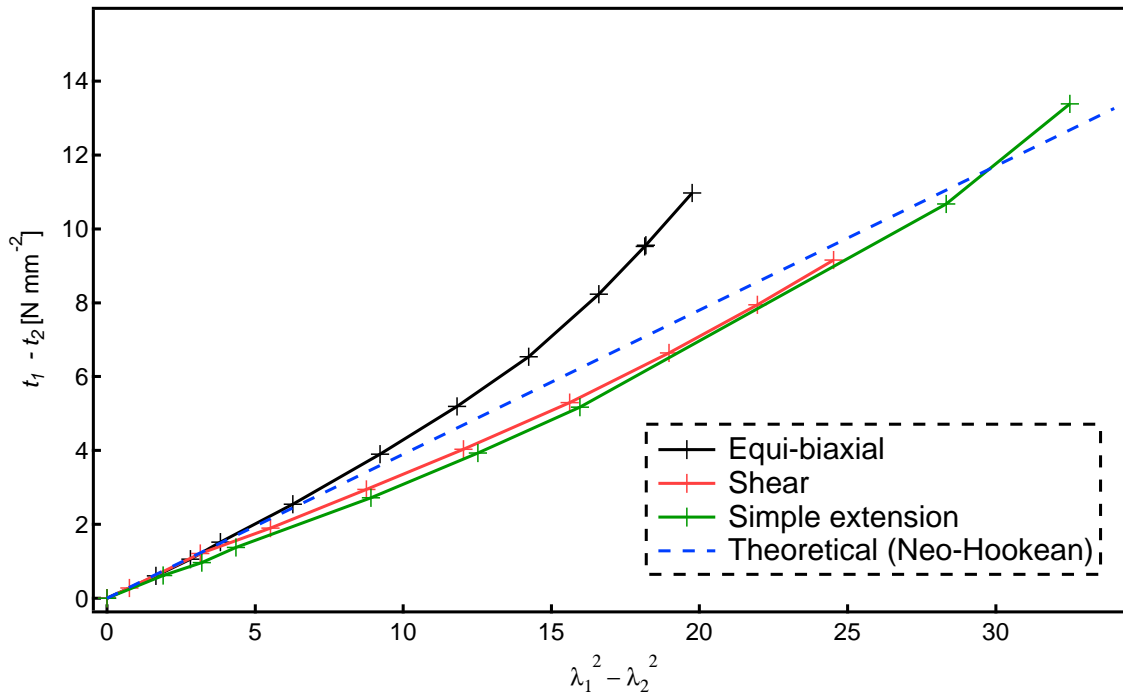


Figure 2.5: $t_1 - t_2$ plotted as a function of $\lambda_1^2 - \lambda_2^2$. Data taken from Treloar.^[28]

2.2.4 The Mooney-Rivlin theory

In the previous section, the kinetic theory of rubber elasticity (Neo-Hookean model) was discussed. As all mathematical models, the Neo-Hookean model has its limitations and cannot accurately reproduce the stress-strain relationship of rubber under large deformation. In order to create a clear contrast between the theoretical and the actual behaviour of rubbers under various types of deformations, it is most convenient to plot $t_1^2 - t_2^2$ of specific types of deformation as a function of $(\lambda_1^2 - \lambda_2^2)$ as shown in Figure 2.5. In this plot, the Neo-Hookean model predicts a straight line with a gradient of μ , regardless of how the rubber is deformed.

There are two differences between the theory and the real behaviour of rubbers that can be seen in the plot. Firstly, although the theory accurately reproduces the stress-strain behaviour of the rubber at low strain, it gradually deviates with increasing strain. Secondly, the experimental curves diverge in different directions depending on the type of deformation, which means that no single parameter can represent the elasticity.

Given these limitations of the kinetic theory of rubber, a model that is capable of compensating such deviations is desirable. Among all hyperelastic constitutive laws apart from the kinetic theory of rubber, the Mooney-Rivlin model is the most commonly used theory due to its simplicity and capability of accurately reproducing the stress and strain behaviour of real rubbers. While the kinetic theory of rubber is based on a molecular model, which attributes the entire Helmholtz free energy of rubber to the entropy of idealised polymer chains, the theory of Mooney and Rivlin is a phenomenological theory. It was not developed from a physical concept, but from

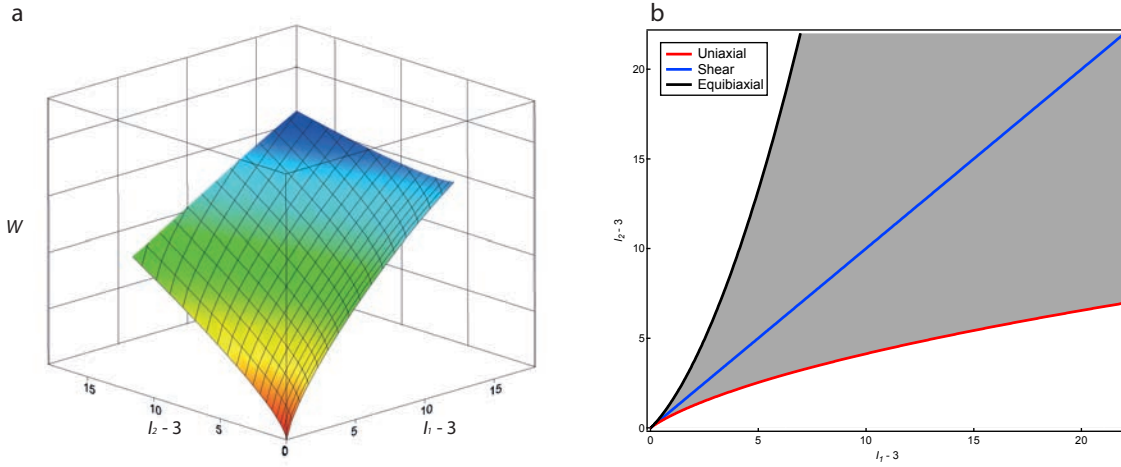


Figure 2.6: (a) Distribution of W of an arbitrary Mooney-Rivlin material represented by a curved surface. (b) Relation between I_1 and I_2 for uniaxial extension, shearing and equibiaxial extension.

mathematical reasoning.^[28] In order to formulate the theory, it is necessary to introduce the concept of strain invariants. The Mooney-Rivlin theory for incompressible materials requires two strain invariants, which are

$$I_1 = \lambda_1^2 + \lambda_2^2 + \lambda_3^2 \quad (2.50)$$

$$I_2 = \lambda_1^{-2} + \lambda_2^{-2} + \lambda_3^{-2}. \quad (2.51)$$

In this theory, the Helmholtz free energy is determined as a function of I_1 and I_2 in the first instance. This formulation is introduced based on the assumption that rubbers are incompressible and isotropic in their unstrained state. The free energy of an isotropic material should not depend on the frame of reference, and W is symmetrical with respect to the three principal stretch ratios.^[28] These requirements are satisfied by defining W in terms of I_1 and I_2 .

Using the two strain invariants $I_1 - 3$ and $I_2 - 3$ as the x and y axes, the Helmholtz free energy of a Mooney-Rivlin material can be represented as a surface in a three dimensional space as shown in Figure 2.6 (a). When the surface is flat, the simplest formulation of the Mooney-Rivlin equation, the first-order Mooney-Rivlin equation is sufficient to reproduce the surface.

$$\begin{aligned} W &= C_1(I_1 - 3) + C_2(I_2 - 3) \\ &= C_1(\lambda_1^2 + \lambda_2^2 + \lambda_3^2 - 3) + C_2(\lambda_1^{-2} + \lambda_2^{-2} + \lambda_3^{-2} - 3) \end{aligned} \quad (2.52)$$

I_1 and I_2 can be regarded as independent variables of W ,^[28] but because I_1 and I_2 are both functions of λ_1 , λ_2 and λ_3 , they are subject to constraints and can only assume

values that are within the shaded region of Figure 2.6 (b). For $C_2 = 0$, the equation reduces to the Neo-Hookean law, with

$$2C_1 = \mu. \quad (2.53)$$

When the surface is curved, it may be reproduced by the sum of a series of terms,

$$W = \sum_{i=0, j=0}^{\infty} C_{ij} (I_1 - 3)^i (I_2 - 3)^j, \quad (2.54)$$

involving powers of $(I_1 - 3)$ and $(I_2 - 3)$.^[28] Since there is no physical model behind the theory, the coefficients must be determined from experiments.

Based on the above energy density functions, the nominal stress and true stress can be calculated from partial derivative functions of W , which can be derived in a similar way as in the kinetic theory. For example, the nominal stress of a first-order Mooney-Rivlin material can be derived as

$$\begin{aligned} dW &= \frac{\partial W}{\partial I_1} dI_1 + \frac{\partial W}{\partial I_2} dI_2 \\ \frac{dW}{d\lambda_1} &= \frac{\partial W}{\partial I_1} \frac{dI_1}{d\lambda_1} + \frac{\partial W}{\partial I_2} \frac{dI_2}{d\lambda_1} \\ &= \frac{\partial W}{\partial I_1} \frac{d(\lambda_1^2 + \lambda_2^2 + \lambda_3^2)}{d\lambda_1} + \frac{\partial W}{\partial I_2} \frac{d(\lambda_1^{-2} + \lambda_2^{-2} + \lambda_3^{-2})}{d\lambda_1} \\ &= \frac{\partial W}{\partial I_1} \frac{d(\lambda_1^2 + 2\lambda_1^{-1})}{d\lambda_1} + \frac{\partial W}{\partial I_2} \frac{d(\lambda_1^{-2} + 2\lambda_1)}{d\lambda_1} \\ &= \frac{\partial W}{\partial I_1} (2\lambda_1 - 2\lambda_1^{-2}) + \frac{\partial W}{\partial I_2} (-2\lambda_1^{-3} + 2) \\ &= 2(\lambda_1 - 1/\lambda_1^2) \left(\frac{\partial W}{\partial I_1} + \frac{\partial W}{\partial I_2} / \lambda_1 \right) \\ &= 2(\lambda_1 - 1/\lambda_1^2) (C_1 + C_2/\lambda_1). \end{aligned}$$

Various forms of first-order Mooney-Rivlin equations of nominal and true stress can be derived similarly. Presenting all the steps for each equation is unnecessary, especially because it was done for the kinetic theory. Therefore, a summary of the equation of nominal stress and true stress of the first-order Mooney-Rivlin equations is given below without the derivation.

Uniaxial extension

$$\begin{aligned} s_1 &= 2(\lambda_1 - 1/\lambda_1^2)(C_1 + C_2/\lambda_1) \\ t_1 &= 2(\lambda_1^2 - 1/\lambda_1)(C_1 + C_2/\lambda_1) \end{aligned}$$

General biaxial extension

$$\begin{aligned} s_1 &= 2(\lambda_1 - 1/\lambda_1^3\lambda_2^2)(C_1 + C_2\lambda_2^2) \\ t_1 &= 2(\lambda_1^2 - 1/\lambda_1^2\lambda_2^2)(C_1 + C_2\lambda_2^2) \end{aligned}$$

Equibiaxial extension

$$\begin{aligned} s_1 &= 2(\lambda_1 - 1/\lambda_1^5)(C_1 + C_2\lambda_1^2) \\ t_1 &= 2(\lambda_1^2 - 1/\lambda_1^4)(C_1 + C_2\lambda_1^2) \end{aligned}$$

Pure shear

$$\begin{aligned} s_1 &= 2(\lambda_1^1 - 1/\lambda_1^3)(C_1 + C_2) \\ t_1 &= 2(\lambda_1^2 - 1/\lambda_1^4)(C_1 + C_2) \end{aligned}$$

In order to evaluate the elastic behaviour of balloons, the equation for equibiaxial stretching will be compared to experiments and the kinetic theory in Section 7 and 10.

2.3 Forces acting on curved surfaces under pressure differences

The mechanics of curved surfaces, which includes air-liquid interfaces and rubber membranes are reviewed. The following subsections includes abbreviations of Müller,^[29] Erbil^[31] and Buttz.^[32]

2.3.1 Hoop stress and pressure radius characteristics of rubber balloons

As a first step to develop an understanding of the deformation process of membranes under a pressure difference, the mechanics of a spherical balloon is considered. The stress on the membrane of a balloon is called the hoop stress. One of the aims of this section is to derive an equation for the hoop stress of spherical shells or balloons. We assume that the rubber membrane of the balloon is uniform and the stress within the membrane is much greater than the pressure difference. Also, we assume that the membrane thickness, H , is much smaller than the radius of the balloon, R ($R \gg H$). The balloon inflates by increasing pressure difference while maintaining its spherical form. The membrane undergoes uniform equibiaxial stretching,

$$\lambda_1 = \lambda_2 = \frac{R}{R_0}, \quad (2.55)$$

where λ_1 and λ_2 are the two principal stretch ratios parallel to the balloon surface and R and R_0 are the deformed and undeformed radii of the balloon respectively. From volume conservation:

$$\lambda_3 = \frac{1}{\lambda_1 \lambda_2} = \left(\frac{R_0}{R} \right)^2, \quad (2.56)$$

The thickness during deformation is

$$H = H_0 \lambda_3, \quad (2.57)$$

where H and H_0 are the deformed and undeformed thickness of the membrane. We now consider the force acting on the inflated balloon. Figure 2.7 shows the cross-section of the balloon cut into half at the equator. The overall force, F , created by the pressure difference, ΔP , is acting on the cross-section of the membrane.

$$F = \pi R^2 \Delta P \quad (2.58)$$

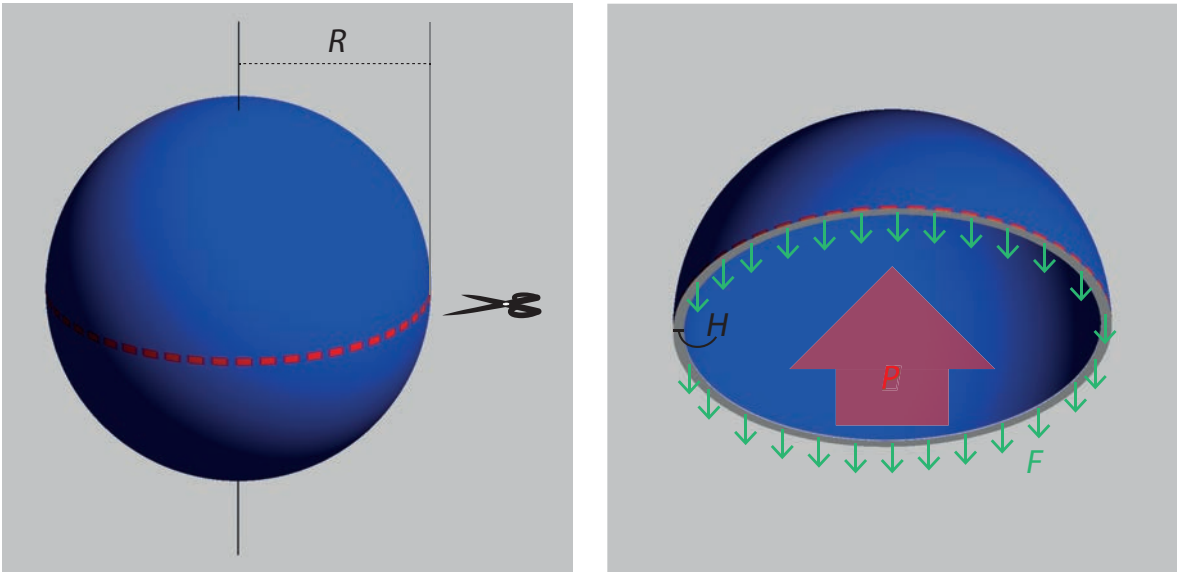


Figure 2.7: Illustration of of spherical balloon and the cross-section.

The balloon is stationary, therefore there must be a counterbalancing force with the same magnitude as F , but acting in the opposite direction. Dividing the force by the area of the membrane cross-section A , where A can be written as

$$A = 2\pi RH, \quad (2.59)$$

will give the true stress t :

$$t_1 = t_2 = \frac{F}{A} = \frac{\pi R^2 \Delta P}{2\pi RH} = \frac{R\Delta P}{2H}. \quad (2.60)$$

Equation 2.60 can be used to analyse the stress and strain of spherical balloons, or of any thin membrane/wall with a spherical curvature under pressure difference, including boilers and gas cylinders. This equation can be used for studying the material properties of flat sheets by inflating the sheet into an axisymmetric form. Such tests are called “bulge tests“.

Assuming the membrane of the spherical balloon to be a Neo-Hookean material, equation 2.48 and 2.60 will allow ΔP to be expressed in terms of λ_1 as

$$\frac{R\Delta P}{2H} = \mu \left(\lambda_1^2 - \frac{1}{\lambda_1^4} \right). \quad (2.61)$$

Rewriting Equation 2.61 in terms of its radius by substituting equation 2.55 into 2.61 and we get

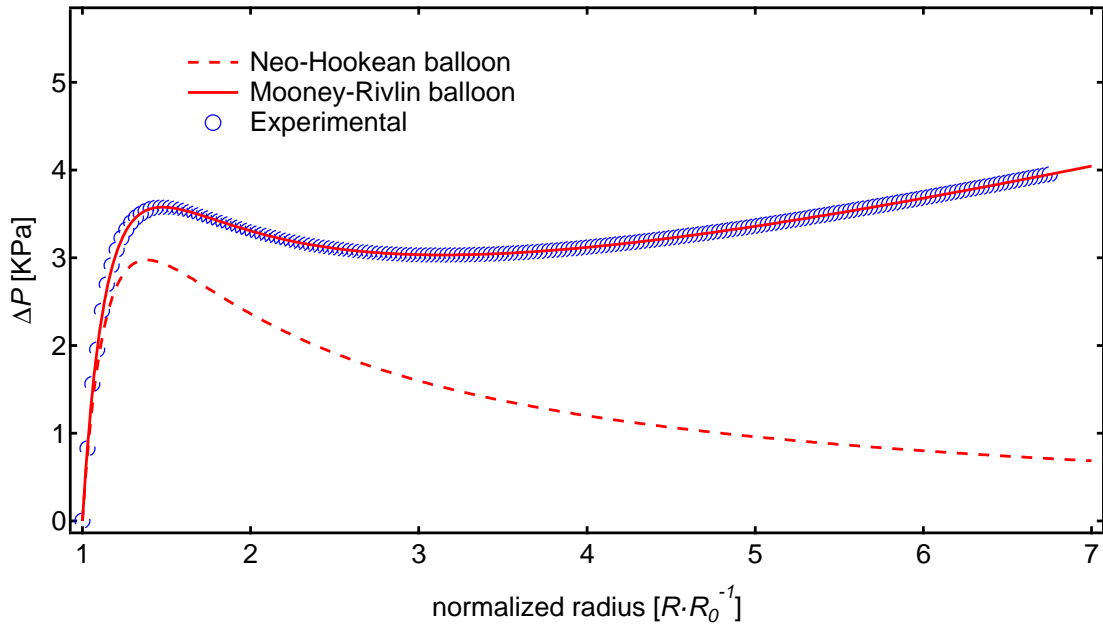


Figure 2.8: Pressure-radius curves of spherical balloons. Neo-Hookean balloon ($\mu = 300$ KPa), Mooney-Rivlin balloon ($C_1 = 150$ KPa, $C_2 = 15$ KPa) are compared to a real balloon. Data taken from Müller *et al.*^[29]

$$\Delta P = \frac{2H_0}{r_0} \mu \left[\frac{R_0}{R} - \left(\frac{R_0}{R} \right)^7 \right]. \quad (2.62)$$

We now have an equation which describes the relationship of the pressure difference and the radius of the balloon. A similar equation for spherical balloons made from a Mooney-Rivlin material can be derived in a similar fashion,

$$\Delta P = \frac{4H_0 C_1}{r_0} \left[\frac{R_0}{R} - \left(\frac{R_0}{R} \right)^7 \right] \left[1 + C_2 \left(\frac{R}{R_0} \right) \right]. \quad (2.63)$$

The pressure-radius curves of spherical balloons calculated from equations 2.62 and 2.63 are shown in Figure 2.8. The curve of the Neo-Hookean balloon significantly differs from the experimental result, while the Mooney-Rivlin Balloon reproduces the experiment very accurately. At a constant pressure difference, the Neo-Hookean balloon is unstable at $R/R_0 > 1.4$ and will inflate to infinite radius. As shown in Figure 2.8, such behaviour is not seen in real spherical balloons, and it is therefore emphasised that the choice of the constitutive equation is a crucial factor for modelling realistic balloons.

Another interesting fact is that the Mooney-Rivlin balloon also has a descending branch between $1.5 < R/R_0 < 3$. In this region, spherical balloons are unstable. If two

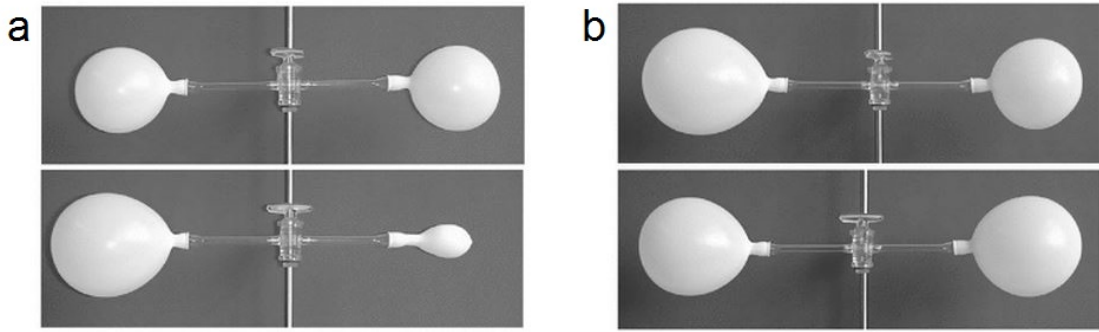


Figure 2.9: (a) Symmetry breaking of the radii of two connected balloons. Top: before opening the tap. Bottom: after opening the tap. (b) Largely inflated balloons become symmetric when the Tap is opened. Top: before opening the tap. Bottom: after opening the tap. Photographs taken from Müller *et al.*^[29]

balloons are inflated to this region and connected to each other, symmetry breaking will occur as shown in Figure 2.9.^[29,33] A similar phenomena can be also seen in soap bubbles,^[34] but the presence of distinct stable/unstable regions, which correspond to the ascending/descending branches, is unique to rubber balloons.

2.3.2 Surface tension and rubber elasticity

The fundamental theory of surface tension is described and the mechanical properties of liquid films are compared to that of rubber membranes.

Inflating a balloon is somewhat similar to inflating a soap bubble. This is not only true in the sense that both are enjoyable activities, but also in a scientific sense. Surface chemistry, which provides fundamental laws to describe soap bubbles, also provides useful insights for studying balloons. In order to clearly understand the similarity and the difference between soap bubbles and balloons, the basic definition of surface tension will be examined and liquid films will be compared to rubber films.

We consider the following experiment in order to define surface tension.^[32] A liquid film is formed in a rectangular frame. One end of the frame consists of a mobile slider which moves without any friction as shown in Figure 2.10. The work dG is done to move the bar to the right. dG is proportional to the newly formed surface dA and scales with a factor of γ , hence

$$dG = \gamma dA = 2\gamma b dx. \quad (2.64)$$

γ is called surface tension. The coefficient 2 is necessary because the front and back surfaces of the film are both considered. Equation 2.64 holds not only for infinitesimal changes of A but also for significant increases of the surface area, therefore

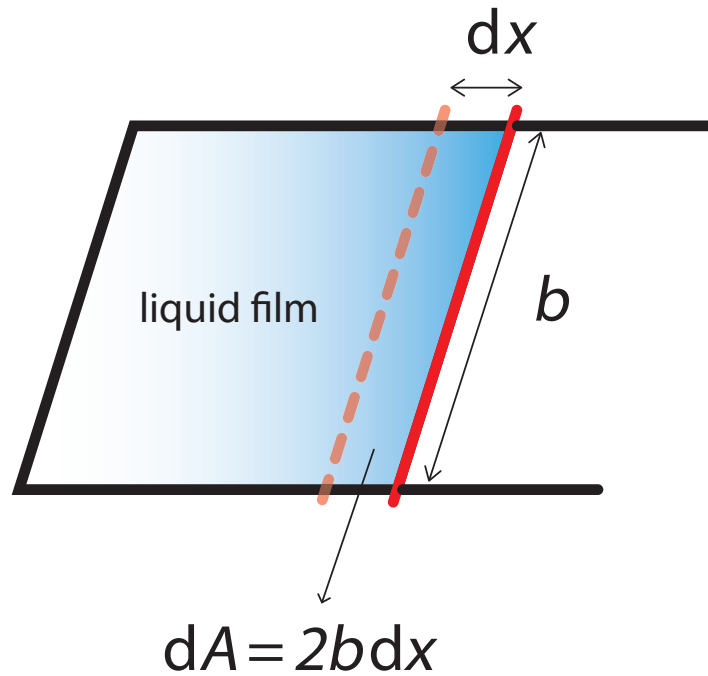


Figure 2.10: The definition of surface tension can be explained by an experiment illustrated above, where work is done on a liquid film in a rectangular frame to expand its area.

$$\Delta G = \gamma \Delta A. \quad (2.65)$$

In general, γ depends on the composition of the liquid phase and the gas phase, temperature, and pressure, but it is independent of the area increase.

Since we are also interested in rubber elasticity, it is worthwhile defining surface tension in terms of applied force. If we define F in such a way that it will take a positive value for a positive displacement, F can be written as

$$F = \frac{dG}{dx} = 2\gamma b. \quad (2.66)$$

We would like to compare liquid surfaces to rubber membranes. If we deform a rubber membrane in a similar way to Figure 2.10, such deformation is pure shear. Using Equation 2.43,

$$F = A_0 \frac{\partial W}{\partial \lambda_1} = A_0 \mu (\lambda_1 - 1/\lambda_1^3). \quad (2.67)$$

As Equation 2.67 suggests, the force will increase by the amount of stretch ratio. If the undeformed rubber is a square membrane with sides of unit length, Equation 2.67

can be re-written as

$$F = H \frac{\partial W}{\partial x} = H\mu(x - 1/x^3). \quad (2.68)$$

The force acting on the rubber membrane is now expressed in terms of displacement in Equation 2.68. In principle, an external observer should not be able to distinguish between a liquid film and a rubber membrane from the force when the displacement is above $x \geq 0$, especially when the rubber membrane is thin enough so that the surface free energy of the liquid and the Helmholtz free energy of the rubber becomes comparable to the liquid. For example, when a 1 μm thick PDMS film with a shear modulus of $\mu = 500$ KPa is stretched by 5%, $H \frac{\partial W}{\partial x}$ becomes comparable to the surface tension of water at room temperature:

$$10^{-6} \times \frac{\partial W}{\partial x} \approx \gamma_{aq} \text{ (at a strain of 5\%.)} \quad (2.69)$$

If the rubber film is as thin as $H = 100$ nm, the effect of surface tension will become sufficient to have an impact on the shape of the film at equilibrium. In order to accurately describe thin rubber films in this regime, the following net free energy function,

$$E = VW + G, \quad (2.70)$$

should be used. E is the net free energy and V is the volume of the film. The effect of surface tension on the equilibrium conformation of thin rubber films is discussed in detail in Chapter 6.

2.3.3 Young-Laplace equation

A basic definition of surface tension was introduced in the previous section, and the similarities and differences of liquid films and rubber membranes were discussed. We would now like to use these insights to examine the equations which govern the relationship between a pressure difference and the radius of curvature. In order to define the radii of curvature of the surface (mnp), the curved surface is sliced with two perpendicular planes as shown in Figure 2.11. The intersections of the planes and the curved surface form arcs, and the radii of curvature of these arcs are defined as R_1 and R_2 , and the lengths of the arcs are defined as x and y , respectively. We assume that the curved surface moves outwards by a small distance, dz , to a new position ($m'n'p'r'$). The arc lengths have increased from x and y to $(x + dx)$ and $(y + dy)$ as shown in Figure 2.11 and the area of the interface has increased by dA . dA can be written as

$$dA = (x + dx)(y + dy) - xy = xdx + ydy + dxdy \approx xdy + ydx. \quad (2.71)$$

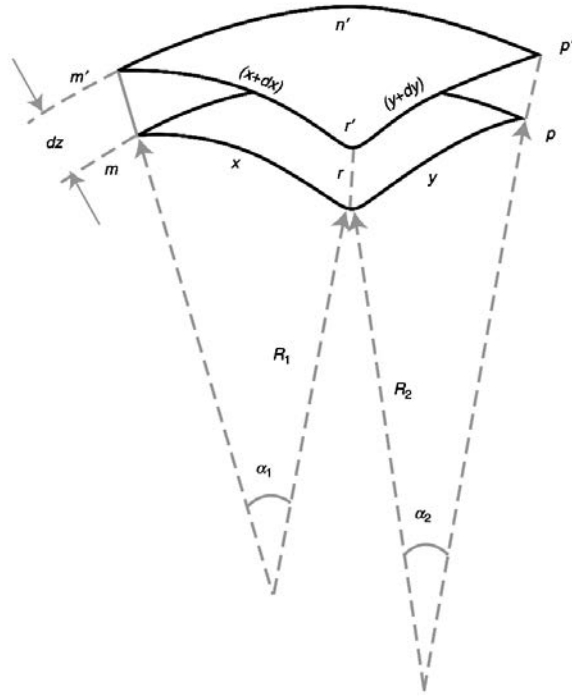


Figure 2.11: Schematic illustration of three-dimensional curvature using plane geometry concepts. Reprinted from Erbil.^[31]

The change in the surface area will increase the surface free energy, which is given by

$$dG = \gamma(xdy + ydx). \quad (2.72)$$

$$PdV = Pxydz = \gamma(xdy + ydx) \quad (2.73)$$

The vertices of the surface lie along the extension of the new diverging radial lines, therefore the radian angles α_1 and α_2 , which are defined as $\alpha_1 = \frac{x}{R_1}$ and $\alpha_2 = \frac{y}{R_2}$, are kept constant before and after the displacement of the interface. Such conservation of radian angles will lead to

$$\frac{x + dx}{R_1 + dz} = \frac{x}{R_1}, \quad (2.74)$$

which simplifies to

$$\frac{dx}{xdz} = \frac{1}{R_1}. \quad (2.75)$$

Equivalently for y and R_2 ,

$$\frac{dy}{ydz} = \frac{1}{R_2}. \quad (2.76)$$

By substituting Equation 2.75 and 2.76 into 2.73, the Young-Laplace equation,

$$\Delta P = \gamma \left(\frac{1}{R_1} + \frac{1}{R_2} \right), \quad (2.77)$$

is obtained. For $R_1 = R_2$, Equation 2.77 can be further simplified as

$$\Delta P = \gamma \frac{2}{R}, \quad (2.78)$$

which is the special form of Young-Laplace equation for spherical interfaces. Of course, equation 2.78 holds even when the interface is overall not a sphere, as long as $R_1 = R_2$ at the point of interest.

2.3.4 From Young-Laplace equation to the hoop stress of balloons

Section 2.3.1 derived the hoop stress of a spherical balloon with a uniform membrane thickness. Equation 2.60 can be used for analysing bulge tests, but one may question whether such usage is truly valid. The concern comes from the possibility that the specimen may deform into a non-spherical shape with a non-uniform thickness distribution, and violate the assumptions of Equation 2.60 valid. Such a worry is reasonable because the derivation relied on the global shape of the balloon, and it is not obvious whether rubber specimens will deform into a spherical form with a uniform thickness during bulge tests. As a matter of fact, the shape *does* deviate from a sphere at large deformation, and the thickness is *not* uniform once it is inflated.

Although the bulge test is an established method for testing rubber sheets, a rigorous proof of Equation 2.60 is not easily found, and it is therefore worthwhile to demonstrate the derivation of Equation 2.60 without relying on the assumptions of spherical form of the balloon and uniform thickness of the rubber membrane. As shown in Section 2.3.3, the pressure difference between a curved interface was described by its radii of curvature and surface tension from the Young-Laplace equation. We would like to show that the same equation can be used for rubber membranes. This will not require information that relies on the global shape, but will only use information that can be acquired from an infinitesimal area.

In Section 2.3.3, the derivation of Young-Laplace equation was carried out in planar geometry. Similar to what was shown previously, we start from considering an equibiaxial expansion of a square interface the sides of which have unit length. The work done to increase an infinitesimal area can be written as

$$dG = \gamma dA = \gamma(xdy + ydx). \quad (2.79)$$

Assuming equibiaxial expansion of a square interface, y can be eliminated from Equation 2.79,

$$dG = 2xdx\gamma. \quad (2.80)$$

Equivalently, dG can be expressed in the form of a total differential as

$$dG = \frac{\partial G}{\partial x}dx + \frac{\partial G}{\partial y}dy \quad (2.81)$$

where

$$\frac{\partial G}{\partial x} = \gamma x \quad (2.82)$$

$$\frac{\partial G}{\partial y} = \gamma y. \quad (2.83)$$

Again, eliminating y from Equation 2.81 gives

$$dG = 2dx \frac{dG}{dx}. \quad (2.84)$$

We now consider a square sheet made of rubber. The sheet has a thickness H and sides with unit length. Under infinitesimal equibiaxial stretching, the work done to the sheet is

$$\begin{aligned} VdW &= HdW \\ &= H \left(\frac{\partial W}{\partial x}dx + \frac{\partial W}{\partial y}dy \right) \\ &= d \left(2dx \frac{dW}{dx} \right) = H \left(2d\lambda \frac{dW}{d\lambda} \right) \end{aligned} \quad (2.85)$$

As we saw previously, W is the Helmholtz free energy per unit volume of the rubber (Pa/m^3), and therefore the volume of the sheet V must be taken into account. When the amount of work done to the interface and the rubber sheet is the same,

$$\gamma dA = dG = HdW \quad (2.86)$$

and finally from Equation 2.78 we get

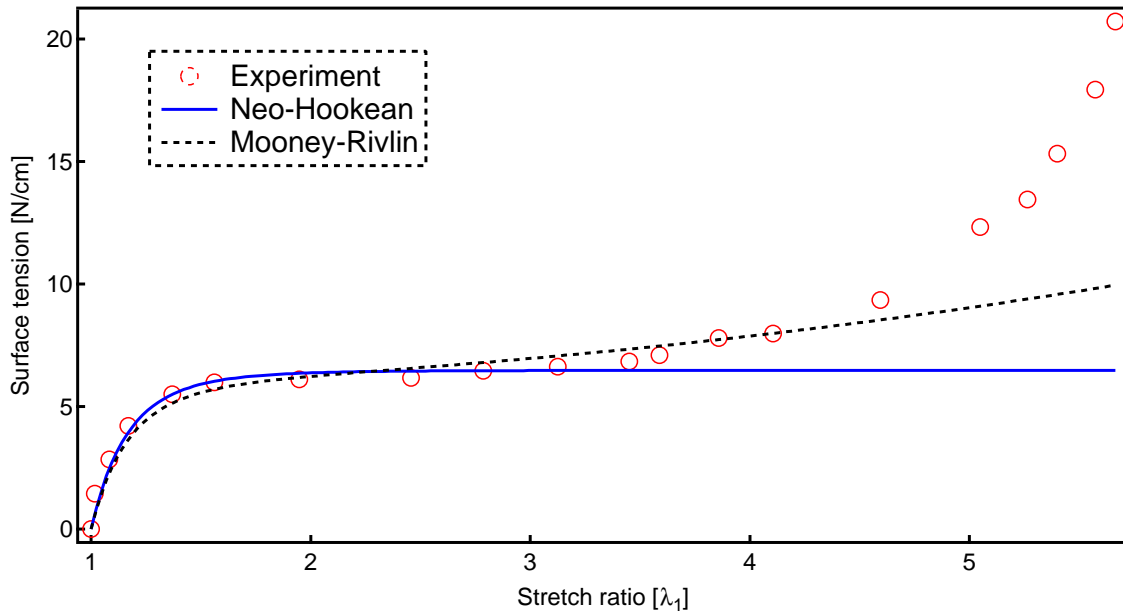


Figure 2.12: Surface tension plotted as a function of stretch ratio. Data taken from Treloar.^[35]

$$\Delta P = H \frac{dW}{dx} \frac{2}{R} = H t_1 \frac{2}{R} \quad (2.87)$$

therefore

$$t_1 = \frac{r \Delta P}{2H}. \quad (2.88)$$

We have arrived at an equation identical to Equation 2.60. Therefore, Equation 2.60 is valid regardless of the global shape of the balloon, as long as the thickness of the balloon is much smaller than its radius of curvature and the pressure inside the balloon is greater than the external pressure. It also does not rely on any constitutive equation and can therefore be used for materials other than rubber, as long as the thickness of the membrane/wall during the test is known.

There are at least two differences between the behaviour of liquid spheres, such as droplets and soap bubbles, and rubber balloons. Firstly, as it has been pointed out previously, the deformation of liquid is a plastic process and flow of the liquid is possible, whereas chemically cross-linked rubbers deform elastically and flow does not occur. Because of this difference,

$$\frac{\partial G}{\partial x} = \frac{\partial G}{\partial y} = \gamma = \text{constant} \quad (2.89)$$

holds regardless of the change in the area, but

$$\frac{\partial W}{\partial x} \neq \frac{\partial W}{\partial y} \quad (2.90)$$

unless

$$\lambda_1 = \lambda_2. \quad (2.91)$$

Equation 2.85 assumed $\frac{\partial W}{\partial x} = \frac{\partial W}{\partial y}$ which is the case only for equibiaxial stretching. In addition, $\frac{\partial W}{\partial x}$ and $\frac{\partial W}{\partial y}$ are functions of temperature and, more importantly in the current context, functions of stretch ratios. This can be easily verified by plotting the “Surface tension” of rubber under equibiaxial tension^[29] as shown in Figure 2.12, where the tension normalised by the length is strongly dependent on the stretch ratio.

Secondly, liquid spheres and spherical balloons will respond differently when they are compressed. While soap bubbles maintain their spherical form when they are compressed or deflated, rubber balloons tend to become flat as we know from experience.

3 Materials and methods

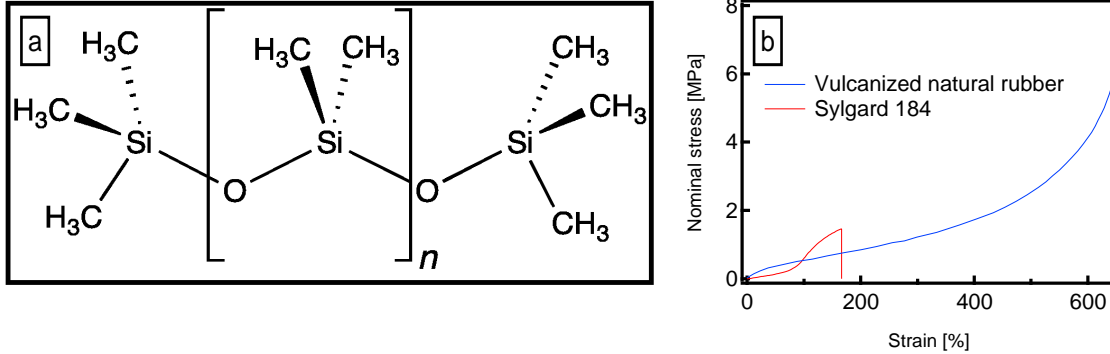


Figure 3.1: (a) Stress-strain curve of PDSM (Sylgard 184)^[36] in comparison to a vulcanized natural rubber with 8% sulphur.^[35] (b) Molecular structure of a linear PDMS molecule. Reprinted with permission.^[37]

In this chapter, materials and techniques which were used in this thesis will be introduced. We will assume that readers will be familiar with conventional methods, which will not be included. Detailed descriptions of these methods can be found in other theses and literature, and comprehensive reviews can be found in.^[12,38–40] The methods that were extensively used can be classified into two main categories: film deposition methods that include spin-coating and blade-coating, and optical methods that include reflection spectra measurement, microscopy and ellipsometry. They will not be described in this chapter.

3.1 Materials

The mechanical property of elastomers in general were introduced in Chapter 2. This section will focus on specific properties of elastomers which were used in this thesis. Three types of elastomers, namely PDMS, PSPI and LCE will be introduced.

3.1.1 PDMS

Polydimethylsiloxane rubber (PDMS) is a low cost elastomer which is chemically stable, non-toxic and optically clear.^[37] It is also known by the name silicone rubber. As the name implies, its backbone chain contains silicon as shown in Figure 3.1 (a). It is used in a wide range of applications such as fluidics (valves, pumps, fluidic circuits), optical systems (adaptive lenses, tilting mirrors) and sensors (acceleration sensors, tactile sensors and chemical sensors).^[41] It has a refractive index of about $n = 1.41$ and has been used as a low refractive index material in the previous work on stretchable DBRs.^[15] Sylgard 184, which is a commercially available PDMS rubber, consists of

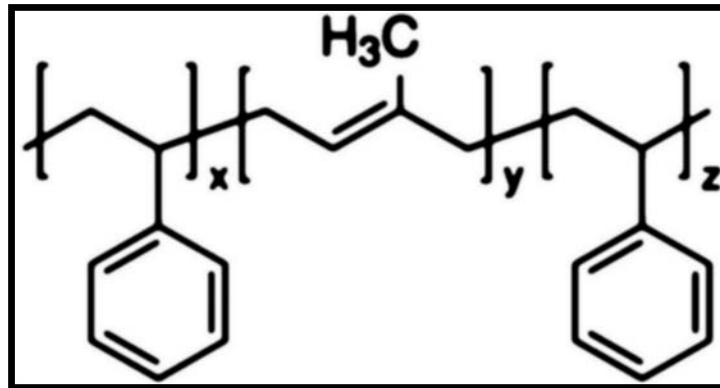


Figure 3.2: Molecular structure of PSPI. Reproduced with permission.^[43]

two components (A and B). In the experiments, the two components were mixed in a ratio of A:B = 10:1 and cured at 100 °C for 1 hour, unless otherwise stated.

The stress-strain curve of PDMS is quite different from vulcanized natural rubber (polyisoprene) as can be seen in Figure 3.1(b). Instead of following the theoretical predictions of the Neo-Hookean model or the Mooney-Rivlin model, the nominal strain of Sylgard 184 increases linearly up to 50% upon uniaxial tension^[36,41,42] as shown in Figure 3.1(b). The stress-strain curve becomes steeper immediately after the linear regime, whereas vulcanized natural rubber undergoes gradual hardening after 200-300% of extension.

The author of this thesis believes that Sylgard 184 is a material suitable for various optical applications, but not necessarily ideal for stretchable substrates when a large deformation is required. This is because hardening (50-100%) and fracture (150%) occurs at relatively low extension,^[36] whereas vulcanized natural rubber can be stretched to a greater extent before hardening and it can reach 500-1000% before fracturing.^[28] The early hardening of Sylgard 184 requires sophisticated clamps that can tolerate the stress for large uniaxial deformation, and the ultimate amount of extension is limited by the fracture limit. However, Sylgard 184 is an excellent substrate for optical measurements due to its smoothness and clarity.

3.1.2 PSPI

Polystyrene-block-Polyisoprene-block-Polystyrene (PSPI) is a thermoplastic elastomer which is used as an adhesive and as a sealant.^[43] It is also used as a constituent in asphalt and oil gels.^[43] It has a refractive index of about $n = 1.53$ and has been used as a high refractive index material in the previous work on stretchable DBRs.^[15] The polystyrene (PS) block and polyisoprene (PI) block are known to microphase separate and form a network structure. Since PS blocks are attached to the two ends of the PI block as shown in Figure 3.2, the PS micelles serve as a physical cross-linker and connects multiple PSPI molecules. Unlike chemical rubbers, no covalent bonds between

individual block copolymer molecules form and the cross-links are reversible. Because of this, the network structure can be rearranged and the material can be moulded by applying heat and pressure, which is not possible for chemically cross-linked elastomers.

The same mechanism can also cause creep during deformation under moderate temperature. The stress-relaxation behaviour of PSPI has been studied by Hotta *et al.*^[44] Their conclusions can be summarized as follows. The two mechanisms responsible for creep in PSPI are: relaxation of dangling chains, and PS chains being pulled out from the cross-linking sites, i.e. the PS micelles. The latter mechanism starts to kick-in only above a critical temperature of 30°C at 20% strain. It was pointed out that the critical temperature may vary depending on the strain. Above the critical temperature, the sample flows plastically and the natural length of the sample will change permanently. PSPI with different polystyrene ratios, namely 14, 18 and 22%, can be purchased from Sigma-Aldrich, of which 22% polystyrene was used in this work.

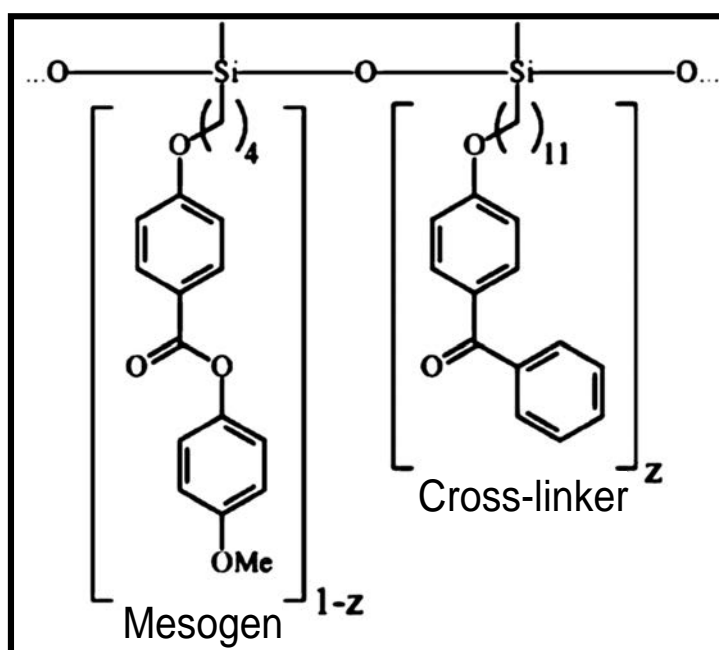


Figure 3.3: Molecular structure of LCE. Reproduced from Sánchez-Ferrer *et al.*^[45]

3.1.3 LCE (side chain nematic liquid crystal elastomer)

Liquid crystal elastomers (LCEs) are a new class of materials that inherit the characteristics of liquid crystals and rubbers. Liquid crystals possess long-range orientational order, but unlike other crystals they are able to flow. Elastomers, on the other hand, are capable of undergoing large deformation as discussed in Chapter 2. A combination of the properties of liquid crystals and elastomers allows LCEs to exhibit unique properties. For example, the mesogens in nematic liquid crystal elastomers can be macroscopically aligned to form monodomains by stretching, which can be stabilised

by two-step cross-linking.^[46] The anisotropy of monodomain LCEs exhibit strong birefringence, which can be used for bifocal lenses.^[47] The monodomain liquid crystal phase can undergo a nematic-isotropic phase transition at a critical temperature which has a significant influence on the conformation of the chains. This leads to a reversible change in the natural length of the LCE.^[48] Sensitising this behaviour to light leads to the application of photo-actuators.^[49]

In this thesis, a side-chain nematic elastomer was used as a high refractive index elastomer. The side-chain nematic elastomer was synthesized from polymethylhydrosiloxane (PMHS), which is the backbone chain, 4-methoxyphenyl 4-(but-3-en-1-yloxy)benzoate (SCM), which is the mesogen, and 4-(undec-10-en-1-yloxy)benzophenone (SCPC), which is the cross-linker. SCM and SCPC are attached to PMHS as shown in Figure 3.3. The molar ratio of SCM and SCPC were set to $M_{SCM} : M_{SCPC} = 9 : 1$.

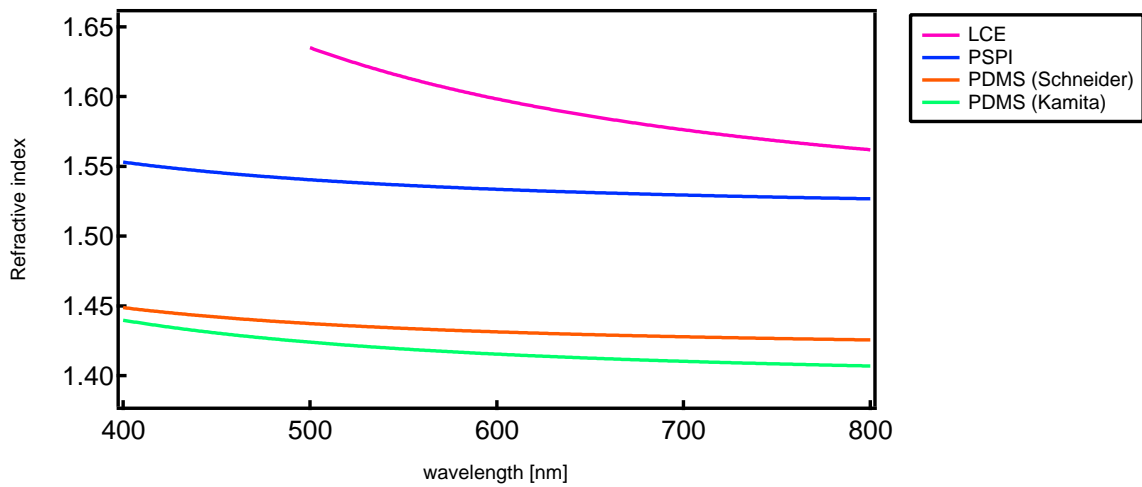


Figure 3.4: Refractive indices of materials. Modelling of the reflectometry results of the LCE by Cauchy’s equation was difficult below 500 nm, therefore only the curve between 500-800 nm is presented. The refractive index of PDMS taken from Schneider *et al.*^[41] and the author’s measurement are displayed.

3.1.4 Refractive index dispersion

The refractive indices of the materials were measured by spectroscopic ellipsometry. The reflectometry results were modelled by Cauchy’s equation and are plotted in Figure 3.4. The refractive index of PDMS found in literature^[41] is also plotted in the graph for comparison.

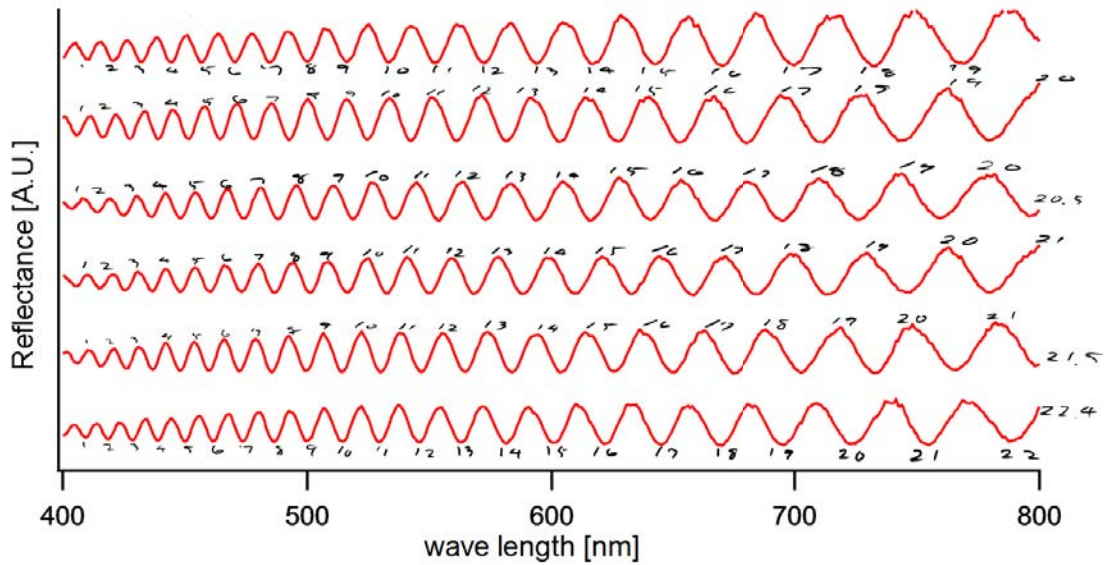


Figure 3.5: An example of a tedious fringe counting performed by the author.

3.2 Approximate calculation of film thickness for automatic film thickness measurements

Optimization of thicknesses of the constituent layers is necessary for fabricating high quality DBRs. This is because the reflection band can be adjusted to a desired wavelength, and moreover the effect of constructive interference is maximised when the optical thicknesses of the constituent layers are both set to $\frac{\lambda}{2}$, as mentioned in Chapter 2. In this study, reflection spectra measurements were chosen to determine film thickness because of their convenience and reliability. Analysis of interference spectra can provide a rapid and accurate means for estimating the thicknesses of thin films. Routines to support spectral analysis were implemented and the details will be discussed in this section.

3.2.1 Primitive approach for film thickness estimation by fringe counting

The simplest method of estimating film thicknesses from spectral measurement results is to count the numbers of maxima within a certain range of wavelengths. Using the Fabry-Perot relationship,

$$m\lambda = 2nl, \quad (3.1)$$

the order of maxima (or minima) m can be deduced for each peak at a wavelength λ , and the approximate value of optical path difference, $2nl$, can be calculated. This so called "fringe counting" is effective but is tedious when carried out manually (see Figure 3.5). As the equation of thin film interference has already been introduced in

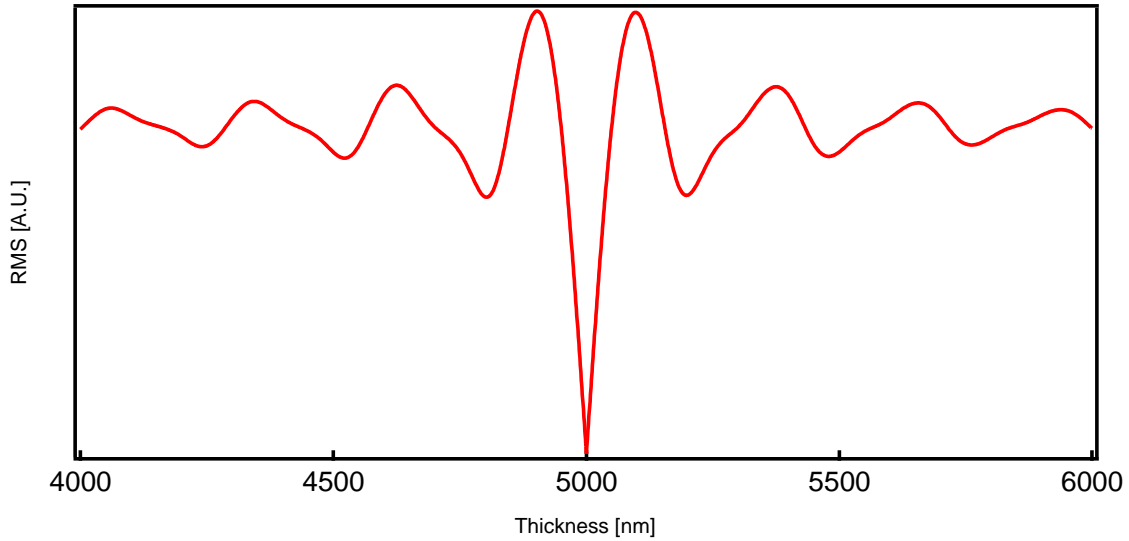


Figure 3.6: Distribution of RMS error of a 5000 nm PDMS (constant refractive index $n = 1.41$) film on silicon substrate. The curve was calculated from Equation 3.2 using a "pseudo" experimental spectrum and calculated spectra. The RMS error is minimized when the thickness of the experimental spectrum and the calculation coincide at 5000 nm.

Chapter 2, it is natural to consider the use of fitting algorithms, such as the least square method, to fit the film thickness. This approach works well with thin films, but not necessarily with thick films because the root mean square

$$y_{rms} = \sqrt{\frac{1}{n}y_1^2 + y_2^2 + y_3^2 + \dots + y_n^2}, \quad (3.2)$$

where y_i is the difference of the data and fitting function at λ_i , has many local minima as shown in Figure 3.6. Finding the right seed value for thick films can be time consuming, and is likely to involve manually counting the fringes in order to get the fit to work. Therefore, a routine that automatically counts the fringes is desirable.

3.2.2 FFT analysis of interference spectra

For the automatic fringe counting, a routine which utilises Fast Fourier Transformation (FFT) was utilised. The algorithm was originally developed by Anglin *et al.*^[50] and was used by many studies that involve optical thickness measurements of porous silicon for bio-sensing.^[50–56] The implementation for this work was developed based on Anglin's method with some modifications. When we transform Equation 3.1 to

$$\frac{m}{2nl} = k, \quad (3.3)$$

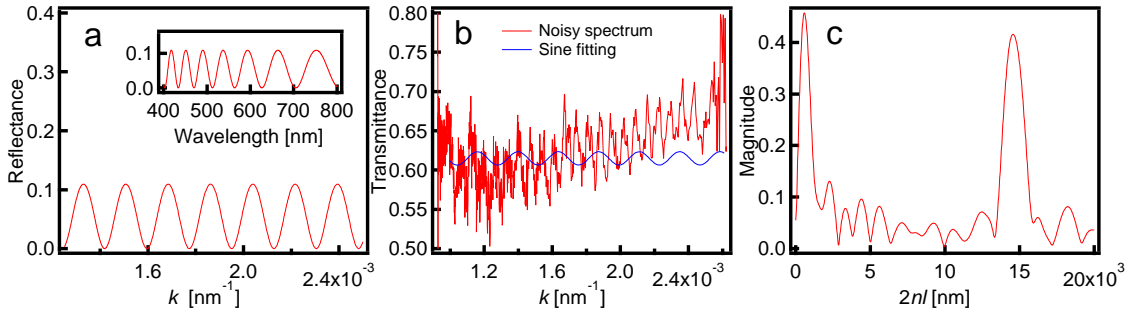


Figure 3.7: (a) Reflection spectrum of a 2000 μm PDMS ($n = 1.41$) film plotted with respect to frequency. The inset figure is the same spectrum plotted with respect to wavelength (b) Unsuccessful attempt to fit a noisy spectrum to a sine curve. (c) Fourier spectrum of the data in (b). The maximum near the left axis is due to the low frequency feature of the real spectrum and the zero padding. The zero padding was applied in order to increase the resolution of the Fourier spectrum.

where $k = \frac{1}{\lambda}$, it is clear that the maxima (or minima) appear at every $\frac{1}{2nl}$ increment in k . In Figure 3.7, the maxima indeed appear periodically when the reflectance of a PDMS film is plotted with respect to k . For $m = 1$, we can measure the distance between neighbouring peaks to acquire k and therefore

$$\frac{1}{k} = 2nl. \quad (3.4)$$

Since the curve resembles a sine wave, it is natural to fit a sine curve to it, which in fact works well. However, this approach will not work very well when the spectrum is noisy as shown in Figure 3.7(b) and this is why a more robust method is necessary. Since the noise has a much higher frequency compared to the interference fringes, it is possible to filter the noise by Fourier transformation and thus accurately measure k . We have performed FFT filtering on the data in Figure 3.7(b) using a Hanning window and zero padding, and acquire a Fourier spectrum with a pronounced peak just below 15,000 nm in Figure 3.7(c). This peak should correspond to k , the distance between the fringes in the real spectrum as shown in Figure 3.7(a). To verify that this is correct, we count the number of maxima in Figure 3.7(a) and we see 23 oscillations between 1.0×10^{-3} to 2.6×10^{-3} , hence k is approximately

$$k = (2.6 - 1.0) * 10^{-3} / 23 = 7.0 * 10^{-5} \text{ nm}^{-1}. \quad (3.5)$$

and

$$\frac{1}{k} = 1.4 \times 10^4 [\text{nm}] \quad (3.6)$$

As expected, the period calculated from FFT and from manual fringe counting roughly agrees with each other. The thickness of the film can be calculated from the following equation

$$I_{\text{max}} = \frac{1}{k} = 2nl \quad (3.7)$$

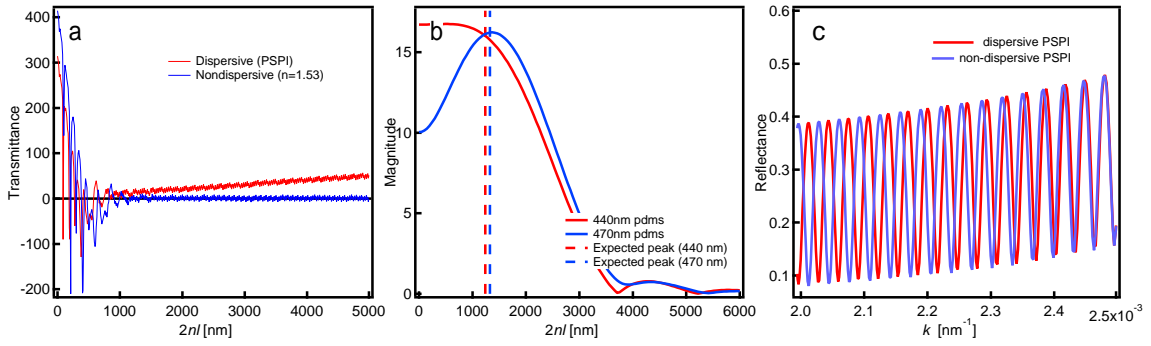


Figure 3.8: (a) Estimation of error of the film thickness for dispersive and non-dispersive ($n = 1.53$) PSPI films on silicon. The error starts to become significant below 1000 nm for both films. A linear increase of error is only seen for dispersive PSPI above 1000nm. (b) Fourier spectra of thin PDMS films. The peak corresponding to the film thickness is overwhelmed by the low frequency feature for the 440 nm film but not for the 470 nm film. (c) Spectra of dispersive and non-dispersive PSPI on silicon substrate plotted with respect to frequency. Although both have the same refractive index at $k = 2.5 \times 10^{-3}$ ($\lambda = 400\text{nm}$), the number of the fringes of the dispersive PSPI is greater by 0.5.

, where I_{max} is the x value of the maximum of the Fourier spectrum. The result is translated to a thickness of $5,170 \pm 10$ nm. This estimation differs by $+93$ nm from the thickness determined by the least square method, which is only 2% difference. Since the FFT method is used for providing seed values, the accuracy is sufficient for the subsequent fitting algorithms to converge to the global minimum.

3.2.3 Limitations of FFT analysis and how to compensate for it

In order to further examine its capabilities and limits, the FFT method was tested on spectra calculated from Equation 2.16. Estimation of film thickness was performed on calculated spectra of PSPI films (0-5000 nm) on silicon substrates. The estimated thicknesses were compared to the thicknesses which was used for generating the spectra. Figure 3.8(a) shows the distribution of error of the estimated thickness. It can be seen that there are noticeable errors in the estimation below 1000 nm. The error is too large below 500 nm for the seed value to be useful. The cause of the large errors may be attributed to the zero padding. The zero padding increases the resolution in the Fourier spectrum, but creates an artificial low frequency feature, which overwhelms the peak of the interference fringe in the Fourier spectrum when the number of fringes is small (Figure 3.8(b)). This can lead to a seed value with too much error which causes the fitting routine to converge to a local minimum. It is noteworthy that the low frequency feature can also be pronounced in the Fourier spectrum of a thick film in some cases, as shown in Figure 3.8(c).

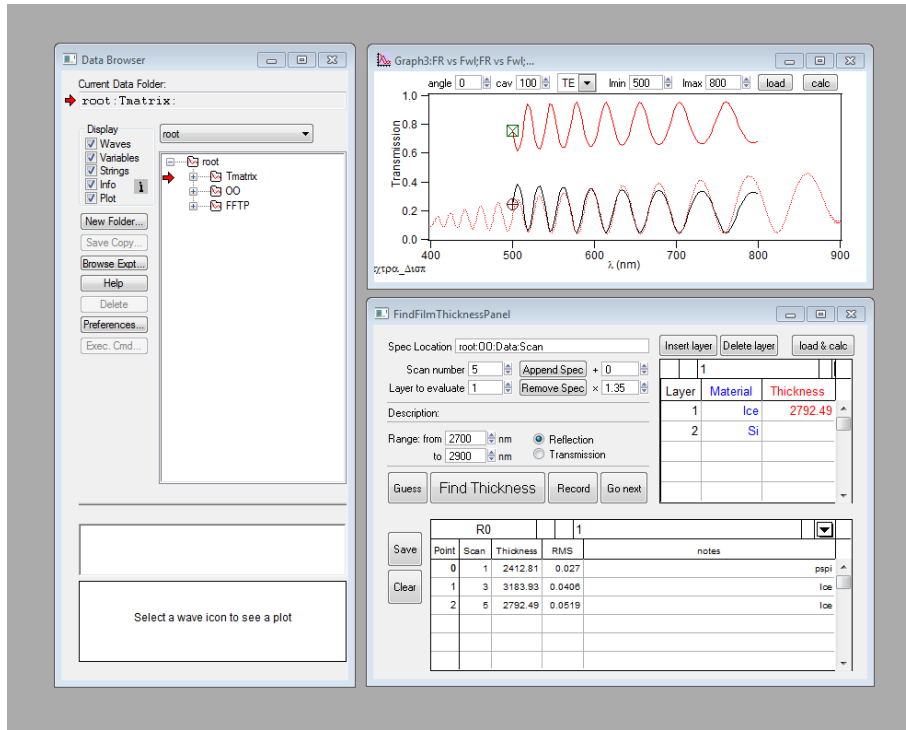


Figure 3.9: Graphical user interface of the FFT method implemented in Igor Pro.

In order to avoid arriving at an incorrect result, a conditional subroutine can be utilised when a seed value is lower than a certain threshold, 1000 nm in the case of Figure 3.8(b), is generated. Since the range where the FFT method becomes incorrect is rather limited, the subroutine can divide the range into multiple sections and run the fitting routine for each of them. The global minimum can be found by comparing the final REM error values of the sections.

There is another important feature in Figure 3.8(a) that has to be pointed out. We see a linear increase in error for the dispersive film but not for the non-dispersive film. The cause of such a difference can be explained as follows. The FFT method must utilise information of the real spectrum from a sufficiently wide wavelength range, so it will include at least about two fringes. However by doing so, the dispersion of the refractive index becomes neglected. As a result, the FFT method will always overestimate the thickness as long as the refractive index of the film has normal dispersion.

This is because the number of fringes of a dispersive film will always be greater compared to that of an idealized non-dispersive film with an averaged refractive index (see Figure 3.8(c)). As a result, the average periodicity of the fringes will be shorter for the dispersive film, and therefore the FFT will overestimate the thickness. The subsequent fitting routine will start to return incorrect results when the magnitude of the error approaches the distance between the local minima of the RMS error. This can be avoided by additionally running the fitting routine for a range lower than what was suggested by the FFT method for thick films.

3.2.4 Implementation

The FFT method was implemented in IGOR Pro version 6 (WaveMetrics) with a graphical user interface as shown in Figure 3.9. Transfer matrix algorithm written by Professor Jeremy J. Baumberg was included for the least-square fit routine. Using the FFT and the least-square methods together ensured accurate and efficient film thickness analysis. The program is capable of handling dispersive and non-dispersive materials, absorbing and non-absorbing materials, monolayer and multilayer films and includes a library of 64 different materials with pre-set refractive indices. A repeat fitting procedure, which is useful for analysing kinetic measurements of drying/swelling films, was also included.

3.3 Assembly of thin films on water

This section introduces the basic set of techniques for manipulating thin films on water surfaces. When devices are assembled from thin films on water surfaces, the following processes are typically involved.

- Transference of a film from its departing substrate to a water surface.
- Immobilisation of the film on the water surface.
- Transference of the film from the water surface to a destination substrate.

In this work, these processes were individually performed by the floating technique, the pinning technique and the catching technique. The folding technique is a method in which all three processes are combined. These techniques are described in the following subsections.

3.3.1 Floating technique

The process for creating periodic structures from thin polymer films, such as folding, rolling and stacking^[15] require an initial floating process. In order to start manipulating thin films on water, a spin-coated film must be first transferred from its initial substrate to a water surface as shown in Figure 3.10. This can be done by using a sacrificial layer, a layer that releases the overlying layer when it dissolves in water. This sacrificial layer can be formed by spin-coating a polyelectrolyte solution prior to the spin-coating of the film that is to be floated. The solvent for the film must be a orthogonal solvent for the sacrificial layer, so the sacrificial layer will not be affected during the spin-coating of the overlying film.

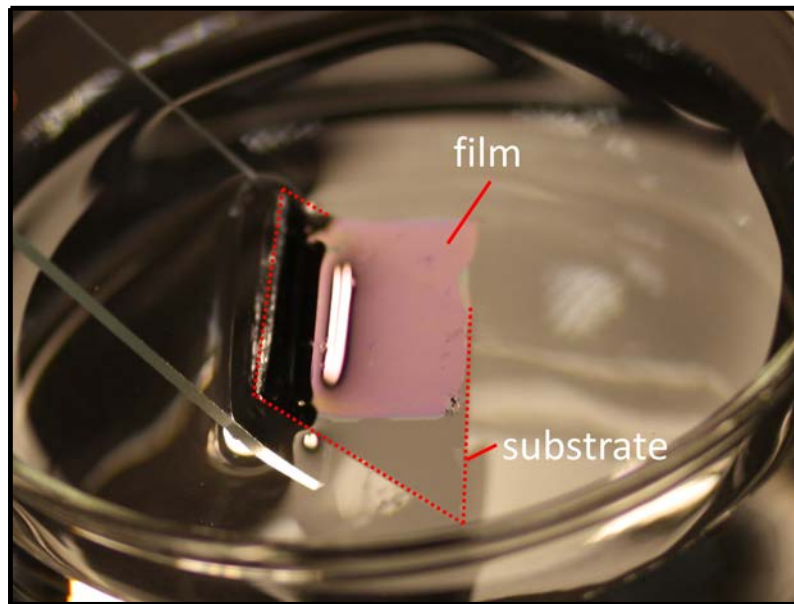


Figure 3.10: Photograph of a film being floated off from a substrate.

3.3.2 Pinning technique

It is often the case that the film has to be transferred from the water surface to a new substrate during or after the assembly of the optical device. As it will be discussed in the next subsection, this can be done by the "Catching technique". During the transference, it is convenient if the film is immobilised on the water surface. This is especially true when the film and the catching substrate require accurate alignment. In order to do so, a cocktail stick with a hydrated tip can be used. By placing the tip on the edge of the film, lateral motions of the film are prevented, making it "pinned" onto the water surface. Rotational motions may also become restricted, even when only one cocktail stick is used.

3.3.3 Catching technique

Transference of the film starts from approaching the film with a substrate. This can be done with the substrate submerged in water or in the air. In the next step the film comes into contact with the substrate at the water surface. If the substrate approaches the film from air, the substrate and film will make secure attachment. Keeping the surface of the substrate with the film downwards, the substrate is submerged into the water and the transference is completed. The substrate can be taken out from the water without loosing the film. If the substrate approaches the film from water, a water layer will be trapped between the film and substrate. Keeping the surface of the substrate with the film upwards, the substrate is taken out from the water and the transference is completed. The film can be re-floated on to water as long as the water layer has not evaporated.

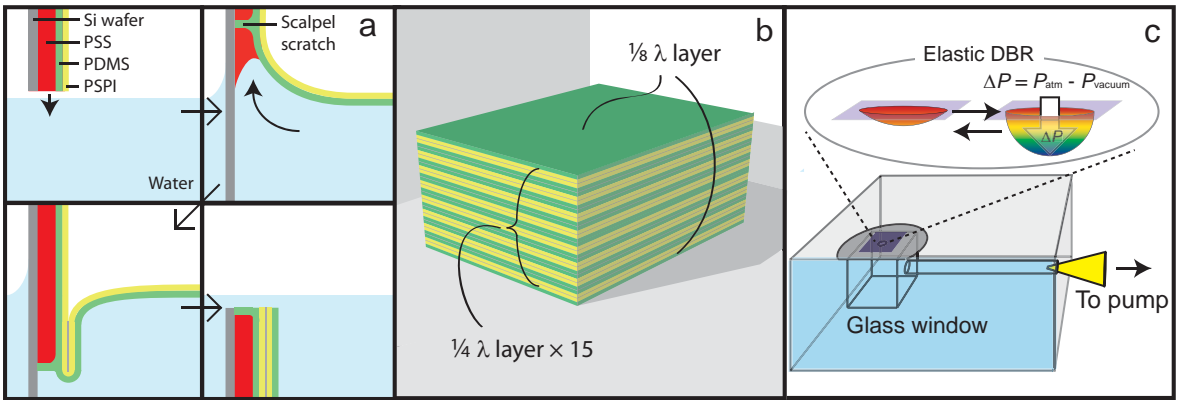


Figure 3.11: (a) Illustration of the Origami technique. The Elastomeric DBR is assembled by immersing the Si wafer coated with a PSS-PDMS-PSPI tri-layer into water. The PDMS-PSPI double layer floats onto the water surface by dissolving an underlying PSS layer until it reaches a scratch in the PSS film, stopping PSS dissolution. Further immersion causes the PDMS-PSPI bilayer to fold back to the upper half of the wafer. The folding steps completes by full submersion of the wafer. (b) Elastomeric DBR after 4 folding steps. (c) Illustration of the home-made sample holder supporting an Elastomeric DBR over a pinhole.

When catching is performed from the water phase, it is recommended that the catching substrate is hydrophilised, typically by oxygen plasma etching, before the catching process. By doing this, the water between the substrate and the film spreads more easily, whereas without the hydrophilisation process the water is likely to become trapped in between the film and substrate by forming droplets or cylinders. The trapped water can be expelled by drying with heat, but will leave creases in order to accommodate the excess amount of film. Such concern is not relevant when the catching is performed from the air phase, but will require precise control of the process in order to not induce defects.

3.3.4 Folding technique

The number of repeats is crucial for making a highly reflective polymer DBR. This is especially true for structures comprising of polymers only, which is because the refractive index contrast between the constituent polymers tend to be small, typically about 0.1. If the process for the fabrication has a mechanism of inducing defects, the repeating process is likely to cause the film to accumulate many defects. In order to have fewer defects, it is favourable to avoid trapping of water, and consequently the U folding technique for PDMS-PSPI DBRs was developed. This method folds the halfway floated film by fully immersing the substrate vertically into the water. The water trapping could be avoided in most experiments. This technique can be used for other combination of elastomers.

In this technique, a thin polysulfonic acid (PSS) layer is first spin-cast onto a silicon

wafer. The PSS layer is marked with a set of orthogonal scratches which extend down to the substrate. A PDMS film is then cast from heptane solution onto the PSS layer followed by cross-linking at 120 °C for one hour. PSPI is subsequently cast from toluene onto the insoluble PDMS rubber to form the next layer. The supported trilayer sample is then immersed into water, dissolving the PSS, which causes the PDMS-PSPI layer to float onto the top water surface. Exposing the PSS layer at the rim of the wafer by scratching the trilayer is often necessary to facilitate dissolution of PSS. PSS dissolution stops as soon as the water reaches one of the scalpel scratches of PSS, where the PDMS is pinned to the substrate surface. Continued immersion of the substrate into the water forces the bilayer to fold back onto the upper-half of the substrate, forming a U-fold of the bilayer (Figure 3.11(a)). The sample is then rotated by 90° and the immersion process is repeated. Repeating the folding steps 5 or 6 times results in multilayers comprising 31 or 63 stacked alternating PDMS and PSPI films of double the thickness compared to the initial spin-cast thickness. The number of the PDMS and PSPI double layers, n , is given by

$$n = 2^m - 1 \quad (3.8)$$

where m is the number of the folding steps. The outmost PDMS single layers are not included in this layer number because they do not contribute to the DBR interference (Figure 3.11(b)).

3.3.5 Deformation of DBRs and PDMS films by pressure difference

In order to study the optical and mechanical property of Elastomeric DBRs under pressure difference, the following method was used. DBRs and PDMS films were floated onto thin stainless steel sheets containing a 300 µm-wide pinhole. The pinhole sheet was fixed air-tight onto a channel in a transparent plexiglass holder (Figure 3.11(c)) and the channel connected to a pump and a pressure gauge, allowing variable evacuation of the volume under the pinhole. A pressure difference established across the air-impermeable multilayer membrane leads to deformation of the films into a concave shape. The deformed films were observed by microscopy and confocal micro-spectroscopy throughout deformation and optical micrographs of the deformed films were taken in top and side-view. The profile of the deformed DBR extracted from side view images provides access to the shape of the deformed film. For transmission spectroscopy and curvature evaluation, the deformed DBR was kept under a constant pressure difference for approximately 10 minutes before the measurement in order to allow the deformed state to stabilise.

3.4 Mechanical tests

The mechanical aspect of the concavely deformed DBR will be examined in Chapter 5. This chapter will introduce the relevant mechanical tests.

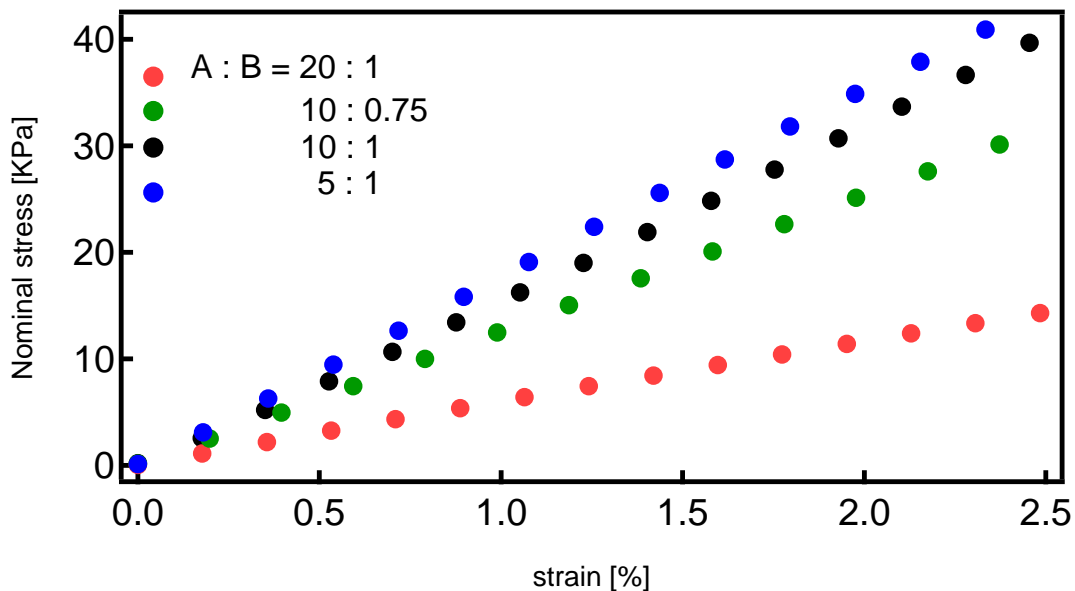


Figure 3.12: Stress-strain plot of tensile tests on PDMS with various cross-linking agent concentration.

3.4.1 Tensile test

Tensile test is one of the simplest methods for determining mechanical properties of materials including elastomers. It is performed by recording the tensile force while the specimen is uniaxially elongated. Young's modulus is a measure of tensile stiffness and can be easily measured by tensile tests. This is because its range of application is limited to small deformations. The equation of Young's modulus is given by

$$E = \frac{\sigma}{\epsilon}. \quad (3.9)$$

The 2D theory of elasticity tells us that shear modulus μ is related to Young's modulus E by the following equation:

$$\mu = \frac{E}{2(1 + \nu)} \quad (3.10)$$

where ν is the Poisson's ratio. Since rubber is incompressible, $\nu = 0.5$ therefore

$$\mu = 3E. \quad (3.11)$$

As shown in Chapter 2, the kinetic theory of rubber is capable of accurately predicting the stress-strain behaviour of vulcanized natural rubber under uniaxial compression (or equivalently equibiaxial stretching) up to 85% of strain.^[28] This means that the equibiaxial stress-strain behaviour of rubber can be predicted to a great extent by

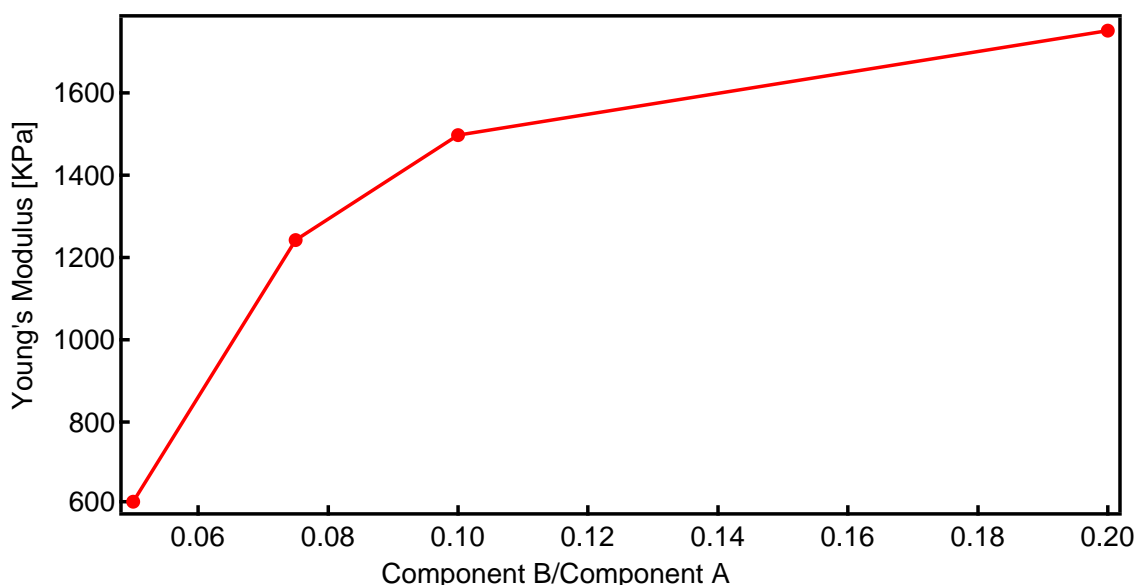


Figure 3.13: Young's modulus of PDMS prepared with various cross-linking agent amount.

only measuring the Young's modulus, which does not require an elaborate set-up. This makes tensile tests a convenient and reliable method to evaluate the stress-strain behaviour of rubbers.

In this work, tensile tests were performed on PDMS specimens and the results were used as a reference to evaluate the accuracy of equibiaxial tests. PDMS (Sylgard 184) sheets were prepared with various cross-linking agent amounts. It was cured at 100 °C for 1 hour and was aged at room temperature for more than a day before the test. Rectangular specimens with dimensions of about 20 mm x 7 mm x 0.75 mm were prepared. The specimens were tested by a custom made tensile tester built by Robyn Pritchard. During the tensile measurements, the specimens were stretched 0.04 mm per step and this was repeated for 20 times with 30 second intervals between each step. The stress was recorded for each step of extension as shown in Figure 3.12. The slope of the plots increased as a function of cross-linking agent concentration as expected. The Young's moduli obtained from linear fit ranged from 0.9 to 1.7 MPa as shown in Figure 3.13. The sample made with a mixing ratio recommended by the manufacture, which is component A : component B = 10:1, had a Young's modulus of $E = 1.5$ MPa. This translates to a shear modulus of $\mu = 500$ KPa from Equation 3.11.

3.4.2 Bulge test

As discussed in Chapter 2, it is necessary to perform different types of stress-strain tests in order to fully elucidate the true form of the strain-energy function.^[28,57] Typically, this is done by a combination of tensile test, equibiaxial test, pure shear test and others.^[28] As a convenient method for performing equibiaxial tests, Treloar used a technique which measures the stress and strain of an inflated circular rubber sheet.^[35]



Figure 3.14: Photograph of an inflated rubber sheet during bulge test. Reprinted with permission from Cambridge Polymer Group.

Treloar found that the strain of the inflated membrane was uniform over a substantial area around the pole of the inflated sheet. By measuring the stretch and radius of curvature at the centre, the equibiaxial stress can be calculated using

$$t = \frac{Pr}{2H} \quad (3.12)$$

where t is the true stress in the direction parallel to the surface of the sheet at the pole, ΔP is the pressure difference, r and H are the radius of curvature and the thickness of the rubber sheet at the pole, respectively. This method is called bulge test. Figure 3.14 shows an example of the test being performed on a rubber material. In this thesis, a similar method was used to determine the shear modulus of PDMS. However, instead of measuring the displacement of two spots near the pole as Treloar did, the thickness of an inflated film was measured by spectral reflection/transmission measurements. The experimental results will be discussed in detail in Chapter 5.

4 Multilayer mirrored bubbles with spatially-chirped and elastically-tuneable optical bandgaps

We demonstrate the multifolding Origami manufacture of elastically-deformable Distributed Bragg Reflector (DBR) membranes that reversibly color-tune across the full visible spectrum without compromising their peak reflectance. Multilayer films composed of alternating transparent rubbers are fixed over a 300 μm wide pinhole and deformed by pressure into a concave shape. Pressure-induced color tuning from the near-IR to the blue arises from both changes in thickness of the constituent layers and from tilting of the curved DBR surfaces. The layer thickness and color distribution upon deformation, the bandgap variation and the repeatability of cyclic color tuning, are mapped through micro-spectroscopy. Such spatially-dependent thinning of the film under elastic deformation produces spatial chirps in the color, and are shown to allow reconstruction of complex 3D strain distributions.

4.1 Introduction

Distributed Bragg reflectors (DBRs), are used as spectrally selective mirrors in many different optical systems, including lasers,^[58–62] light emitting diodes (LEDs)^[63–65] sensing^[14,66–68] and photovoltaics.^[69–71] The realization of a bandgap Elastomeric DBR provides opportunities for the development of novel emission devices such as tunable lasing^[15,72] or LED^[15] systems, and mechanical sensing devices such as pressure or acoustic sensors. In this chapter we demonstrate the manufacture of highly-flexible DBR membranes that exhibit a high reflectance stop-band. The stop-band center can be tuned from 830 nm in the near-IR down to 400 nm in the blue, without compromising the reflection intensity. Simple color-tuning is achieved by pressurising elastic multilayer membranes stretched over a pinhole, deforming them into spherical shapes. Detailed spatially-resolved spectroscopy allows analysis of the color variation across such concavely deformed DBRs, the polarization rotation observed when light reflects off curved regions, and the spatial distribution of the film thickness of the deformed multilayer. Such films can thus be used to analyse the strain distribution in complex deformations of 3D objects.

The contents of this chapter was adapted from *Multilayer mirrored bubbles with spatially-chirped and elastically-tuneable optical bandgaps* – Gen Kamita, Mathias Kolle, Fumin Huang, J.J. Baumberg, and Ullrich Steiner, **Optics Express** 20, 6421-6428 (2012).

4.2 Materials and methods

The Elastomeric DBRs were fabricated and deformed as described in Chapter 3. PDMS and PSPI layers were spin-cast with a thickness of 90 nm and 60 nm respectively. The PDMS was thermally cured at 120 °C for one hour. Given the refractive indices of 1.41 and 1.53 for PDMS and PSPI, respectively, the resulting multilayer stack forms a DBR with a stop-band that is centred in the infrared at ~ 800 nm, with a stop-band reflectance of around 80%.

4.3 Results

4.3.1 Full color DBR tuning

Images of the DBR membrane under deformation show a change in hue from red to blue (Figure 4.1(a) and 4.1(b)). Reflection spectra from the cavity center reveal the dependence of the stop-band peak wavelength on the applied deformation. The stop-band peak smoothly shifts from 800 nm in the near-IR to 400 nm in the blue without a variation in peak intensity (Figure 4.1(c)). This indicates that the ratio of thicknesses of the PDMS and PSPI layers in the DBR remains constant with increasing strain, which is the consequence of equal Poisson ratios of the two elastic layers.

The change in peak reflectance wavelength induced by a variation in light incidence angle and layer thickness upon deformation follows the simple relation

$$m\lambda/2 = d_1\sqrt{n_1^2 - \sin^2\theta} + d_2\sqrt{n_2^2 - \sin^2\theta} \quad (4.1)$$

where d_1 , d_2 , n_1 and n_2 are the thicknesses and the refractive indices of the two multilayer materials, θ is the incident angle of the light and m is a natural number. Analysis of these data reveals a decrease in thickness to one-half of the unstrained value for $\Delta P = 0.33$ bar.

A cyclic tuning test was performed in order to demonstrate the repeatability of stop-band tuning. The Elastomeric DBR peak wavelength was tuned from a starting value of ~ 800 nm to 400 nm and back for 10 cycles (Figure 4.1(d)). Although a reflectance at 400 nm was attained a few seconds after turning on the vacuum pump, returning to ambient pressure did not lead to immediate restoration of the membrane to its original color. The layer was allowed to relax for 5 minutes before starting the next cycle to allow the reflection peak wavelength to recover beyond 700 nm. The reflection intensities remained stable throughout the 10 cycles of tuning (Figure 4.1(e)).

A time resolved spectral measurement was performed after applying a fixed pressure difference of $\Delta P = 0.25$ bar. The peak reflectance shifted from 800 to 600 nm during the initial 100 seconds, followed by a gradual shift to 570 nm over the following hour. This is indicative of a viscoelastic behaviour of the rubber film. While every rubber shows viscoelasticity to a small degree, it is likely that the substantial creep of Figure 4.1(f)

4 Multilayer mirrored bubbles with spatially-chirped and elastically-tuneable optical bandgaps

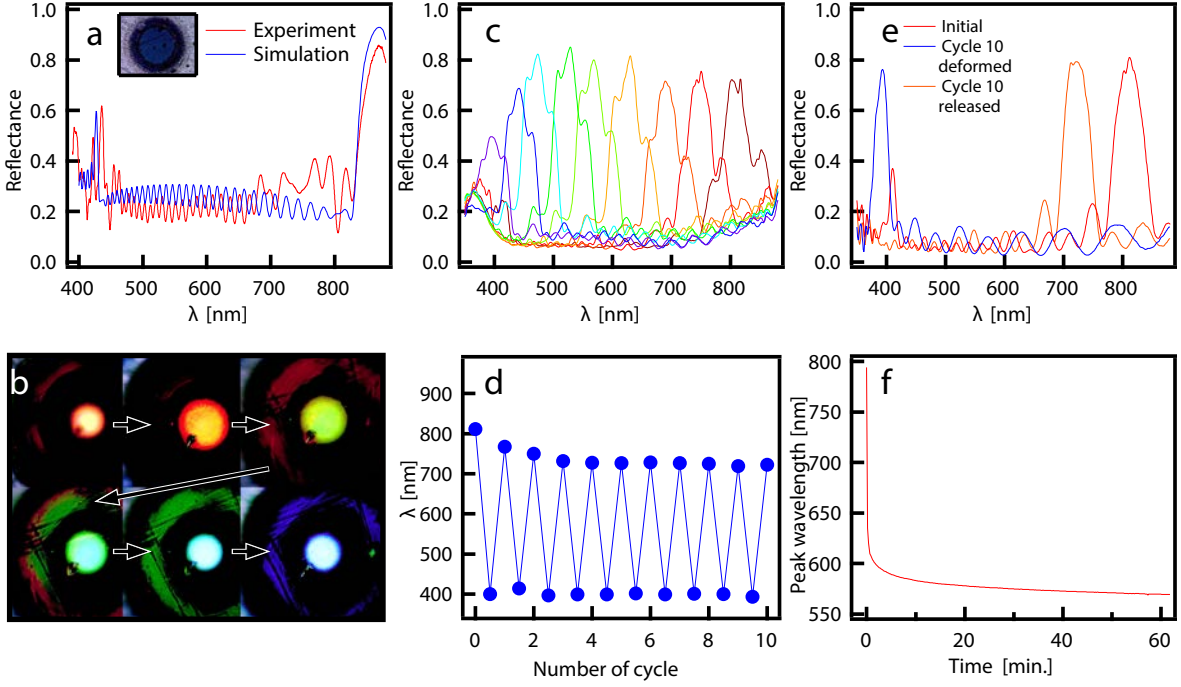


Figure 4.1: (a) Experimental and simulated reflection spectra of a flat Elastomeric DBR still attached to its Si substrate. Simulation parameters were $d_{\text{PDMS}} = 175$ nm, $d_{\text{PSPI}} = 123$ nm, $n_{\text{PDMS}} = 1.41$, and $n_{\text{PSPI}} = 1.53$. The inset shows an Elastomeric DBR on a $300\ \mu\text{m}$ -wide pinhole in its initial flat state. (b) A deformed DBR under increasing pressure showing color shifts from red (top left) to blue (bottom right). (c) Reflection spectra taken during actuation showing shift of stop-band to 400 nm with pressure difference $\Delta P = 0.33$ bar. (d,e) Stop-band tuning of the DBR performed over ten cycles by repeatedly switching ΔP between 0 to 0.32 bar. (f) Peak reflectance position extracted from a time resolved spectral measurement after pressure difference was increased to $\Delta P = 0.25$ bar.

is dominated by the PSPI layer. In contrast to the chemical cross-links of the cured PDMS layer, PSPI forms physical cross-links by PS micro-phase separation which have been shown to enable creep at temperatures above 30°C , where chain pull-out and PS reassembly take place if a sufficiently high force is applied.^[44] This behaviour is likely to affect the recovery speed upon elastic deformation. One possible way to overcome this is to use a polymer with similar optical properties (e.g. pure polyisoprene) that can be chemically cross-linked.

4.3.2 Polarization rotation

Polarization rotation by the pressure-deformed DBR was observed in a microscope with two crossed polarisers (Figure 4.2(a)-4.2(d)). Light incident off-centre onto the concave multilayer surface can undergo more than one reflection within the concavity. Multiple bounces within the concavity induce a polarization rotation caused by a different overall

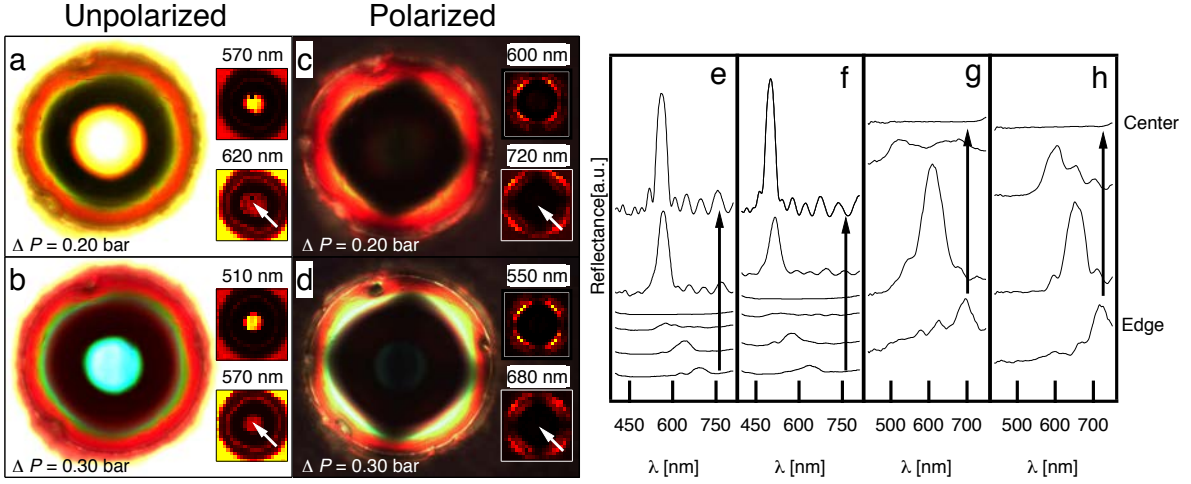


Figure 4.2: (a-d) Observation of rotation by polarization microscopy and micro spectroscopy. Images of the deformed DBR, both (a,b) without and (c,d) with crossed polarisers for (a,c) $\Delta P = 0.20$, (b,d) $\Delta P = 0.30$. Optical reflection from the center is blocked by the crossed polariser while regions near the rim remain bright, which is characteristic for a polarization rotation by double reflection. The insets show images at the indicated wavelengths. (e-h) reflectance along the path indicated by the arrows in (a-d), respectively.

phase shift between TE- and TM-polarized reflections, compared to singly-reflected light. Previous studies have demonstrated that light reflected from hemispherical metal mirrors^[73] and from the photonic structures on butterfly and moth wing scales give rise to a similar effect.^[21, 74, 75] Concave cuticle-air multilayers on the wings scales of *Papilio blumei* cause polarization rotation for blue light after a double bounce from the concavity edges.^[15, 21] Observation of the concavities between crossed polarisers suppresses the yellow center reflection, rendering the butterfly scales macroscopically blue.

Similar to *Papilio blumei*, the deformed DBR shows a difference in color between the center and the edge of the bubble DBR. The double bounce reflection of light from the cavity edges is revealed by the observed differences in reflection color with and without crossed polarisers which is characteristic for *Papilio blumei*-like polarization rotation. Interestingly, light reflected from the center of the deformed rubber DBR is blue-shifted compared to the edge reflection (Figure 4.2(a) and 4.2(b)), in contrast to the wing scale of *Papilio blumei* where the center reflection is red-shifted. This microscopic observation is confirmed by the spectra (Figure 4.2(e)-4.2(h)) which show a clear blue shift of the center stop-band peak. This observation is seemingly in contradiction with Eq. (4.1) which predicts a red shift of the center reflection compared to the concavity edges. The reason for this inverted colour performance for the Elastomeric DBR is a systematic variation in PDMS and PSPI layer thickness in the center compared to the edges upon deformation, resulting in a net red-shift. This shift to shorter wavelengths from the edges to the center therefore indicates a higher local strain of the polymer layers at the concavity center, as discussed below.

4 Multilayer mirrored bubbles with spatially-chirped and elastically-tuneable optical bandgaps

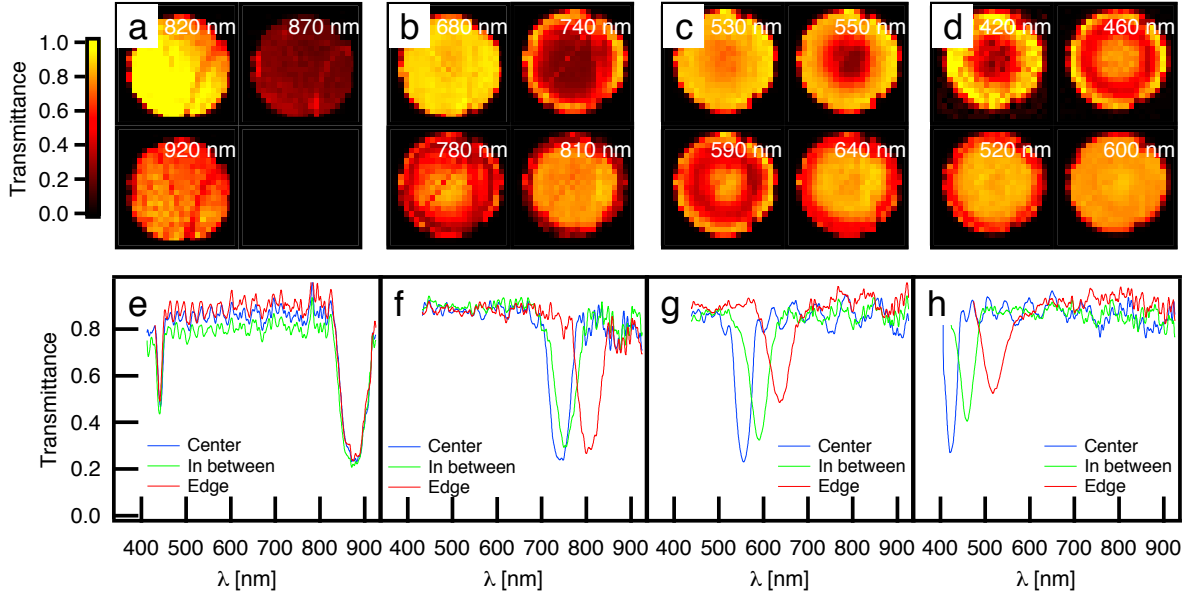


Figure 4.3: (a-d) Spatial distribution of transmitted intensity at different wavelengths. The maps were taken (a) in the initial non-deformed state, (b) the residual concavity state after deformation and relaxation, (c) $\Delta P = 0.17$ bar and (d) $\Delta P = 0.27$ bar. (e-h) Spectra extracted from (a-d), respectively. The small red shift in (f) is due to the permanent deformation of the multilayer after actuation.

4.3.3 Spatial chirp

In order to confirm a radially inhomogeneous strain distribution within the concavely shaped DBR, the sample was mapped spectroscopically in transmission with a resolution of $15\ \mu\text{m}$ (Figure 4.3). The Elastomeric DBR in its non-deformed state has a homogeneous stop-band distribution (Figure 4.3(a) and 4.3(e)). At $\Delta P = 0$ after several actuation steps, it acquires slight permanent concave form caused by the repeated tuning cycles. The spectrum taken at the center of the pinhole shows a stop-band around $745\ \text{nm}$, compared to a stop-band peak of $\sim 800\ \text{nm}$ at the concavity edge (Figure 4.3(b) and 4.3(f)). This is a clear indication of localized film thinning at the center. The red shift becomes more pronounced when the Elastomeric DBR is further deformed, with a stop-band difference of up to $100\ \text{nm}$ (Figure 4.3(d) and 4.3(h)).

Further evidence of the localized thinning was acquired by analysing the film radial thickness distribution. Micrographs taken through the side window of the custom-made sample holder revealed the change in the curvature of the deformed multilayer for increasing pressure differences (Figure 4.4(a)-4.4(c)). The variation of incident angles across the spherically deformed DBR membrane were calculated from the shape of the deformed DBR. The thickness distribution along the deformed DBR as a function of horizontal distance from the pinhole center was then calculated using Eq. (1) with λ acquired from the spectral maps and θ from angle distribution maps (Figure 4.4(d)). The initial Elastomeric DBR before actuation has a homogeneous thickness distribu-

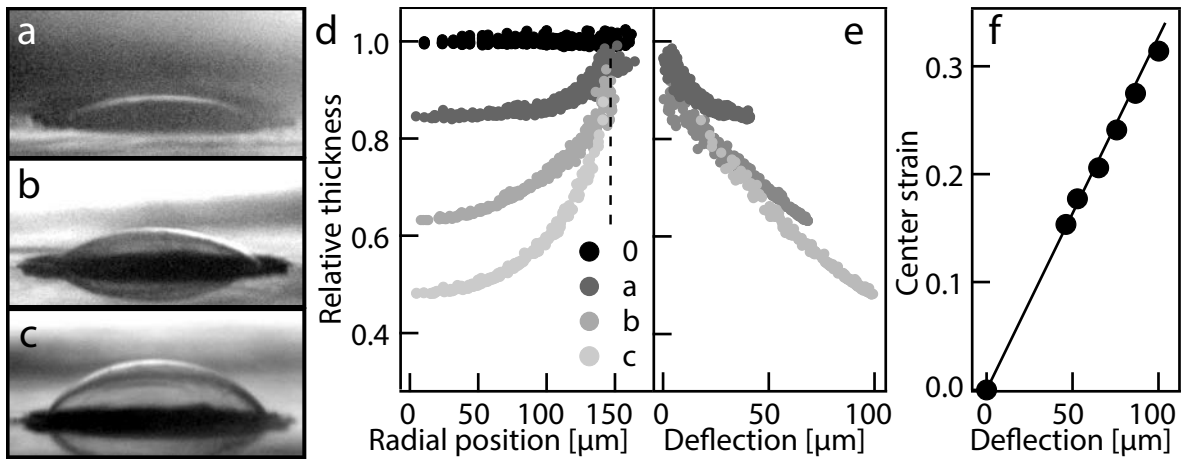


Figure 4.4: (a-c) Images of a deformed DBR taken in the permanently deformed state, and with applied pressures of 0, 0.17 and 0.27 bar. (d) PDMS and PSPI layer thickness variation of the Elastomeric DBR across the pinhole extracted from the spectral maps, together with (e) its dependence on the local deflection. (f) Extracted strain at the mirror centre *vs* the deflection produced by different pressures.

tion. The hemispherical geometry of the actuated film concentrates the strain at the center, thereby enhancing the observed spectral shift.

The spherical nature of the shape is further revealed when plotting the relative thickness against the local deflection at different radial positions (Figure 4.4(e)). Although the actual shape of such an elastic bubble is a highly complicated non-analytic function, as the pressure increases the bubble shape becomes more spherical and the thickness directly tracks the deflection.^[76] This can also be seen in the linearity of the maximum strain found at the centre of the membrane with the local deflection at that point (Figure 4.4(f)). These features point to the robustly predictable nature of suitable designed elastomeric optical components. Extraction of such data on deformed membranes has been previously difficult, and the use optically-functional membranes opens up new capabilities for understanding 3D elastic deformations in detail.

Such non-uniform strain distributions suggest a new route to spectroscopic components. Combining such non-uniformly strained dielectric multilayers yielding chirped thickness variations together with diode arrays and CCDs, allows reconfigurable hyperspectral imaging. While the demonstration shown here was of a regularly-spaced DBR, the complete range of multilayer filter functions are possible, including high-pass, low-pass, bandpass, notch and dichroic elements. Applications include Raman edge filters for maximising laser rejection by elastic tuning, as well as graded photonic bandgap systems useful for adjustable negative dispersions for pulse compression. Improvements require control of the creep identified in such systems, through better control of the cross-linking.

4.4 Conclusion

We have demonstrated the repeatable full color tuning of elastically deformable DBRs across the entire optical spectrum without compromising the peak reflectance. Light reflected from the edge of the deformed DBRs showed polarization rotation, while the center reflection was blue shifted compared to the edge. These effects are caused by multiple reflection of incident light at the edge and localized film thinning at the center of the deformed DBRs.

Future developments will allow acquisition of thickness and curvature data from the Elastomeric DBR to allow extension of this work to the study of inflation of micro-balloons.^[77] Such structures also provide prospects for the development of color displays, resonant cavities for tunable lasing, tunable LEDs, and bio-inspired filters/reflectors for security applications. Using chemically cross-linked polyisoprene instead of PSPI should enhance actuation sensitivity and decrease the response time to pressure changes, enabling the development of accurate low-cost optical acoustic sensors.

5 Effect of geometry and mechanical properties on the optical effects of axisymmetrically inflated Elastomeric DBRs

In the previous chapter, the optical effects of axisymmetrically deformed Elastomeric DBRs by bulging, and their inhomogeneous strain distribution was investigated. The main findings were that the concavely deformed DBRs had a similar optical effect as the wing scale of *Papilio Blumei*, but with reversed hue sequence. The blue shifted colour in the pole (referred to as centre in Chapter 4) arose from the localisation of strain, sufficiently thinning the film to override the angular effect. It was also found that the thickness at the centre of the DBR decreases by creep, when it was under a pressure difference for a long period of time, but it was not discussed whether the creep was occurring locally or globally. In this work, we will further investigate the effect of localised thinning of the DBR balloon by studying its stress-strain behaviour. The Mooney-Rivlin model and a numerical method was used and it is demonstrated that the localisation of strain at the pole of the concavely deformed DBR is not only due to the geometrical configuration of the inflation process, but also because of the effect of creep taking place at the pole, which makes it softer compared to the edge of the balloon.

5.1 Introduction

Photonic crystals with mesoscopic features can exhibit unique optical properties due to the interplay of their photonic bandgap and the effect of geometrical optics. The colour selective and angle dependent reflection of an ordinary 1D photonic crystal is eye-catching in its own right, yet its colouration can become even more striking by additional effects introduced by reflection and refraction, which are the fundamental effects of ray-optics. Novel effects such as polarisation sensitive reflection, colour-mixing, diffuse reflection and unusual angle dependency of the colour can be incorporated into the coloration by geometrical optics occurring on mesoscopic length scales.^[22, 23, 74, 75, 78-80] Such photonic structures with additional optical effects can be found in insects and animals, for example butterflies, beetles, shield bugs and birds,^[22, 23, 74, 75, 78-80] and they have been providing inspiration for creating photonic devices with novel optical functionalities.^[20, 22, 23]

Recently, it was demonstrated that elastically tunable Distributed Bragg Reflectors, which are 1D photonic crystals purely consisting of rubbers, can simultaneously display multiple colours when inflated into a hemispherical balloon.^[81] The deformed DBRs exhibited polarisation sensitivity due to the double reflection of light,^[20, 81] which is essentially a retro reflection mechanism occurring on a hemispherical reflector. The mechanism of the coloration was found to be similar to some butterflies,^[22, 23, 74, 75] but

had a different hue sequence. In the case of the deformed DBR, the distribution of the thickness was substantially graded along its radius, which caused the Bragg stack to be much thicker at the edge (or rim), causing its colour to be red-shifted in comparison to the pole. This is the opposite than in butterflies,^[23,74] where the edge of the concavity shaped multilayer is blue-shifted compared to its centre due to the angular dependency of the reflected colour. Since the DBR had a uniform colour at its initial flat state, the inverted hue arrangement caused by the gradient thickness is clearly dependent on the inflation process. In addition, it was also reported that the stop-band at the pole gradually blue shifted under constant pressure difference, which suggests that the stress-strain behaviour of the DBR under axisymmetric inflation may have an impact on its optical appearance.

In this work, we demonstrate that the inverted hue sequence is created by an interplay of the axisymmetric inflation process and the viscoelasticity of the rubbers the DBR is made from. Instead of studying the time evolution of the stress and strain of the DBR, which is the most straight forward approach for solving viscoelastic problems, we assume that the DBR is completely elastic on the timescale of the measurement. Although the DBRs does show viscoelastic behaviour on a longer timescale, this assumption enables us to focus only on the spacial distribution of the stress and strain, which significantly simplifies the problem.

As we will see in the following sections, the strain of a flat rubber film varies strongly in the radial direction when it is axisymmetrically inflated into a hemispherical balloon. This is partially due to the effect of the geometric conformation of the inflation process, but also because of the heterogeneous distribution of the effective stiffness, which is caused by creep. The Mooney-Rivlin theory will be used to reproduce the heterogeneous stiffness caused by creep by taking advantage of the geometric constraint on the deformation. Using a chemically cross-linked PDMS films which has negligible creep as a reference, the variation of the elastic properties of the DBR is characterised. In addition, the effect of C_2/C_1 on the deflection, the effective stiffness at the pole and the edge and the optical appearance will be discussed. As an overall trend, a clear contrast between the PDMS and the DBR will be presented. It will be shown that the viscoelastic property of the DBR has a strong influence on the optical appearance when it is deformed.

5.2 Materials and methods

5.2.1 Experimental methods

Following the protocol of described in Chapter 3, a 7 μm thick PDMS film was floated onto a stainless steel sheet with a 300 μm wide pinhole at the centre. The film was inflated by pressure difference until it reached a steady state, and reflection spectra of the film were taken at the pole. At the same time, photographs of the bulged films were taken from which the radius of curvatures of the films were extracted. The film

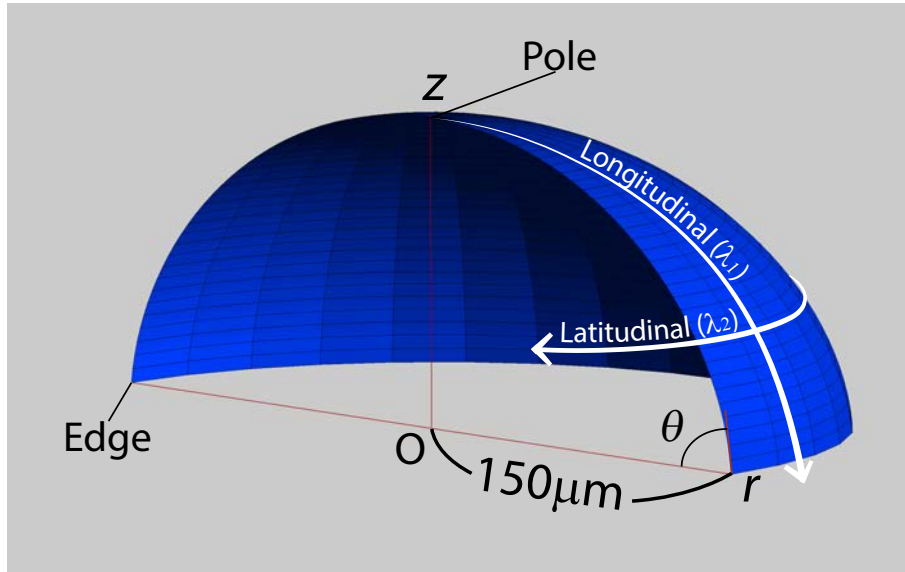


Figure 5.1: A three dimensional model of an axisymmetrically inflated balloon.

thickness of the pole, or in other words the centre of the inflated film, was calculated from the reflection spectra taken by micro-spectroscopy. The deflection of the pole was measured from the photographs and by varying the focus of the microscope, which allowed to measure the distance between the stainless sheet and the film. The data of the DBR was taken from Chapter 4. The DBR was repeatedly inflated before the measurement and permanently deformation.

5.2.2 Equibiaxial test (bulge test)

The hoop stress of the inflated PDMS film at the pole was evaluated. As mentioned earlier, it is possible to calculate the equibiaxial stress of an axisymmetric balloon at the pole from the curvature as long as the film thickness is sufficiently thin (less than 1/10 of the radius). Historically, this method was first adopted by Treloar for studying the stress-strain behaviour of vulcanized polyisoprene.^[28] It is still being used^[57] because of its simplicity and reliability. The experiment performed in this work is equivalent to what Treloar has done in 1944. Assuming equibiaxial extension, the true stress of the PDMS film at the pole was calculated by

$$t_1 = \frac{\Delta P \rho}{2H\lambda_3}, \quad (5.1)$$

where t_1 and is the true stress in the longitudinal direction (see Figure 5.1), ΔP is the pressure difference, ρ is the radius of curvature, H is the thickness of the film before deformation and λ_3 is the stretch ratio of the film in the direction of the thickness. ρ was obtained from the photographs of the deformed films and H and λ_3 were obtained from transmission spectra measurements. t_1 was plotted as a function of λ_1 , the stretch ratio

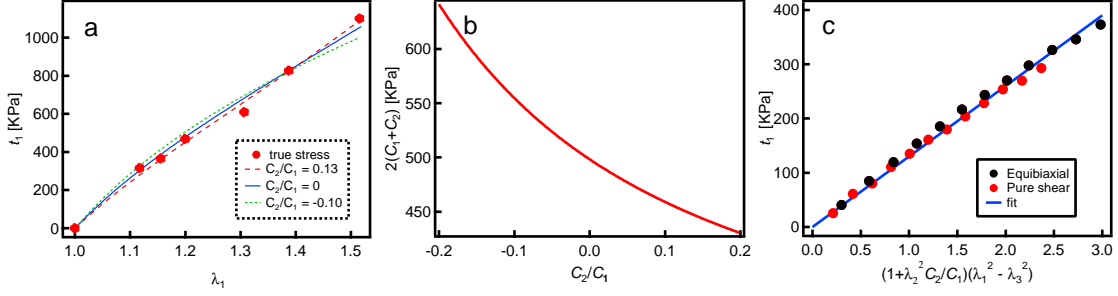


Figure 5.2: (a) Stress-strain plot of a PDMS film tested by bulging. (b) Shear modulus $2(C_1 + C_2)$ of Mooney-Rivlin materials determined by curve fitting on the data of (a), plotted as a function of C_2/C_1 . (c) Stress plotted on basis of Equation 5.6.

in the longitudinal direction, and was fitted to the Neo-Hookean model of equibiaxial extension (see Figure 5.2(a)),

$$t_1 = \mu(\lambda_1^2 - \lambda_1^{-4}), \quad (5.2)$$

and a shear modulus of $\mu = 500$ KPa was obtained. According to

$$E = 3\mu, \quad (5.3)$$

the obtained shear modulus translates to $E = 1.5$ MPa, which is in good agreement with the tensile test in Chapter 3. The Mooney-Rivlin model of equibiaxial extension

$$t_1 = 2(\lambda_1^2 - \lambda_1^{-4})(C_1 + C_2\lambda_1^2) \quad (5.4)$$

was also fitted to the data. C_1 and C_2 are the Mooney-Rivlin constants, which determine the stress-strain behaviour of the material. C_1 and C_2 were varied in curve fit, in order to best approximate the equibiaxial data. At a first glance, the purpose of using the Mooney-Rivlin equation may not be obvious, because the results of the fits with varying C_2/C_1 are very similar to each other as shown in Figure 5.2(a). This is because only equibiaxial extension was considered, and other types of deformation were not taken into account. It is necessary to consider the problem in a more general context in order to understand the significance of the Mooney-Rivlin equation.

As it was shown by Treloar's so-called dead-loading experiment,^[28,29,82] the stress-strain behaviour of rubber tends to deviate from the classical Neo-Hookean theory under general biaxial deformation. In other words, when a rubber sheet is simultaneously stretched in two principle directions with various ratios of strains, it is no longer practical to represent its stiffness with a single constant μ , as it was done in the classical Neo-Hookean theory. This is because the difference between the theory and experiment becomes too large to ignore. Specifically, the stress-strain curve of

equibiaxial extension starts to exceed the theoretical prediction, while it tends to fall below the prediction under shear. This deviation in stress-strain behaviour can be compensated in Mooney-Rivlin model by adjusting the two constants, C_1 and C_2 . The ratio between the two constants, C_2/C_1 , can be regarded as a measure of the deviation of the stress-strain behaviour from the Neo-Hookean model. The shear modulus of the Mooney-Rivlin material, which is defined as

$$\mu = 2(C_1 + C_2). \quad (5.5)$$

It monotonically decreases with increasing C_2/C_1 when C_1 and C_2 are determined by the fitting as shown in Figure 5.2(b). Therefore, the Mooney-Rivlin material with a high C_2/C_1 will behave softer under pure shear. At this point, it is not clear which value of C_2/C_1 best reproduces the stress-strain behaviour of PDMS the best. Therefore, the best-fit C_2/C_1 was calculated from other experimental results. The data in Figure 5.2(c) was taken from the work of Urayama *et al.*,^[83] in which they performed a series of general biaxial tests, similar to Treloar's dead-loading experiment, on end-linked PDMS networks. The true stress of equibiaxial extension $\lambda_1 = \lambda_2$ and pure shearing $\lambda_2 = 1$, were taken and was plotted as a function of

$$(1 + \lambda_2^2 C_2/C_1)(\lambda_1^2 - \lambda_3^2). \quad (5.6)$$

In this representation, the data should fall on a straight line passing through the origin for the appropriate ratio of C_2/C_1 .^[28] The best fit yielded $C_2/C_1 = 9.28 \times 10^{-2}$. This is in a fair agreement with the curve fit to our equibiaxial test, performed without any constrain on C_2/C_1 , which gave $C_2/C_1 = 0.13$. The value of C_2/C_1 found in the literature for vulcanized polyisoprene under biaxial extension ranges from 0.05 to 0.1.^[28,82] Therefore, within the range of investigated stretch ratios, the stress-strain behaviour of PDMS under biaxial extension is similar to that of vulcanized polyisoprene.

5.3 Theory of Inflation of axisymmetric balloons

5.3.1 Zhu's method

A numerical method developed by Zhu *et al.* was used to model the axisymmetric inflation of PDMS and DBRs. The method was originally developed for simulating the oscillation of dielectric elastomers under pressure differences and oscillatory voltage.^[76]

Following their approach, the material particles were labelled by their distances R from the origin O at its undeformed state.^[76] At its inflated state, the position of each particles were specified by $r(R)$ and $z(R)$, which are the radial and axial distance from the origin, respectively. λ_1 is the stretch ratio in the longitudinal direction of the hemispherical balloon and λ_2 is the stretch ratio in the latitudinal direction, as shown in Figure 5.1. Assuming $H \gg \rho$, λ_1 and λ_2 were defined in terms of r and z and their

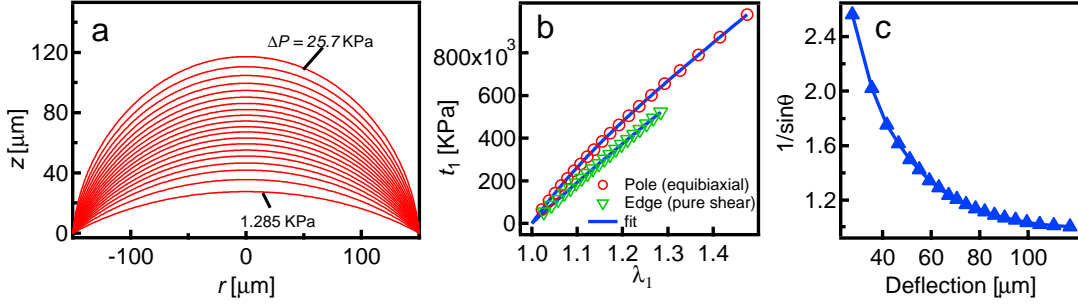


Figure 5.3: (a) Calculation of profiles of a Neo-Hookean film with $\mu = 500$ KPa. ΔP was varied from 1.285 to 25.7 KPa with 1.285 KPa of increment per step. (b) Stress-strain plot re-calculated from the results of (a). (c) $1/\sin\theta$ plotted as a function of deflection.

differential elements

$$\lambda_1 = \sqrt{\left(\frac{\partial r}{\partial R}\right)^2 + \left(\frac{\partial z}{\partial R}\right)^2} \quad (5.7)$$

$$\lambda_2 = \frac{r}{R}. \quad (5.8)$$

From the definition of stretch ratio,

$$dl = \lambda_1 dR \quad (5.9)$$

where l is the distance between R and $R + dR$. It can be easily deduced that

$$r(R + dR, t) - r(R, t) = \cos\theta(R)dl \quad (5.10)$$

$$z(R + dR, t) - z(R, t) = \sin\theta(R)dl, \quad (5.11)$$

$$(5.12)$$

where $\theta(R)$ is the angle of the film with respect to the horizontal plane. Assuming that the film is a Neo-Hookean material, the nominal stress in the longitudinal and latitudinal directions are

$$s_1 = \mu(\lambda_1 - \lambda_1^{-3}\lambda_2^{-2}) \quad (5.13)$$

$$s_2 = \mu(\lambda_2 - \lambda_2^{-3}\lambda_1^{-2}). \quad (5.14)$$

$$(5.15)$$

In addition, the following equations were derived by calculus of variation^[76] and by balancing of force.^[84]

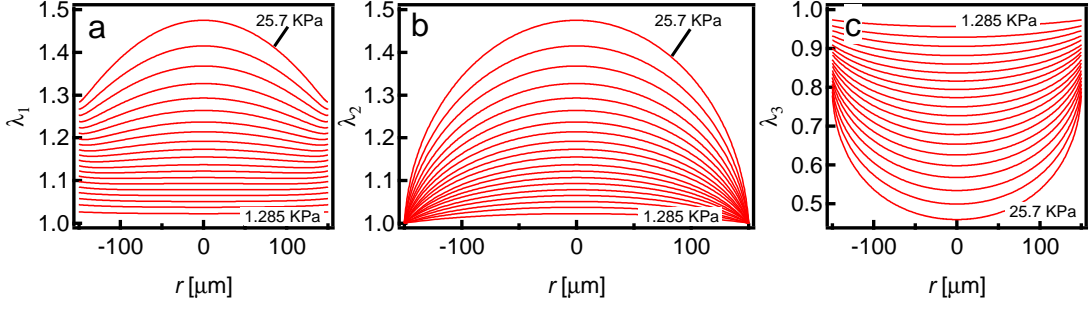


Figure 5.4: (a-c) Distribution of (a) λ_1 , (b) λ_2 and (c) λ_3 of an inflating film.

$$-\frac{\partial}{R\partial R}(Rs_1 \sin \theta) + \lambda_1 \lambda_2 \frac{\Delta P}{H} \cos \theta = 0 \quad (5.16)$$

$$\frac{\partial}{R\partial R}(Rs_1 \cos \theta) - \frac{s_2}{R} + \lambda_1 \lambda_2 \frac{\Delta P}{H} \sin \theta = 0 \quad (5.17)$$

$$(5.18)$$

were t is the time. Equation 5.16 and 5.17 are satisfied when the film is inflated to its equilibrium state. The profile of the axisymmetrically inflated film is obtained by solving these differential equations.

5.3.2 Numerical modelling of axisymmetric inflation of Neo-Hookean membranes

The equations were solved using Mathematica. Figure 5.3 shows the profiles of axisymmetrically inflated films with varying pressure. The degree of inflation increases as a function of pressure difference as expected. In addition to the pole, the deformation at the edge can be analysed analytically. At this position, λ_2 is always $\lambda_2 = 1$ regardless of the degree of inflation, as can be seen in Figure 5.4(b). This indicates that the deformation taking place at the edge is pure shear. The true stress of pure shear of Neo-Hookean materials is defined as

$$t_1 = \mu(\lambda_1^2 - \lambda_1^{-2}). \quad (5.19)$$

By considering the balancing of force, the pure shear stress in the longitudinal direction at the edge can be written as

$$t_1 = \frac{\Delta P r}{2 \sin \theta (A) H \lambda_3} \quad (5.20)$$

where A is the radius of the supporting stainless steel sheet, H is the film thickness before inflation and λ_3 is the stretch ratio in the direction of the thickness of the film.

Using Equation 5.1 and 5.20, stress-strain plots of the pole and the edge can be extracted from the calculated results ($\Delta P = 1.258$ to 25.7 KPa) and the shear modulus was fitted using Equation 5.1 and 5.19, in order to evaluate the accuracy of the numerical method. The difference between the value of the shear modulus initially used for calculating the profile and that obtained by fitting the results of the calculation was less than $\pm 0.25\%$. Importantly, the true stress at the pole reaches $t_1 = 980$ KPa at $\Delta P = 25.7$ KPa, whereas the maximal stress at the edge is only $t_1 = 520$ KPa at the same pressure difference. The plot indicates that the stress at the pole is always greater than the stress at the edge.

Figure 5.3(c) shows $1/\sin\theta$ as a function of deflection. As the degree of inflation will be measured by deflection in the following sections, it is important to estimate the error in the stress at the edge which is introduced by the measurements of the deflection. The pure shear stress at the edge is proportional to $1/\sin\theta$ as can be seen from Equation 5.19.

Figure 5.4(a)-(c) show the distribution of the principle stretches in the two principal directions. λ_1 and λ_2 are parallel to the two in-plane directions of the film. In specific, λ_1 is parallel to the longitudinal direction and λ_2 is parallel to the latitudinal direction (see Figure 5.1). λ_1 and λ_2 are written as a function of R , r , z and their derivatives are defined in Equations 5.7 and 5.8 respectively. Both λ_1 and λ_2 have graded distributions along the r direction. As a result, λ_3 , or equivalently the thickness of the film, also varies where λ_3 is always smaller at the pole compared to the other parts of the film. From this fact and also from the difference in t_1 at the pole and edge, shown in 5.3b, it is clear that the pole always accumulates the greatest stress compared to other parts of the film.

5.4 Numerical analysis of axisymmetrically inflated films

5.4.1 Modelling of PDMS balloons

In order to establish a basis for comparison, the inflated states of a PDMS film is analysed. Figure 5.5 shows the profile of the PDMS film inflated with various pressure differences. The profile of the inflated PDMS film was calculated from Zhu's equations and was compared with the experimental results. The variables of the calculation were set to the same value of the experiment, namely the film thickness to ($7\ \mu\text{m}$), the pressure difference to ($\Delta P = 13.8$ to 30.9 KPa), the diameter of the pinhole to ($300\ \mu\text{m}$), and the shear modulus to (500 KPa). The calculated profiles were superposed on to the photos for comparison, and the experiment and calculation were found to be in good agreement, but errors in the bulge height became increasingly pronounced with increasing pressure difference. As can be seen in the Figure 5.5, the gap between the broken line, which indicates the bottom surface of the supporting stainless steel sheet, and the end of the superposed curve increases by increasing pressure difference. The

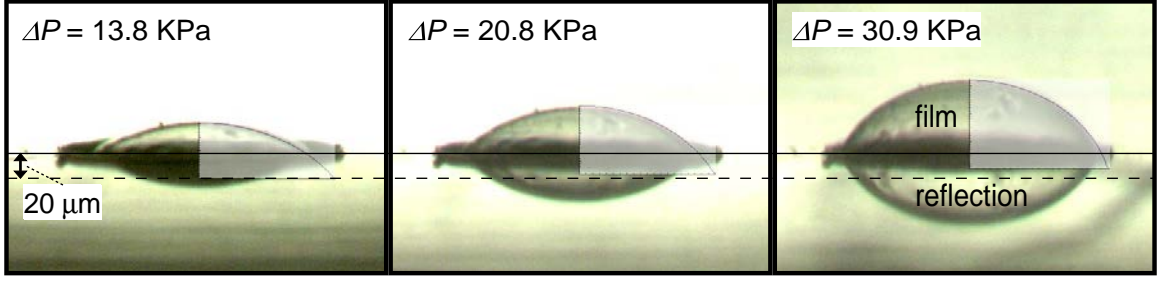


Figure 5.5: Photographs of inflated PDMS film with $\Delta P = 13.8$ - 30.9 KPa. The solid line and broken line indicate the vertical positions of the top and bottom surface of the $20 \mu\text{m}$ thick stainless steel sheet. The PDMS film, which is attached to the bottom of the stainless steel sheet, is bulging upwards and its reflection is seen on the top surface of the stainless steel sheet.

Mooney-Rivlin model was used in a second calculation by replacing Equation 5.13 and 5.14 with

$$S_1 = 2(\lambda_1 - \lambda_1^{-3}\lambda_2^{-2})(C_1 + C_2\lambda_2^2) \quad (5.21)$$

$$S_1 = 2(\lambda_2 - \lambda_2^{-3}\lambda_1^{-2})(C_1 + C_2\lambda_1^2). \quad (5.22)$$

S_1 is the nominal stress of a Mooney-Rivlin material under general biaxial extension. To the best of our knowledge, this is the first time the Mooney-Rivlin equation was used in Zhu's equation. C_1 and C_2 were determined by a method which ensures the maximal consistency between the numerical calculation and the experimental results of the equibiaxial test. As before, the coefficients were determined by a curve fit to the equibiaxial test fixing C_2/C_1 at a specific value. This way it is possible to conserve the stress-strain behaviour of the Mooney-Rivlin material under equibiaxial extension as shown in Figure 5.2(a), while altering the behaviour of other types of deformation. In particular, the stress-strain behaviour under pure shear is significantly shifted as shown in Figure 5.2(b).

In this method Mooney-Rivlin materials with a positive C_2/C_1 behave softer under pure shear compared to a Neo-Hookean material with a shear modulus of $\mu = 500$ KPa, which is equivalent to a Mooney-Rivlin material with $C_1 = 250$ KPa and $C_2 = 0$ KPa. Considering such change in the shear modulus of an axisymmetrically inflated film, setting C_2/C_1 to a positive value causes the edge to behave softer in comparison to a negative value of C_2/C_1 , because of the geometrical constraint on λ_2 . This gives rise to the prediction that a Mooney-Rivlin film with positive C_2/C_1 will inflate to a greater degree compared to a Neo-Hookean film under the same conditions.

Using four sets of Mooney-Rivlin coefficients obtained from curve fitting, the bulge height and λ_3 of the pole were calculated and compared with the experimental results as shown in Figure 5.6. The bulge height calculated with $C_2/C_1 = 0$ best matched the experimental results for $\Delta P = 13.8$ KPa. $C_2/C_1 = 0.10$ and $C_2/C_1 = 0.20$ yielded

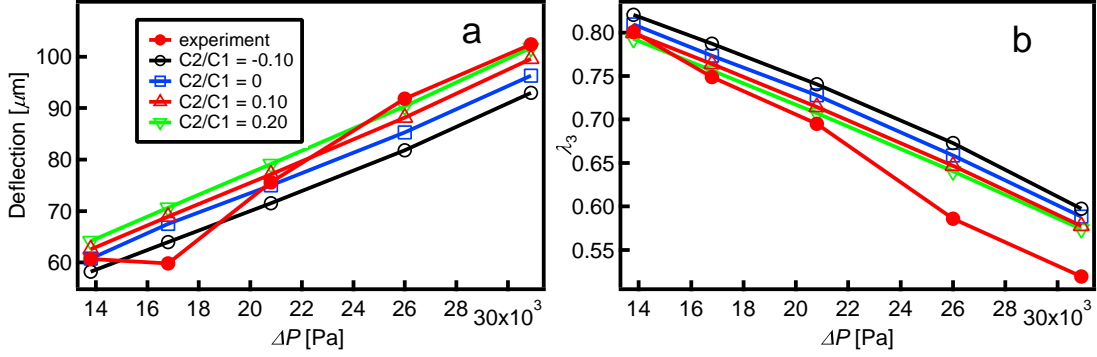


Figure 5.6: (a,b) Comparison between experiment and calculation on (a), bulge height and (b), λ_3 at the centre to the experimental results.

better matches for higher pressure differences. This is in agreement with Urayama's result finding PDMS has a positive C_2/C_1 . On the other hand, the numerical solutions for λ_3 with $C_2/C_1 = 0.10$ and $C_2/C_1 = 0.20$ matched the experiment well at low pressure, but all predictions overestimated λ_3 for pressure differences above $\Delta P = 26$ KPa, with the least agreement for $C_2/C_1 = -0.10$, both in the bulge height and the λ_3 at the pole.

The reason for the poor prediction of λ_3 , may arise the fact that C_1 and C_2 are not constant but complex functions of strain invariants.^[85] The correct form of Mooney-Rivlin equation for biaxial extension is derived by partial differential equations of the strain-energy function W , a function which takes I_1 and I_2 as independent variables.

The assumption that $\frac{\partial W}{\partial I_1}$ and $\frac{\partial W}{\partial I_2}$ are the constants C_1 and C_2 gives rise to a first order approximation of the Mooney-Rivlin equation, which reproduces the stress-strain behaviour of elastomers better than the Neo-Hookean model. It is however known that this approach is of limited accuracy.^[28] As shown in Figure 5.4, the distribution of the stretch ratios during inflation is highly inhomogeneous, varying between equibiaxial extension and pure shear from the pole to the edge. It is likely that the error in λ_3 is caused by approximating $\frac{\partial W}{\partial I_1}$ and $\frac{\partial W}{\partial I_2}$ with the constants C_1 and C_2 . To improve the prediction, it is necessary to use second or higher order Mooney-Rivlin equations or other hyperelastic models such as Ogden model.^[57] For our characterisation of the optical properties of the deformed DBRs, the accuracy of the first order Mooney-Rivlin equation is sufficient.

Modelling the PDMS film as a Mooney-Rivlin material with a positive C_2/C_1 has improved the numerical calculation of the inflation of the PDMS film, as can be seen from the RMS of each sets of solutions in Figure 5.7(a). These results are consistent with the results of the biaxial tests of Figure 5.2(a) and (c), which also gave positive values of C_2/C_1 as best fit results.

So far our discussion was based on the stress and strain at the pole and the edge in the longitudinal direction only. It is also important to understand the stress-strain behaviour between these two points and also in the latitudinal direction. Therefore, we

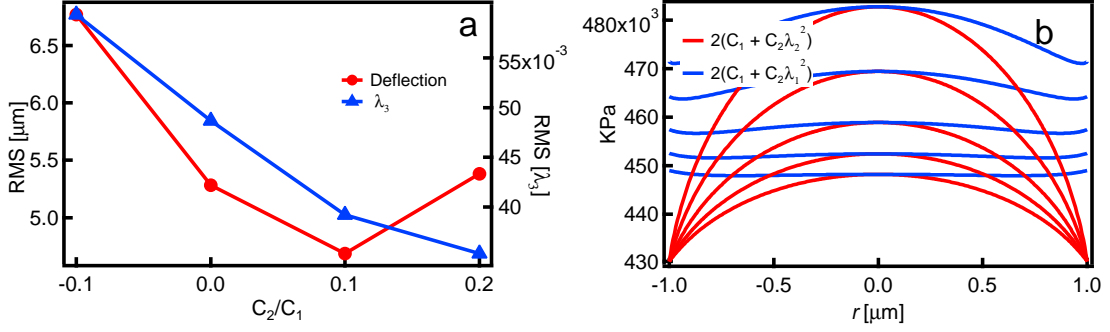


Figure 5.7: (a) Distribution of $2(C_1 + C_2\lambda_2^2)$ and $2(C_1 + C_2\lambda_1^2)$. (b) RMS of bulge height and λ_3 calculated from that data in Figure 5.6.

utilise $2(C_1 + C_2\lambda_2^2)$ as a measure of the stiffness for the longitudinal direction, which changes with varying λ_2 , and $2(C_1 + C_2\lambda_1^2)$ for the latitudinal direction. $2(C_1 + C_2\lambda_2^2)$ and $2(C_1 + C_2\lambda_1^2)$ are plotted with respect to their r position as shown in Figure 5.7(b). Overall, both $2(C_1 + C_2\lambda_2^2)$ and $2(C_1 + C_2\lambda_1^2)$ tend to gradually decrease with increasing r . $2(C_1 + C_2\lambda_2^2)$ is slightly greater at the edge when the degree of inflation is small, but this trend is no longer seen when the film is inflated with a pressure difference of more than 26 KPa. The transition of the stress-strain behaviour from the equibiaxial stretching at the pole to the pure shear at the edge is smooth and mostly monotonic. The distributions of $2(C_1 + C_2\lambda_2^2)$, $2(C_1 + C_2\lambda_1^2)$, λ_1 and λ_2 are qualitatively similar.

5.4.2 Modelling of DBR balloons

An inflated DBR was examined similarly to the previous section. Because the Mooney-Rivlin theory is an elastic model and not a viscoelastic model, this method is not able to fully characterise the viscoelastic properties of the DBR. It can however provide a snapshot of the strain distribution which can serve as an evidence for heterogeneous creep processes. As with the PDMS balloons, the stiffness of the DBR at the pole was determined with Equation 5.1, obtaining $\mu = 500$ KPa for the measurement performed at $\Delta P = 17$ KPa, and $\mu = 510$ KPa for $\Delta P = 27$ KPa. For simplicity we assume that the pole of the DBR can be effectively described as a Neo-Hookean material with a shear modulus of $\mu = 500$ KPa at both pressures, and the Mooney-Rivlin constants C_1 and C_2 for various C_2/C_1 were calculated using

$$C_2 = (250 - C_1)/\lambda_{2pole}^2. \quad (5.23)$$

This conserves the stress-strain behaviour at the pole while altering strain distribution at other locations of the bubble. $2(C_1 + C_2\lambda_2^2) = 500$ is satisfied only at the pole, except when $C_2/C_1 = 0$ where the material becomes Neo-Hookean. Figure 5.8 shows the solution of λ_3 , together with the experimental results of λ_3 of the inflated DBR taken from Chapter 4. In contrast to the results of the PDMS film, the solutions which

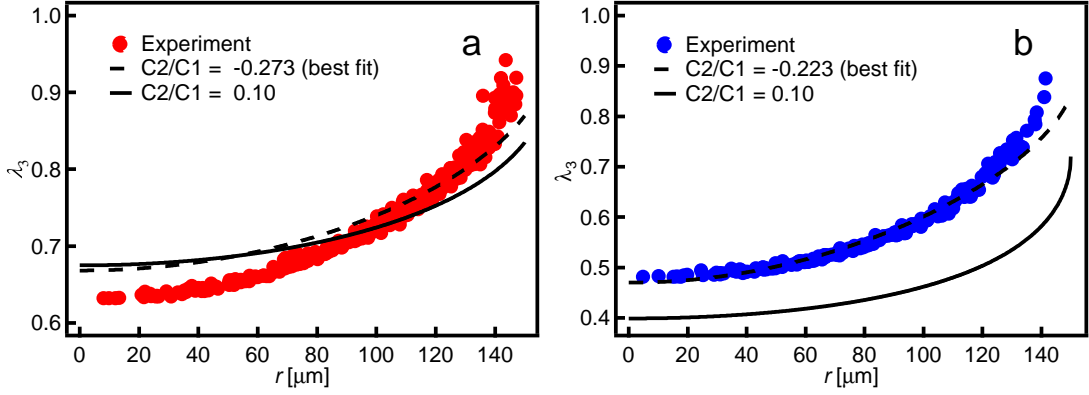


Figure 5.8: (a,b) Experimental results and calculations of λ_3 at (a) $\Delta P = 17$ KPa and (b) $\Delta P = 27$ KPa.

reproduced the experiments well exhibited negative C_2/C_1 values. The best fit curves was obtained for $C_2/C_1 = -0.273$ and $C_2/C_1 = -0.223$ for $\Delta P = 17$ KPa and $\Delta P = 27$ Pa, respectively, as shown in Figure 5.8. In addition, the calculated bulge height which best matched the experiment was obtained for $C_2/C_1 = -0.365$ ($\Delta P = 17$ KPa) and -0.262 ($\Delta P = 27$ KPa) as shown in Figure 5.9. Furthermore, λ_3 at the edge matched the experiment for $C_2/C_1 = -0.52$ (17 KPa) and $C_2/C_1 = -0.40$ (27 KPa), yielding shear moduli of $2(C_1 + C_2) = 991$ KPa ($\Delta P = 17$ KPa) and $2(C_1 + C_2) = 1120$ KPa ($\Delta P = 27$ KPa). Since all results give negative C_2/C_1 values, it is highly likely that the effective stiffness of the deformed DBR is much greater at the edge compared to the pole. The effective stiffness at the edge is estimated to be 1.23 to 1.98 times greater for $\Delta P = 17$ KPa and 1.48 to 2.23 times greater for $\Delta P = 27$ KPa. The differences in bulge height between the experiment and the calculation vary depending on C_2/C_1 , which introduces errors in the effective stiffness at the edge.

5.4.3 Effect of creep on the optical properties of the inflated DBR

In order to evaluate the effect of the thickness distribution and the inflated shape on the optical property of the DBR, the stop-band distribution of the inflated DBR with various C_2/C_1 values was calculated using

$$\tilde{\lambda}(r)/2 = d_1(r)\sqrt{n_1^2 - \sin^2 \theta(r)} + d_2(r)\sqrt{n_2^2 - \sin^2 \theta(r)}, \quad (5.24)$$

where $\tilde{\lambda}$ is the wavelength of the transmittance peak (in optics, λ is used for wavelength as a convention, however $\tilde{\lambda}$ is used in this chapter to avoid ambiguity between wavelength and stretch ratios), $d_1(r)$ and $d_2(r)$, $n_1(r)$ and $n_2(r)$ are the thicknesses and refractive indices of PDMS and PSPI respectively and $\theta(r)$ is the angle of incidence, or equivalently the angle of the DBR surface with respect to its flat geometry.

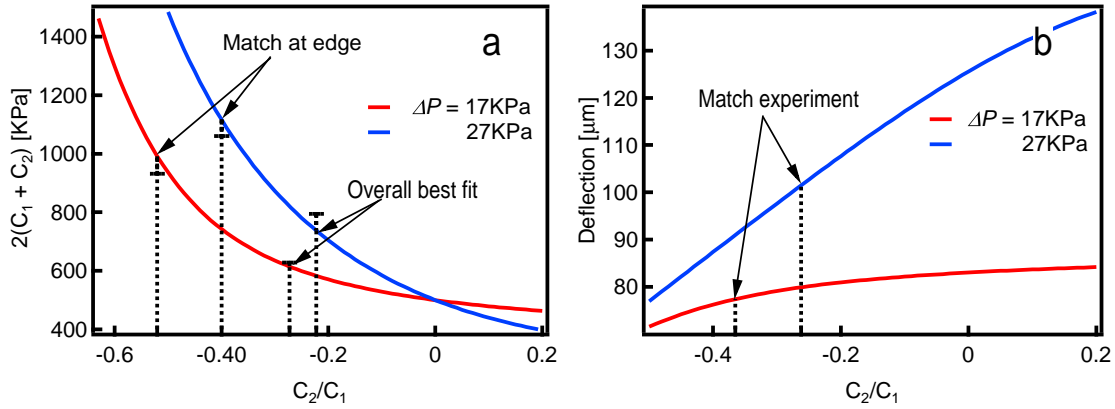


Figure 5.9: (a) Distribution of $2(C_1 + C_2)$ of the calculation on the basis of Equation 5.23. The arrows indicate the C_2/C_1 which gives the best fitting curves and curves which match the experiment at the edge. Error bars indicate the possible over/under estimation due to the difference in the bulge height between the experiment and calculation (see Figure 5.3(c)). (b) Calculated bulge height as a function of C_2/C_1 . The steep gradient of the curve for $\Delta P = 27$ KPa can introduce significant over/under estimation of λ_3 .

Figure 5.10(a) and (b) show the distribution of the transmittance peak of the inflated DBR at $\Delta P = 17$ KPa and $\Delta P = 27$ KPa respectively. The curve calculated with $C_2/C_1 = -0.273$ ($\Delta P = 17$ KPa) reproduces the red shift of the edge qualitatively while $C_2/C_1 = -0.223$ ($\Delta P = 27$ KPa) reproduces the entire distribution of λ_3 accurately. In contrast, the curves calculated using $C_2/C_1 = 0.1$ fails to reproduce the experimental results in both cases. For $\Delta P = 17$ KPa, the edge shows blue shift with respect to the pole instead of red shift. For $\Delta P = 27$ KPa, λ_3 is significantly underestimated for the entire range of r , arising from a greater inflation of the calculated film compared to the experiment, as can be seen from the difference in bulge height shown in Figure 5.9. This overall underestimation of λ_3 prevents meaningful comparisons. Therefore, the degree of red shift at the pole was evaluated as a function of bulge height as shown in Figure 5.10(c). The curve with $C_2/C_1 = -0.25$ shows a greater red shift at the edge for all bulge heights compared to the curve with $C_2/C_1 = 0.10$. The curve with $C_2/C_1 = 0.10$ only shows a red shift of 23.1 nm at the edge for the measured bulge height of 101 μm , while the curve with $C_2/C_1 = -0.223$ shows a red shift of 124 nm at this bulge height, which is in good agreement with the experiment.

To summarise, the curves with $C_2/C_1 = -0.223$ and -0.273 qualitatively reproduced the experimental results of the stop-band distribution for $\Delta P = 17$ KPa and quantitatively for $\Delta P = 27$ KPa, while the curves with $C_2/C_1 = 0.10$ did not provide a good fit. Therefore, we conclude that creep contributes significantly to the gradient in film thickness and therefore to the hue of the deformed DBR. The edge appears to be red-shifted relative to the pole, which is partially due to the geometric factor which concentrates the strain at the pole, but may also be caused by the material property of

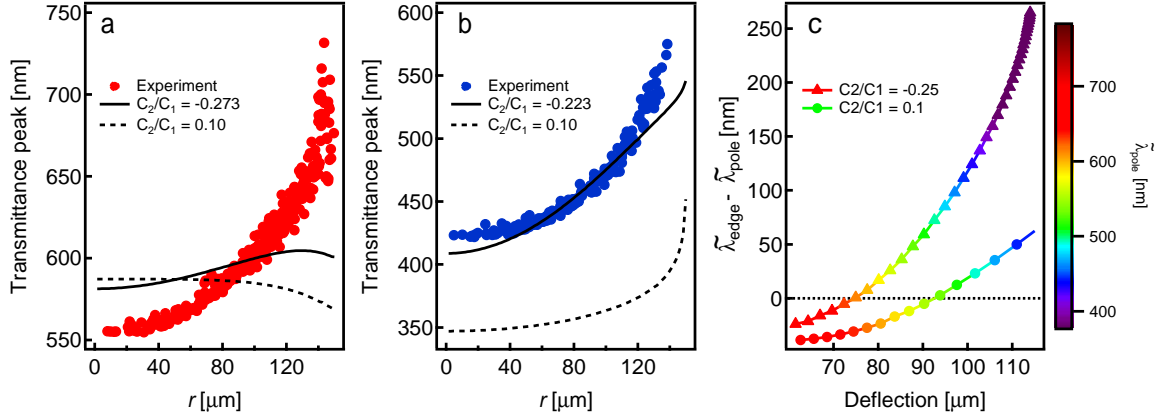


Figure 5.10: (a,b) Experimental results and calculations of transmittance peak distribution at (a), $\Delta P = 17$ KPa and (b), $\Delta P = 27$ KPa. (a) The edge of the curves calculated from $C_2/C_1 = -0.273$ is red shifted compared to the pole, whereas $C_2/C_1 = 0.10$ gives a blue shifted edge. (b) The curve calculated from $C_2/C_1 = -0.223$ shows a red shift of 137 nm of the edge with respect to the pole. The solution from $C_2/C_1 = 0.10$ greatly underestimates the transmittance, which is due to the large error in the bulge height. (c) Degree of red shift of the edge ($\tilde{\lambda}_{\text{edge}} - \tilde{\lambda}_{\text{pole}}$) shown as a function of bulge height. The colour scale indicates the transmittance peak of the pole, $\tilde{\lambda}_{\text{pole}}$.

the DBR film, which allows creep to occur predominantly at the pole. The combination of the two effects creates a sufficient thickness difference between the pole and the edge, so that the angular dispersion of light interference is overridden by the thickness effect on the stop-band, thereby creating an inverted hue sequence, which cannot be realized by a DBR with a curved geometry without a gradient in the film thickness.

5.5 Conclusion

The stress-strain variation of elastomeric DBRs was studied in relation to their optical properties. Numerical analysis and experimental results showed that the inverted hue variation is due to the interplay of the axisymmetric inflation process and the viscoelastic creep of the DBR. Due to the fact that equibiaxial extension and pure shear occurs at specific points, namely at the pole and at the edge of the inflated film, the difference in the stress-strain behaviour between non-creeping PDMS films and creeping DBR films was able to be captured by modelling them as Mooney-Rivlin materials. The film thickness and bulge height of the PDMS and DBR films, and the inverted hue variation of the DBR were reproduced well by a positive C_2/C_1 value for the PDMS film and negative C_2/C_1 for the DBR.

The Mooney-Rivlin theory is an elastic theory that does not allow to model viscoelasticity and the analysis therefore does not provide detailed information about the vis-

coelastic properties of the DBR. It does however provide evidence of creep and its effect on the optical appearance of the DBR. The difference in the signs of the best fit C_2/C_1 values indicates a differing nature of the stress-strain variation of the PDMS and the DBR films for axisymmetric inflation.

For PDMS, positive values of C_2/C_1 were found. This implies that PDMS is stiffer under equibiaxial extension compared to pure shear, which is also true for chemically cross-linked natural rubber.^[28, 82]

In contrast, C_2/C_1 values less than -0.2 reproduced the distribution of λ_3 of the inflated DBR and the bulge height, implying a stiffer edge of the DBR compared to the pole. This behaviour of the Elastomeric DBR is attributed to the viscoelastic nature of PSPI. According to the classical theory of rubber elasticity, the Helmholtz free energy of rubber is entirely stored as the entropy of the polymer chains between cross-linking sites. Therefore the type of cross-link, chemical or physical, should have little influence on the stress-strain behaviour of rubber, as long as the cross-links of the PSPI are permanent.

The negative values of C_2/C_1 indicate that this assumption is incorrect. As seen from the heterogeneous distribution of λ_3 , the stress is greater at the pole and therefore it is reasonable to assume that creep is predominantly occurring at the pole compared to the edge, leading to a lower effective stiffness at the pole in comparison to the edge. Investigations on dynamic properties such as the frequency response of the DBR are necessary to better characterise the viscoelastic behaviour of the DBR.

6 Equilibrium state of thin elastomer films on water

In this chapter, the mechanics of thin elastomer films floating on water is studied in order to provide a view for establishing the foundation of high quality Elastomeric DBR fabrication. A model which describes the free energy minimum was developed and was used to analyse PDMS films with thicknesses ranging from 100 to 1400 nm. It was found that the strain of PDMS films become significant by decreasing film thickness. Based on the results, an outline of an improved folding method for eliminating wrinkles and creases of Elastomeric DBRs is introduced.

6.1 Wrinkling/creasing phenomena in soft materials

Soft materials are highly susceptible to wrinkling and creasing. Many objects around us that become wrinkled by themselves, and we know by experience that maintaining them free from wrinkles require effort. For example, washed bed sheets must be hung in such a way that they are flat during drying, otherwise they will require ironing. One possible explanation for why bed sheets are easily wrinkled, is because the crystalline cellulose fibres in cotton are rigid at room temperature.^[86] Once they memorise the wrinkled form of the bed sheet, they do not have the mobility to change their conformation to allow a wrinkled bed sheet to become flat. Increasing the mobility of the cellulose molecules by heating or hydration allows the conformation of the fibres to reorganise.

Another good example is facial skin. As we age, it is increasingly necessary to apply moisturisers regularly to maintain youthful looking skin. Older skin is stiffer and less elastic compared to younger skin. The reason why cosmetic products can make our skin less wrinkled is because Stratum Corneum, the upper most layer of human skin, becomes softer when it is hydrated.^[87] Technically, wrinkles and creases can be defined as surface instability induced by buckling. They can be found not only on flat surfaces such as sheets or films, but also on many different structures including layered structures supported by foundations, cylinders, tubes, capsules and others.^[88] Regardless of the various forms, the underlying principle of the wrinkling instability is always the same; it is the heterogeneous distribution of strain and stiffness which governs the amplitude and periodicity of wrinkles.^[89,90]

The fact that wrinkling or creasing can occur in Elastomeric DBRs was occasionally a subject of discussion, but a systematic investigation to improve understanding of stress and strain in elastomer films during fabrication has not yet been carried out. Because wrinkling/creasing instabilities are universally found in soft materials, it is reasonable to assume that they also appear in Elastomeric DBRs. Without proper treatment, Elastomeric DBRs fabricated by the folding method always suffer from wrinkling/creasing

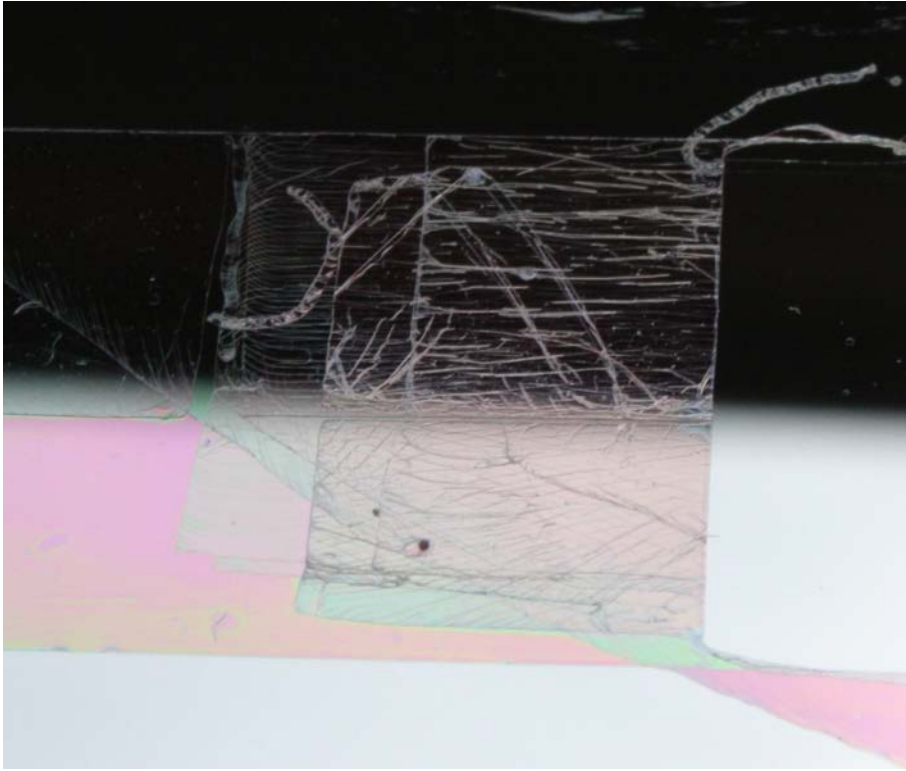


Figure 6.1: Photograph of a Elastomeric DBR. Creases are running horizontally on the DBR.

as shown in Figure 6.1. In fact, even when the folding process is carried out very carefully, it is extremely difficult to make an Elastomeric DBR with a defect-free spot larger than $100\ \mu\text{m} \times 100\ \mu\text{m}$. It is clear that DBRs that are full of defects are not suitable as mirrors for most applications. Even if an application requires only a small DBR, the high defect density will lower the yield and increase the manufacturing cost of the product. Nevertheless, the examples of bed sheets and facial skin imply that wrinkling/creasing instabilities can be controlled by understanding their cause and treating them accordingly. Therefore, revealing the stress-strain distribution in elastomer films during the fabrication process can be the key for improving the quality of the Elastomeric DBR. The purpose of this chapter is to demonstrate a method to quantify the strain of thin elastomer films, and to identify their origin. It will be shown that the stress and strain that can cause wrinkling/creasing of Elastomeric DBRs fabricated by the folding method, are induced by thermal expansion and surface tension during curing and floating of the elastomer film. A new strategy for controlling the stress and strain will be described at the end of the chapter.

6.2 Free energy of thin elastomer films on water

6.2.1 Helmholtz free energy of Neo-Hookean solid under uniaxial deformation

In order to understand the stress and strain of elastomer films during the floating process, we first start by considering the equilibrium state of thin rubber films floating on water. The surface free energy and the Helmholtz free energy of a soft elastomer film become comparable to each other when the film is sufficiently thin. More specifically, the surface tension of water at room temperature^[91] is

$$\gamma = 7.3 \times 10^{-2} \approx 10^{-1} \text{N/m}.$$

This is on the same order of the normalized Helmholtz free energy of an elastomer film with a shear modulus of 10^6 Pa and a thickness of 10^{-7} m. Since

$$\mu \times d = 10^6 \times 10^{-7} = 10^{-1} \text{ N/m},$$

therefore

$$\gamma \approx \mu \times d.$$

This means that the stress and strain of an optical device assembled from elastomer films by the floating technique with a thickness on the order of the optical wavelength, will be under the strong influence of surface tension as well as the elastic force of the elastomer. As we saw in Chapter 2, the Helmholtz free energy density of a Neo-Hookean solid can be written as

$$W = \frac{1}{2}\mu(\lambda_1^2 + \lambda_2^2 + \lambda_3^2 - 3), \quad (6.1)$$

where μ is the shear modulus and λ_1 , λ_2 and λ_3 are the principle stretch ratios. When a rubber film undergoes equibiaxial compression in the direction parallel to λ_1 , the stretch ratios can be written as

$$\lambda_2 = \lambda_3 = \frac{1}{\lambda_1^{0.5}}. \quad (6.2)$$

Therefore Equation 6.1 becomes

$$W = \frac{1}{2}\mu\left(\lambda_1^2 + \frac{2}{\lambda_1} - 3\right). \quad (6.3)$$

6.2.2 Surface free energy of soft thin films on water

Next, we consider the surface energy of the film floating on water. Let us first consider the difference in the surface energy between the two situations. The first situation is when there is water in a container with no film floating on it. The surface free energy of the air-water interface with an area of A is

$$G = A\gamma_{aw}, \quad (6.4)$$

where γ_{aw} is the surface energy of water. The second situation is when an elastomer film is floating on the water surface. The film has two interfaces, namely the air-film interface and the film-water interface. With an area of the film A_1 , the net surface free energy is

$$\begin{aligned} G &= A_1(\gamma_{af} + \gamma_{fw}) + (A - A_1)\gamma_{aw} \\ &= A_1(\gamma_{af} + \gamma_{fw} - \gamma_{aw}) + A\gamma_{aw} \end{aligned} \quad (6.5)$$

where γ_{af} and γ_{fw} are the interfacial tensions at the air-film interface and the film-water interface. We simplify Equation 6.5 by using

$$\gamma_{net} = \gamma_{af} + \gamma_{fw} - \gamma_{aw}. \quad (6.6)$$

Therefore

$$G = A_1\gamma_{net} + A\gamma_{aw}. \quad (6.7)$$

We assume that the film is stretched or compressed by surface tension. Using Equation 6.2, A_1 can be written in terms of the non-strained area A_0 as

$$A_1 = A_0\lambda_2\lambda_3 = \frac{A_0}{\lambda_1}. \quad (6.8)$$

Hence Equation 6.7 becomes

$$G = \frac{A_0\gamma_{net}}{\lambda_1} + A\gamma_{aw}. \quad (6.9)$$

From Equation 6.3 and Equation 6.9, we now consider the net free energy of a floating film with a volume of V , non-strained area A_0 and thickness d ,

$$E = VW + G. \quad (6.10)$$

Note that W is the free energy *density* function, hence the volume of the film must be multiplied with it in order to obtain the Helmholtz free energy. The first order partial derivative of E becomes zero at equilibrium,

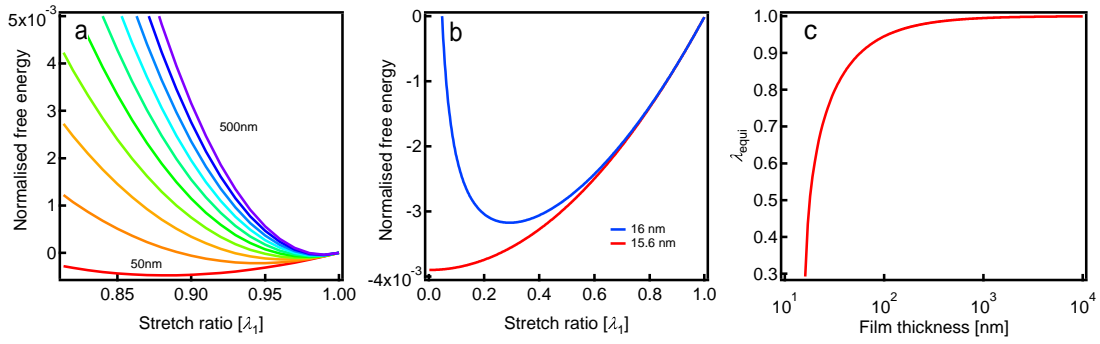


Figure 6.2: (a,b) Distribution of the normalised free energy $((G - A_0\gamma_{\text{net}})/A - \gamma_{\text{aw}})$ of Neo-Hookean films with $\mu = 500$ KPa. (a) The increment of the film thickness is 50 nm from the curve at the bottom (red curve, 50 nm) to the top (purple curve, 500 nm). (b) Free energy distribution of very thin films. (c) Distribution of equilibrium stretch ratio.

$$\begin{aligned} \frac{\partial E}{\partial \lambda_1} &= V \frac{\partial W}{\partial \lambda_1} + \frac{\partial G}{\partial \lambda_1} = \\ &V\mu\left(\lambda_1 - \frac{1}{\lambda_1^2}\right) - \frac{\gamma_{\text{net}}}{A_0\lambda_1^2} = 0 \\ d\mu\left(\lambda_1 - \frac{1}{\lambda_1^2}\right) - \frac{\gamma_{\text{net}}}{\lambda_1^2} &= 0. \end{aligned} \tag{6.11}$$

$$\tag{6.12}$$

Satisfying Equation 6.12 is the necessary condition of equilibration of thin Neo-Hookean films floating on water. Equation (6.12) cannot be transformed to an explicit function of λ_1 , therefore the equilibrium stretch ratio for a given d and μ must be calculated by algorithms such as Newton's method or binary search. For convenience, a computer algorithm was written which uses Equation 6.12 to determine the equilibrium stretch ratio λ_{equi} will be noted as

$$f(d, \mu, \gamma_{\text{net}}) = \lambda_{\text{equi}}. \tag{6.13}$$

6.3 Equilibrium state of thin Neo-Hookean films on water

6.3.1 Theoretical calculation

Using Equation 6.10, we calculate the normalised free energies of floating thin Neo-Hookean films. In order to model a PDMS film, the shear modulus was set to 500 KPa and the net interfacial tension was arbitrarily set approximated to $\gamma_{\text{net}} = -7.8 \text{ mN/m}$. As shown in Figure 6.2(a), the normalised net free energy forms a concave curve for films with $d > 15.6 \text{ nm}$. The minima are located between $0 < \lambda_1 < 1$ which arises from the negative value of γ_{net} , reducing the surface energy with expanding film area. The position of the minimum is shifted towards zero with decreasing film thickness, because of an increasing significance of surface tension with decreasing film thickness. The minimum reaches $\lambda_1 = 0$ when $d = 15.6 \text{ nm}$, at which point the film has to occupy an infinite area. The theoretical thickness which causes infinite expansion is set by $d_{\text{inf}} = -\frac{\gamma_{\text{net}}}{\mu}$, which is easily obtained by considering the limit of Equation 6.12 as λ_1 approaches zero. This result is obviously non-physical, because elastomers can only stretch to a finite area. The equilibrium stretch ratio of the film λ_1 is calculated from Equation (6.13), obtaining $\lambda_1 = 0.99$ for a film thickness of $d_0 = 225 \text{ nm}$ and $\lambda_1 = 0.999$ $d_0 = 5.23 \text{ }\mu\text{m}$.

6.3.2 Experimental method

In order to compare the theoretical calculations with experimental results, thickness measurements of PDMS films floating on water were performed. PDMS (Sylgard 184 with 10:1 mixing ratio of polymer and cross linking agent) was spin-coated on silicon wafers with a PSS sacrificial layer. The thickness of the PDMS films was measured on the wafers and on water by reflection spectra measurements. Films with thicknesses of about 200 to 1400 nm were used.

6.3.3 Analysis of the experimental results

The differences in film thickness on the wafer and on the water surface are shown in Figure 6.3. As expected, there is a clear correlation between the film thickness and the change in thickness. We further analyse the results by using Equation 6.13. The following notations will be used in the discussion below.

- d : non-strained thickness
- d_0 : thickness on substrate
- d_1 : thickness on water
- λ_{sub} : d_0/d
- λ_{equi} : d_1/d

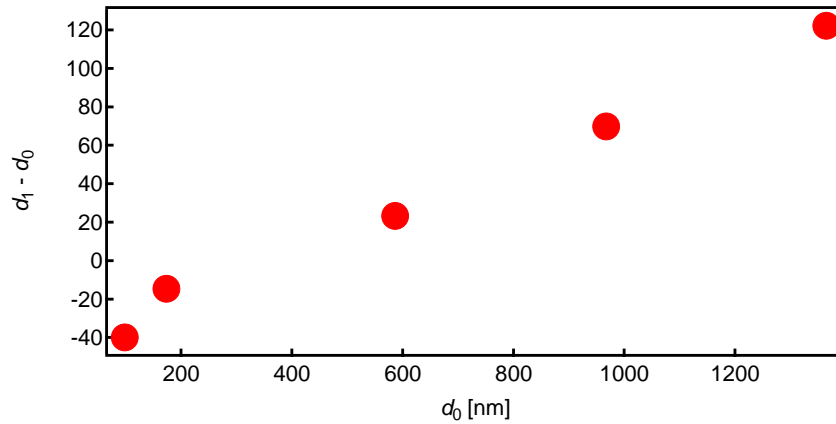


Figure 6.3: Film thickness difference before (d_0) and during d_1 the floating process.

d can be rewritten in terms of d_0 as

$$d = \frac{d_0}{\lambda_{\text{sub}}}. \quad (6.14)$$

Therefore equation 6.13 can be rewritten as

$$f(d_0, \lambda_{\text{sub}}, \mu, \gamma) = \lambda_{\text{equi}}. \quad (6.15)$$

Dividing by λ_{sub} will give

$$\frac{f(d_0, \lambda_{\text{sub}}, \mu, \gamma)}{\lambda_{\text{sub}}} = \frac{\lambda_{\text{equi}}}{\lambda_{\text{sub}}} = \frac{d_1}{d_0}. \quad (6.16)$$

We further simplify the notation as

$$\begin{aligned} \frac{f(d_0, \lambda_{\text{sub}}, \mu, \gamma_{\text{net}})}{\lambda_{\text{sub}}} &= \\ g(d_0, \lambda_{\text{sub}}, \mu, \gamma_{\text{net}}) &= \frac{d_1}{d_0} \end{aligned} \quad (6.17)$$

We have arrived at a function which quantifies $\frac{d_1}{d_0}$ in terms of four parameters, a value that can be directly calculated from the experimental data.

$\frac{d_1}{d_0}$ was plotted as a function of d_0 as shown in Figure 6.4. Equation 6.17 was fitted to the plot using d_0 as an independent variable, $\mu = 500$ KPa and λ_{sub} and γ_{net} are varied to provide the best fit, yielding $\lambda_{\text{sub}} = 0.9$ and $\gamma_{\text{net}} = -47$ mN/m.

Using $\gamma_{\text{aw}} = 72.8$ mN/m^[91] and $\gamma_{\text{af}} = 20$ mN/m^[92] for the surface tension of water and PDMS, the interfacial tension between water and PDMS, $\gamma_{\text{fw}} = 5.8$ mN/m, was obtained by Equation 6.6. We substitute γ_{aw} , γ_{af} and γ_{fw} in Young's equation

$$\gamma_{\text{af}} = \gamma_{\text{fw}} + \gamma_{\text{aw}} \cos \theta \quad (6.18)$$

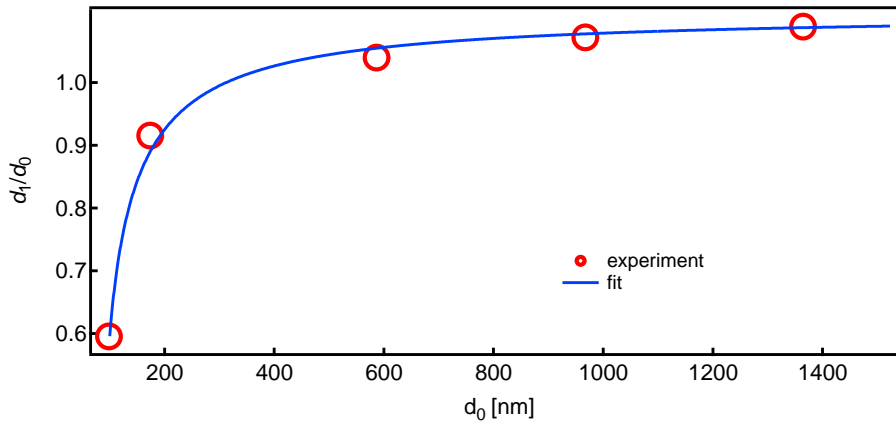


Figure 6.4: Ratio of film thickness on wafers, d_w , and on water, d_0 , plotted as a function of d_0 .

which gives $\theta \approx 78^\circ$. To verify the calculation, the contact angle of water on PDMS was measured by a goniometer and was found to be $\theta = 114^\circ$ (average of five measurements). A contact angle measurement of water on PDMS surface that has been in contact with the sacrificial layer yielded $\theta = 64^\circ$, close to the value found above. This indicates that the PDMS surface tension was altered by the contact with polyelectrolyte sacrificial layer.

Polyelectrolyte brushes attached to hydrophobic surfaces can reduce the contact angle of water.^[93] Since the PDMS film was floated off by a polyelectrolyte sacrificial layer, one possible explanation of the decrease in the contact angle is that the polyelectrolyte has formed a polymer brush on the PDMS surface facing the water. Another possibility is that the polyelectrolyte is acting as a surfactant. In both cases, we can assume that the polyelectrolyte attached to the PDMS surface has lowered the interfacial tension from $\gamma_{fw} = 45$ mN/m (calculated using $\theta = 114^\circ$) to $\gamma_{fw} = 5.8$ mN/m.

The modified surface tension of the PDMS can be calculated using $\gamma_{fw} = 5.8$ mN/m, $\theta = 64^\circ$ and $\gamma_{aw} = 72.8$ mN/m to arrive at $\gamma_{af} = 38$ mN/m. This result seems reasonable because the polyelectrolyte is charged and its surface tension should be greater than that of non-polar PDMS surface. The significance of the effect of the polyelectrolyte becomes clear when the experimental result is compared to the calculation assuming that no polyelectrolyte is attached to the PDMS surface. The calculation of Figure 6.2(c) is, in fact, based on this assumption and yields a compressive strain of only 5% for $d = 100$ nm, whereas the fit in Figure 6.4 yields a compression of about 30% for the same thickness.

The strain of the film before floating, $\lambda_{\text{sub}} = 0.9$, arises from an isotropic shrinkage of PDMS by 2% in length when cooling down after curing at 100°C , corresponding to a volume change of about

$$1 - 0.98^3 \approx 6\%.$$

Since the PDMS film is immobilised on a substrate, the thermal expansion and con-

traction should be only possible in the direction of the surface normal of the film. Therefore the volume change causes a vertical compression of $\lambda_1 = 0.94$. This value is in fair agreement with our observation, and we conclude that the compressive strain of the PDMS film before floating is mainly caused by thermal contraction.

6.4 Conclusion and future prospect

The experimental results demonstrated that the equilibrium state of thin PDMS films follow the prediction of Equation 6.13. Two origins in strain of thin PDMS films were identified, which are surface tension of a film on a water surface and thermal contraction after the curing of PDMS. Because of the surface tension, the film can either expand or shrink to minimise the net free energy on water surface depending on the sign of γ_{net} . It was shown in the experiment that γ_{net} of the PDMS film floated from a sacrificial polyelectrolyte layer is negative, and the interfacial energy is reduced when the water surface is covered by the film. Therefore the area of the films will expand with respect to its non-strained state, such that it can balance the elastic force of PDMS.

A PDMS film with a thickness of 100 nm which is suitable for making optical devices, is then compressed in the direction of its thickness as much as $\lambda_1 = 0.54$ for a rubber with a shear modulus is 500 KPa. The contact angle measurement suggests that the PDMS surface is modified by PSS, which enhances the effect of surface tension.

It was also found that the film is equibiaxially strained on the substrate before floating. This is most likely caused by the one-dimensional shrinkage during the cooling process after the thermal curing. Performing additional experiments with different curing temperatures should further confirm this finding.

As mentioned earlier, the goal of this chapter is not to merely study the equilibrium state of thin elastomer films, but to provide insight into wrinkling/creasing instabilities that occur during Elastomeric DBR manufacture. The strategy that should be taken becomes clear once the cause of the strain in the PDMS film is elucidated. The strain caused by surface tension can be eliminated by optimising the interfacial tensions. More specifically, the surface tension should have no effect on the equilibrium state of the film and will not induce any strain, when

$$\lambda_{aw} = \lambda_{af} + \lambda_{fw}$$

is satisfied. Such treatment is sufficient to eliminate the strain induced by the floating process. The most straightforward and effective idea for doing this is to use a neutral polymer as a sacrificial layer in the place of the polyelectrolyte. In addition, a liquid with a lower surface tension such as surfactant solutions or mixtures of water and organic solvents can be used.

For thermally cured elastomer films such as PDMS, the strain induced by thermal expansion might play a role in the wrinkle/crease formation, especially at the late stages of the assembly process. In order to double the number of layer stack, the folding

method requires the film to be partially attached to the substrate during the process. To avoid strain mismatch between the floated film and the film on the substrate, the strain of the floated film has to be matched to that of the film on the substrate. At the early stage of the folding steps, this can be achieved by controlling the strain by optimising the interfacial tensions, however this becomes difficult during the later stage when the film thickness becomes larger. At this point, the effect of surface tension is negligible and the strain of the floating film approaches to zero by increasing film thickness, due to the increasing effect of the Helmholtz free energy. If the film on the substrate has a finite amount of strain, the folding process will induce strain mismatch between the floated film and the film on the substrate, which cannot be controlled by optimising the interfacial tensions. As a new strategy, the strain of the film on the substrate can be controlled by keeping the curing temperature as low as possible. This will reduce the volume change by heating/cooling, hence result in a reduced strain of the film on the substrate. In addition, elevating the temperature of the water for floating to that of the curing temperature can be also useful. The film becomes heated up to the temperature to its non-strained shape, at which point the compressive strain will become zero.

This study has been limited to PDMS, but a second material is required for the manufacture of DBRs, and this second materials should be included in the discussion. If the second material is PSPI, and if there is any strain remaining in the film after spin-coating, it can be easily removed by thermal annealing because PSPI is a thermoplastic elastomer.^[44] Ultimately, making Elastomeric DBRs purely based on thermoplastic elastomers by extrusion may be the most realistic route for practical applications,^[62] as long as a sufficient refractive index contrast can be realised between the two materials.

6.5 Additional remarks

This chapter was written in order to elucidate the relevant parameters, to demonstrate how they can be measured and suggest how they can be controlled. In principle, all the parameters, which are the shear modulus and strain of the thin rubber film, interfacial tension and thermal expandability, can be calculated only from film thickness measurements and contact angle measurements, which are both very easy to perform.

As always, time is what limits us. Unfortunately, the fabrication of a high quality DBR described in the end of Chapter 6 could not be carried out in this work, therefore the capability of the new method is yet to be tested. However, this method might be the only possible route for the realisation of an all-rubber optical device that is something more than just a flat and small color changing mirror, created from thin rubber films by floating on a water surface.

In book 13 of the Analects of Confucius, a conversation between Confucius and his student Zi Xia is recorded:

子夏爲魯筭父宰,問政,子曰:“毋欲速,毋見小利。欲速則不達,見小利則大事不成。”

The English translation of this passage is the following:

Zi Xia became the head governor of Ju Fu and consulted Confucius on politics. Confucius replied, “Never hurry. Do not pursue a small profit. If you hurry, you will fail. If you pursue a small profit, you can not achieve a great accomplishment.”

We should understand from his saying that rushing towards a high impact research, such as stretchable lasing, without having a good foundation established, leads to nowhere. Instead, studies that seems to have limited impact at the first sight can actually be the shortest route to the ultimate goal. Sophisticated work are only possible with a firm basis. This is a fact that should go without saying.

Conclusion and future work

In this thesis, the optics and mechanics of DBRs consisting purely of rubbers were studied. The optical property of the axisymmetrically inflated DBRs were studied in relation to their structures and mechanical properties.

In Chapter 2, theories of optical properties of thin films and multilayer films, mechanical properties of rubbers, mechanics of curved structures and surface surface chemistry of films were presented in the context of this thesis. The emphasis was on the mechanics rather than on optics. This was because the theory of rubber elasticity was necessary for Chapter 5 and 6 and also because the detailed understanding of the mechanics of rubber seem to be lacking in the optics community.

In the recent years, thin rubber films have been one of the main classes of materials which have been used for creating DBRs and metamaterials by various assembly methods.^[15–18] As discussed, one of the concepts behind the idea of using rubbers as constituent materials in DBRs is to enable the tuning of the optical response by mechanical stimuli. Rubbers are capable of undergoing large reversible deformations, making it a material suitable for building optical devices that can be tuned in a wide-spanning range of optical wavelength by stretching. Such a concept provides an attractive outline for high-impact research; however since its focus is on optics, a thorough understanding of their mechanics has been lacking and was preventing a detailed description of the behaviour of soft, thin and layered structures under large deformation. Without the right understanding, one may naively make the following assumptions:

1. Thin rubber films can be assembled on water surface without causing any stress or change in their shape.
2. Deformation of rubbery optical devices will always occur homogeneously across the entire device in a reversible fashion.

These assumptions are by no means correct. Firstly, thin rubber films that are floating on water can be highly strained due to surface tension. Secondly, non-linear processes such as buckling and related instabilities can occur during large deformation. This effect has a possibility of critically spoil the quality of DBRs.

To those who are aware of these facts, the creation of optical devices that are free from creases using thin rubber films, may seem an extremely difficult task, which may undermine the motivation of pursuing this challenge. In that sense, it may be said that the initial successes in the Elastomeric DBRs were possible because of a bold challenging spirit, excellent manual skills and a lack of preconception. However, it is important to establish a deeper understanding of the fabrication process in order to further extend the studies on elastomeric DBRs. Since Chapter 6 has provided the foundation of the mechanics of thin elastomer films on water, improvement of the fabrication process should be relatively straightforward.

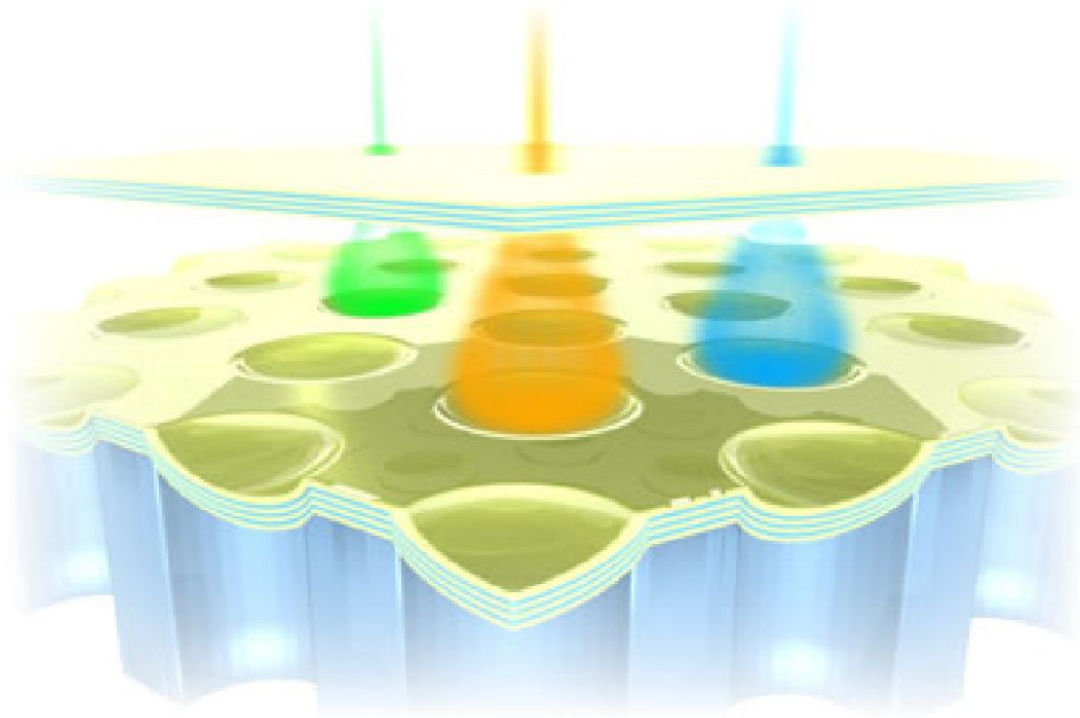


Figure 6.5: An example of a possible application suggested by Kolle. Reprinted from Kolle.^[12]

The following briefly summarises Chapters 3 to 5. Chapter 3 introduced the materials and methods that were used in this study. In particular, a method developed by Anglin *et al.*^[50] for calculating the approximate thickness of films from spectral measurements, was studied in great detail. To our knowledge, there is no documentation that is accessible for the public which describes the properties of the method in the detail of Chapter 3.

Chapter 4 describes the fabrication, repeatable full-colour tuning and radially inhomogeneous distribution of strain in Elastomeric DBRs, tuned by a pressure difference. The stop-band of the DBR can be tuned from 830 nm in the near-IR down to 400 nm in the blue without compromising the peak intensity. To our knowledge, this is the current world record of stop-band wavelength tuning in the visible spectrum of photonic crystals by mechanical stimuli.

Chapter 5 studied the radially heterogeneous distribution of the strain of the deformed DBR by numerical analysis. The DBR was modelled by the Mooney-Rivlin equation and the effect of creep was examined by evaluating the distribution of the effective stiffness. It was concluded that the inverted hue sequence of the deformed DBR which resembles *Chlorophila obscuripennis*, was created due to the geometry of the inflation process and the viscoelasticity of the DBR.

Taking all these results into account, the following suggestion is given as an outlook for further research on Elastomeric DBRs. As a possible application of Elastomeric

DBRs, Kolle suggested an optical device consisting of an array of individually addressed pressure-tuneable optical micro-cavities^[12] as shown in Figure 6.5. After having a detailed understanding of the optics and mechanics of axisymmetrically inflated DBRs established, Kolle's blueprint can be redesigned with more specific details.

First, a fabrication method for high quality Elastomeric DBRs can be developed based on the discussion in Chapter 6. Once this is established, an array of pressure tuneable concavities can be created with a supporting sheet with many holes. It is assumed from the results of Chapter 5 that the concave form of the deformed DBR can become permanent. There are two stable forms of the permanently deformed DBR films; the concavity bulged up and bulged down. All the concavities in the array can be rapidly switched between these two states by popping the concavity upwards and downwards by applying positive and negative pressure differences. By doing so, the double-reflection occurring within the individual concavities can be switched on and off, which will enable and disable the colour-mixing effect. This effect can create a clear contrast in the displayed colour between the two states, however a clever method that eliminates the intra-cavity double-reflection will make effect even more vivid.

This can be done by introducing some randomness in the structure, for example by varying the size of the holes or film thickness, either of which will lead to a change in the degree of inflation, resulting in different degree of stop-band tuning at the edge of the concavity. When the stop-band of the edge of neighbouring concavities are sufficiently off-tuned, the intra-cavity double reflection is suppressed. Potential applications that may utilise this concept include bistable optical device security printing or a colour display that can switch its colour by pressure difference.

Related Publications

Multilayer mirrored bubbles with spatially-chirped and elastically-tuneable optical bandgaps – Gen Kamita, Mathias Kolle, Fumin Huang, J.J. Baumberg, and Ullrich Steiner, **Optics Express** 20, 6421-6428 (2012)

Layer-by-Layer Formation of Block-Copolymer-Derived TiO₂ for Solid-State Dye-Sensitized Solar Cells – Stefan Guldin, Pablo Docampo, Morgan Stefik, Gen Kamita, Ulrich Wiesner, Henry J. Snaith, and Ullrich Steiner, **Small** 8, 432-440 (2011)

Internal electrical field of ZnO nanoparticle based memristors – Cheng Li, Gareth Beirne, Gen Kamita, Jianpu Wang and Neil C. Greenham **In preparation**

Effect of geometry and mechanical property on the optical effects of axisymmetrically inflated elastic DBR Gen Kamita, J.J. Baumberg, and Ullrich Steiner **In preparation**

Highly reflective stretchable DBR from liquid crystalline elastomer Gen Kamita, J.J. Baumberg, and Ullrich Steiner **In preparation**

Acknowledgement

I address my special thanks^[0] to Prof. Ulrich Steiner, Prof. Jeremy Baumberg, Prof. Eugene Terentjev, Dr. Mathias Kolle, Dr. Jean Marshall, Dr. Kei Yamamoto, Dr. Ingrid Graz, Hong'En Tan, Robyn Pritchard, Christina and Erica for their help, advice and support during my PhD.

DUBBLE BM26, ESRF, Grenoble, France
2:00 AM, 30th September 2013

[0] Igor P. Dolbnya, “*A Synchrotron Small-Angle X-ray Scattering Study of Order/Disorder in Colloidal Crystals*”(2004)

Bibliography

- [1] T. Gray, “Silver mirror,” <http://www.theodoregray.com> .
- [2] T. Gray, “Gold mirror,” <http://www.theodoregray.com> .
- [3] J. Liebig, “Ueber Versilberung und Vergoldung von Glas,” *Justus Liebigs Annalen der Chemie* **98**, 132–139 (1856).
- [4] B. E. Wood, J. G. Pipes, a. M. Smith, and J. a. Roux, “Hemi-ellipsoidal mirror infrared reflectometer: development and operation.” *Applied Optics* **15**, 940–50 (1976).
- [5] J. M. Hoffman, a. K. Hays, and G. C. Tisone, “High-power UV noble-gas-halide lasers,” *Applied Physics Letters* **28**, 538 (1976).
- [6] J. P. Gardner, J. C. Mather, M. Clampin, R. Doyon, M. a. Greenhouse, H. B. Hammel, J. B. Hutchings, P. Jakobsen, S. J. Lilly, K. S. Long, J. I. Lunine, M. J. Mccaughrean, M. Mountain, J. Nella, G. H. Rieke, M. J. Rieke, H.-W. Rix, E. P. Smith, G. Sonneborn, M. Stiavelli, H. S. Stockman, R. a. Windhorst, and G. S. Wright, “The James Webb Space Telescope,” *Space Science Reviews* **123**, 485–606 (2006).
- [7] H. P. Stahl, L. D. Feinberg, and S. C. Texter, “JWST primary mirror material selection,” *Proceedings of SPIE* **5487**, 818–824 (2004).
- [8] J. M. Enoch, “History of Mirrors Dating Back 8000 Years,” *Optometry and Vision Science* **83**, 775–781 (2006).
- [9] W. A. Haviland, H. E. L. Prins, B. McBride, and D. Walrath, *Anthropology: The Human Challenge* (Wadsworth Publishing, 2010).
- [10] A. S. Grabtchikov, A. N. Kuzmin, V. A. Lisinetskii, and V. A. Orlovich, “Passively Q-switched 1 : 35 lm diode pumped Nd : KGW laser with V : YAG saturable absorber,” *Optical Materials* **16**, 349–352 (2001).
- [11] J. D. Joannopoulos, S. G. Johnson, J. N. Winn, and R. D. Meade, *Photonic Crystals: Molding the Flow of Light* (Princeton University Press, 2011), second edi ed.
- [12] M. Kolle, “Photonic Structures Inspired by Nature,” Ph.D. thesis, University of Cambridge (2011).
- [13] P. J. Flory and J. Rehner, “Statistical Mechanics of Cross-Linked Polymer Networks II. Swelling,” *The Journal of Chemical Physics* **11**, 521 (1943).
- [14] Y. Kang, J. J. J. Walish, T. Gorishnyy, and E. L. E. Thomas, “Broad-wavelength-range chemically tunable block-copolymer photonic gels.” *Nature Materials* **6**, 957–960 (2007).

- [15] M. Kolle, B. Zheng, N. Gibbons, J. J. Baumberg, and U. Steiner, “Stretch-tuneable dielectric mirrors and optical microcavities,” *Optics Express* **18**, 575–581 (2010).
- [16] N. Gibbons and J. J. Baumberg, “Corrugated metallodielectric superlattices via release-rollup assembly.” *Optics Express* **19**, 15596–602 (2011).
- [17] N. Gibbons, J. J. Baumberg, C. L. Bower, M. Kolle, and U. Steiner, “Scalable Cylindrical Metallodielectric Metamaterials,” *Advanced Materials* **21**, 3933–3936 (2009).
- [18] N. Gibbons and J. J. Baumberg, “Optical minibands in metallodielectric superlattices,” *Physical Review B* **85**, 165422 (2012).
- [19] M. Kolle, A. Lethbridge, M. Kreysing, J. J. Baumberg, J. Aizenberg, and P. Vukusic, “Bio-Inspired Band-Gap Tunable Elastic Optical Multilayer Fibers.” *Advanced Materials* pp. 1–7 (2013).
- [20] M. Kolle, P. M. Cunha, M. R. J. Scherer, H. Fumin, P. Vukusic, S. Mahajan, J. Baumberg, and U. Steiner, “Mimicking the colourful wing scale structure of the *Papilio blumei* butterfly,” *Nature Nanotechnology* **5**, 511–515 (2010).
- [21] P. Vukusic, J. R. Sambles, and C. R. Lawrence, “Colour mixing in wing scales of a butterfly.” *Nature* **404**, 457 (2000).
- [22] F. Liu, B. Dong, and X. Liu, *Optical Devices in Communication and Computation* (InTech, 2012).
- [23] M. Crne, V. Sharma, J. Blair, J. O. Park, C. J. Summers, and M. Srinivasarao, “Biomimicry of optical microstructures of *Papilio palinurus*,” *Europhysics Letters* **93**, 14001 (2011).
- [24] J. Walish, Y. Kang, R. Mickiewicz, and E. Thomas, “Bioinspired electrochemically tunable block copolymer full color pixels,” *Advanced Materials* **21**, 3078–3081 (2009).
- [25] F. Liu, H. Yin, B. Dong, Y. Qing, L. Zhao, S. Meyer, X. Liu, and B. Chen, “Inconspicuous structural coloration in the elytra of beetles *Chlorophila obscuripennis* (Coleoptera),” *Physical Review E* **77**, 012901 (2008).
- [26] Y.-Y. Diao and X.-Y. Liu, “Mysterious coloring: structural origin of color mixing for two breeds of *Papilio* butterflies.” *Optics express* **19**, 9232–41 (2011).
- [27] O. Heavens, *Optical properties of thin solid films* (Dover Publications, 1965).
- [28] L. R. F. Treloar, *The Physics of Rubber Elasticity* (Oxford University press, 1975), third edit ed.
- [29] I. Müller and P. Strehlow, *Rubber and Rubber Balloons: Paradigms of Thermodynamics* (Springer, 2004).

- [30] K. H. Meyer and C. Ferri, “Sur l’élasticité du caoutchouc,” *Helvetica Chimica Acta* **18**, 570–589 (1935).
- [31] H. Erbil, *Surface chemistry of solid and liquid interfaces* (Wiley, 2006).
- [32] H. J. Butt, K. Graf, and M. Kappl, *Physics and Chemistry of Interfaces* (Wiley, 2006).
- [33] W. Dreyer, I. Müller, and P. Strehlow, “A study of equilibria of interconnected balloons,” *The Quarterly Journal of Mechanics & Applied Mathematics* **35**, 419–440 (1982).
- [34] F. Weinhaus and W. Barker, “On the equilibrium states of interconnected bubbles or balloons,” *American Journal of Physics* **46**, 978–982 (1978).
- [35] L. Treloar, “Stress-strain data for vulcanised rubber under various types of deformation,” *Transactions of the Faraday Society* (1944).
- [36] T. K. Kim, J. K. Kim, and O. C. Jeong, “Measurement of nonlinear mechanical properties of PDMS elastomer,” *Microelectronic Engineering* **88**, 1982–1985 (2011).
- [37] Smokefoot, “Wikimedia,” <http://commons.wikimedia.org/> .
- [38] R. Azzam and N. Bashara, *Ellipsometry and polarized light* (Elsevier, 1987).
- [39] H. Tompkins, *Handbook of Ellipsometry* (William Andrew Inc., 2005).
- [40] R. M. H. Poetes, “Dynamic and static conformations at the water-solid interface,” Ph.D. thesis, University of Cambridge (2009).
- [41] F. Schneider, J. Draheim, R. Kamberger, and U. Wallrabe, “Process and material properties of polydimethylsiloxane (PDMS) for Optical MEMS,” *Sensors and Actuators A: Physical* **151**, 95–99 (2009).
- [42] M. Liu, J. Sun, and Q. Chen, “Influences of heating temperature on mechanical properties of polydimethylsiloxane,” *Sensors and Actuators A: Physical* **151**, 42–45 (2009).
- [43] Sigma-Aldrich, “Polystyrene-block-polyisoprene-block-polystyrene,” <http://www.sigmaaldrich.com/catalog/product/aldrich/432415> .
- [44] A. Hotta, S. M. Clarke, and E. M. Terentjev, “Stress Relaxation in Transient Networks of Symmetric Triblock Styrene-Isoprene-Styrene Copolymer,” *Macromolecules* **35**, 271–277 (2002).
- [45] A. Sánchez-Ferrer, T. Fischl, M. Stubenrauch, H. Wurmus, M. Hoffmann, and H. Finkelmann, “Photo-Crosslinked Side-Chain Liquid-Crystalline Elastomers for Microsystems,” *Macromolecular Chemistry and Physics* **210**, 1671–1677 (2009).

- [46] J. Küpfer and H. Finkelmann, “Nematic liquid single crystal elastomers,” *Die Makromolekulare Chemie, Rapid Communications* **12**, 717–726 (1991).
- [47] M. Warner and E. Terentjev, “Nematic elastomers—a new state of matter?” *Progress in Polymer Science* **21**, 853–891 (1996).
- [48] S. V. Ahir, A. R. Tajbakhsh, and E. M. Terentjev, “Self-Assembled Shape-Memory Fibers of Triblock Liquid-Crystal Polymers,” *Advanced Functional Materials* **16**, 556–560 (2006).
- [49] J. E. Marshall, Y. Ji, N. Torras, K. Zinoviev, and E. M. Terentjev, “Carbon-nanotube sensitized nematic elastomer composites for IR-visible photo-actuation,” *Soft Matter* **8**, 1570 (2012).
- [50] E. J. Anglin, M. P. Schwartz, V. P. Ng, L. a. Perelman, and M. J. Sailor, “Engineering the chemistry and nanostructure of porous silicon Fabry-Pérot films for loading and release of a steroid.” *Langmuir* **20**, 11264–9 (2004).
- [51] J. Wu and M. J. Sailor, “Chitosan Hydrogel-Capped Porous SiO₂ as a pH Responsive Nano-Valve for Triggered Release of Insulin,” *Advanced Functional Materials* **19**, 733–741 (2009).
- [52] S. Pace, R. B. Vasani, F. Cunin, and N. H. Voelcker, “Study of the optical properties of a thermoresponsive polymer grafted onto porous silicon scaffolds,” *New Journal of Chemistry* **37**, 228 (2013).
- [53] E. J. Anglin, L. Cheng, W. R. Freeman, and M. J. Sailor, “Porous silicon in drug delivery devices and materials.” *Advanced Drug Delivery Reviews* **60**, 1266–77 (2008).
- [54] T. Kumeria and D. Losic, “Controlling interferometric properties of nanoporous anodic aluminium oxide.” *Nanoscale Research Letters* **7**, 88 (2012).
- [55] L. a. Perelman, T. Moore, J. Singelyn, M. J. Sailor, and E. Segal, “Preparation and characterization of a pH- and thermally responsive poly(N-isopropylacrylamide-co-acrylic acid)/porous SiO(2) hybrid.” *Advanced Functional Materials* **20**, 826–833 (2010).
- [56] Y. Shang, W. Zhao, E. Xu, C. Tong, and J. Wu, “FTRIFS biosensor based on double layer porous silicon as a LC detector for target molecule screening from complex samples.” *Biosensors & Bioelectronics* **25**, 1056–63 (2010).
- [57] M. Sasso, G. Palmieri, G. Chiappini, and D. Amodio, “Characterization of hyperelastic rubber-like materials by biaxial and uniaxial stretching tests based on optical methods,” *Polymer Testing* **27**, 995–1004 (2008).
- [58] U. Scherf, S. Riechel, U. Lemmer, and R. Mahrt, “Conjugated polymers: lasing and stimulated emission,” *Current Opinion in Solid State and Materials Science* **5**, 143–154 (2001).

- [59] X. Xu, Y. Dai, X. Chen, D. Jiang, and S. Xie, “Chirped and phase-sampled fiber Bragg grating for tunable DBR fiber laser.” *Optics Express* **13**, 3877–82 (2005).
- [60] T. Komikado, a. Inoue, K. Masuda, T. Ando, and S. Umegaki, “Multi-layered mirrors fabricated by spin-coating organic polymers,” *Thin Solid Films* **515**, 3887–3892 (2007).
- [61] Y. Yang, G. a. Turnbull, and I. D. W. Samuel, “Hybrid optoelectronics: A polymer laser pumped by a nitride light-emitting diode,” *Applied Physics Letters* **92**, 163306 (2008).
- [62] K. D. Singer, T. Kazmierczak, J. Lott, H. Song, Y. Wu, J. Andrews, E. Baer, A. Hiltner, and C. Weder, “Melt-processed all-polymer distributed Bragg reflector laser.” *Optics Express* **16**, 10358–63 (2008).
- [63] E. Schubert, Y. Wang, and A. Cho, “Resonant cavity light-emitting diode,” *Applied Physics Letters* **60**, 921–923 (1992).
- [64] S. Chang, C. Chang, Y. Su, P. Chang, Y. Wu, K. Huang, and T. Chen, “Chirped GaAs-AlAs distributed Bragg reflectors for high brightness yellow-green light-emitting diodes,” *Photonics Technology Letters, IEEE* **9**, 182–184 (1997).
- [65] S. W. Chiou, C. P. Lee, C. K. Huang, and C. W. Chen, “Wide angle distributed Bragg reflectors for 590 nm amber AlGaInP light-emitting diodes,” *Journal of Applied Physics* **87**, 2052 (2000).
- [66] S. Colodrero, M. Ocaña, and H. Míguez, “Nanoparticle-based one-dimensional photonic crystals.” *Langmuir* **24**, 4430–4434 (2008).
- [67] O. Sánchez-Sobrado, M. Calvo, N. Núñez, M. Ocaña, G. Lozano, and H. Míguez, “Environmentally responsive nanoparticle-based luminescent optical resonators,” *Nanoscale* **2**, 936–941 (2010).
- [68] S. Guldin, M. Kolle, M. Stefik, R. Langford, D. Eder, U. Wiesner, and U. Steiner, “Tunable Mesoporous Bragg Reflectors Based on Block-Copolymer Self-Assembly.” *Advanced Materials* **23**, 3664–3668 (2011).
- [69] S. Colodrero, A. Mihi, L. Häggman, M. Ocaña, G. Boschloo, A. Hagfeldt, and H. Míguez, “Porous One-Dimensional Photonic Crystals Improve the Power-Conversion Efficiency of Dye-Sensitized Solar Cells,” *Advanced Materials* **21**, 764–770 (2009).
- [70] S. Colodrero, A. Mihi, J. A. Anta, M. Ocaña, and H. Míguez, “Experimental Demonstration of the Mechanism of Light Harvesting Enhancement in Photonic-Crystal-Based Dye-Sensitized Solar Cells,” *The Journal of Physical Chemistry C* **113**, 1150–1154 (2009).
- [71] M. E. Calvo and H. Míguez, “Flexible, Adhesive, and Biocompatible Bragg Mirrors Based on Polydimethylsiloxane Infiltrated Nanoparticle Multilayers,” *Chemistry of Materials* **22**, 3909–3915 (2010).

- [72] M. H. Song, B. Wenger, and R. H. Friend, “Tuning the wavelength of lasing emission in organic semiconducting laser by the orientation of liquid crystalline conjugated polymer,” *Journal of Applied Physics* **104**, 033107 (2008).
- [73] S. Coyle, G. V. Prakash, J. J. Baumberg, M. Abdelsalem, and P. N. Bartlett, “Spherical micromirrors from templated self-assembly: Polarization rotation on the micron scale,” *Applied Physics Letters* **83**, 767 (2003).
- [74] P. Vukusic, R. Sambles, C. Lawrence, and G. Wakely, “Sculpted-multilayer optical effects in two species of Papilio butterfly,” *Applied Optics* **40**, 1116–1125 (2001).
- [75] S. Yoshioka and S. Kinoshita, “Polarization-sensitive color mixing in the wing of the Madagascan sunset moth.” *Optics Express* **15**, 2691–701 (2007).
- [76] J. Zhu, S. Cai, and Z. Suo, “Resonant behavior of a membrane of a dielectric elastomer,” *International Journal of Solids and Structures* **47**, 3254–3262 (2010).
- [77] S.-H. Yoon, V. Reyes-Ortiz, K.-H. Kim, Y. H. Seo, and M. R. K. Mofrad, “Analysis of Circular PDMS Microballoons With Ultralarge Deflection for MEMS Design,” *Journal of Microelectromechanical Systems* **19**, 854–864 (2010).
- [78] J. Vigneron, M. Ouedraogo, J.-F. Colomer, and M. Rassart, “Spectral sideband produced by a hemispherical concave multilayer on the African shield-bug *Calidea panaethiopica* (Scutelleridae),” *Physical Review E* **79**, 1–8 (2009).
- [79] S. Yoshioka and S. Kinoshita, “Effect of macroscopic structure in iridescent color of the peacock feathers,” *FORMA* **17**, 169–181 (2002).
- [80] D. G. Stavenga, H. L. Leertouwer, N. J. Marshall, and D. Osorio, “Dramatic colour changes in a bird of paradise caused by uniquely structured breast feather barbules.” *Proceedings. Biological sciences / The Royal Society* **278**, 2098–104 (2011).
- [81] G. Kamita, M. Kolle, F. Huang, J. Baumberg, and U. Steiner, “Multilayer mirrored bubbles with spatially-chirped and elastically-tuneable optical bandgaps,” *Optics Express* **20**, 6421–6428 (2012).
- [82] L. Treloar, “Stresses and birefringence in rubber subjected to general homogeneous strain,” *Proceedings of the Physical Society* **135** (1948).
- [83] K. Urayama, T. Kawamura, and S. Kohjiya, “Multiaxial deformations of end-linked poly(dimethylsiloxane) networks. 4. Further assessment of the slip-link model for chain-entanglement effect on rubber elasticity,” *The Journal of Chemical Physics* **118**, 5658 (2003).
- [84] H. Wang, S. Cai, F. Carpi, and Z. Suo, “Computational Model of Hydrostatically Coupled Dielectric Elastomer Actuators,” *Journal of Applied Mechanics* **79**, 031008 (2012).

- [85] Y. Fukahori and W. Seki, “Molecular behaviour of elastomeric materials under large deformation: 1. Re-evaluation of the Mooney-Rivlin plot,” *Polymer* **33**, 502–508 (1992).
- [86] B. Hancock and G. Zografi, “The relationship between the glass transition temperature and the water content of amorphous pharmaceutical solids,” *Pharmaceutical Research* **11**, 471 (1994).
- [87] B. F. V. Duzee, “The influence of water content, chemical treatment and temperature on the rheological properties of tratum corneum,” *The Journal of Investigative Dermatology* **71**, 140 (1978).
- [88] B. Li, Y.-P. Cao, X.-Q. Feng, and H. Gao, “Mechanics of morphological instabilities and surface wrinkling in soft materials: a review,” *Soft Matter* **8**, 5728 (2012).
- [89] E. Cerda and L. Mahadevan, “Geometry and Physics of Wrinkling,” *Physical Review Letters* **90**, 1–5 (2003).
- [90] J. Genzer and J. Groenewold, “Soft matter with hard skin: From skin wrinkles to templating and material characterization,” *Soft Matter* **2**, 310 (2006).
- [91] G. Vhquez, E. Alvarez, and J. M. Navaza, “Surface Tension of Alcohol + Water from 20 to 50 °C,” *Journal of Chemical and Engineering Data* **40**, 611–614 (1995).
- [92] I. B. Burgess, “Wetting in Color,” Phd thesis, Harvard University (2012).
- [93] N. Kampf, J.-F. Gohy, R. Jerome, and J. Klein, “Normal and shear forces between a polyelectrolyte brush and a solid surface,” *Journal of Polymer Science Part B: Polymer Physics* **43**, 193–204 (2005).